Dissertation Submitted to
the Ruperto-Carola University of Heidelberg, Germany
for the Degree of Doctor of Natural Sciences

Non-Destructive Detection and Resistive Cooling of Highly-Charged-Ion Ensembles for Precision Spectroscopy in the ARTEMIS Penning Trap

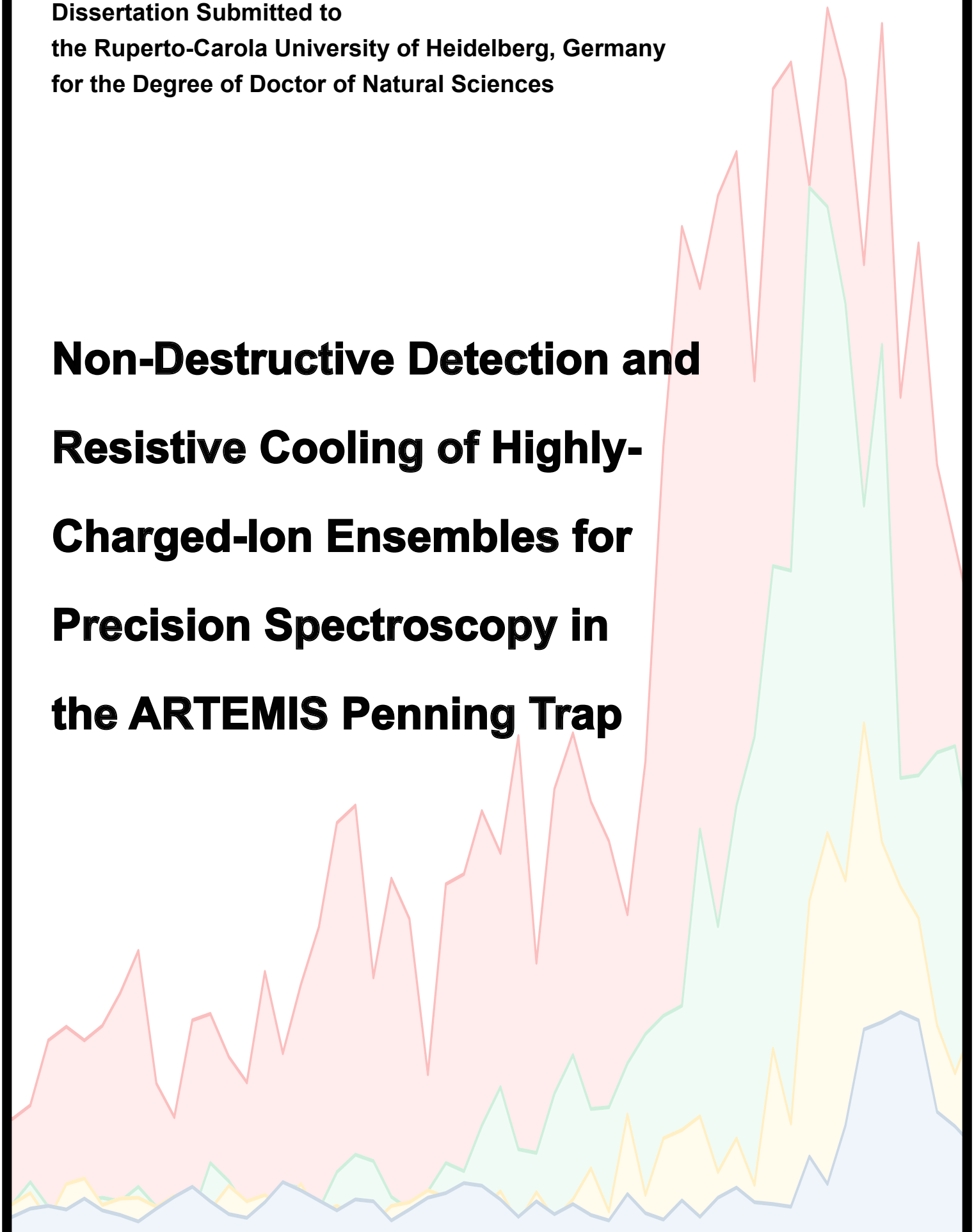

MOHAMMAD SADEGH EBRAHIMI

Dissertation
submitted to the
Combined Faculties for the Natural Sciences and for Mathematics
of the Ruperto-Carola University of Heidelberg, Germany
for the degree of
Doctor of Natural Sciences

Put forward by

Mohammad Sadegh Ebrahimi

Born in TEHRAN, IRAN

Oral examination: 02.05.2018

Non-Destructive Detection and Resistive Cooling

of Highly-Charged-Ion Ensembles

for Precision Spectroscopy in the ARTEMIS Penning Trap

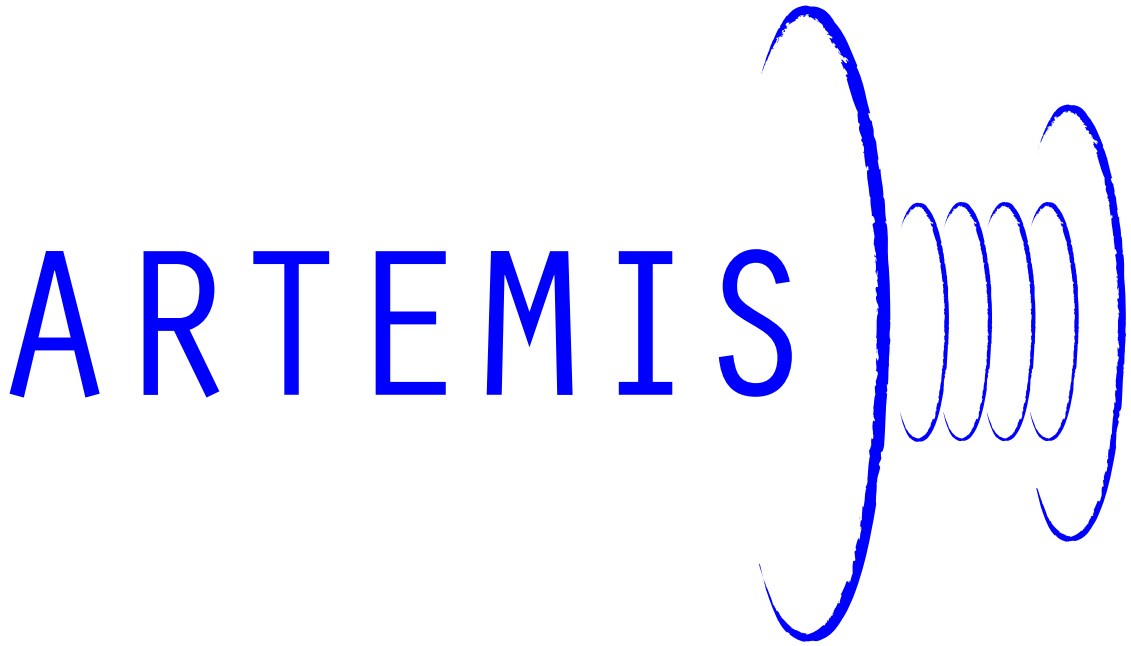

Referees: **Priv.-Doz. Dr.** **Wolfgang Quint**

Prof. Dr. **Markus Oberthaler**

Zerstörungsfreier Nachweis und Widerstandskühlung von Ensembles hochgeladener Ionen für präzisionsspektroskopische Messungen in der ARTEMIS-Penningfalle

Zusammenfassung: Ein wichtiger Aspekt bei Präzisionsmessungen in einer Penningfalle ist die Fähigkeit, die eingeschlossenen Partikel auf kryogene Temperaturen abkühlen zu können, um Messunsicherheiten zu reduzieren. Die ARTEMIS-Penningfalle, die sich in der HITRAP-Einrichtung an der GSI befindet, wurde entwickelt, um den $g-$Faktor von hochgeladenen Ionen wie etwa $^{40}Ar^{13+}$ und $^{209}Bi^{82+}$ zu messen. Das vorgesehene Messschema beinhaltet die Spektroskopie einer großen Anzahl von gespeicherten Teilchen in Form eines Ensembles, typischerweise in der Größenordnung von 10^5 Ionen. Diese Arbeit stellt die Entwicklung und das Upgrade des zerstörungsfreien RLC-Detektionssystems von ARTEMIS vor, das auch für die resistive Ionenkühlung verwendet wird. Die Funktionsweise beruht auf einer dissipativen Wechselwirkung der gespeicherten Ionen mit dem effektiven Widerstand des Detektionssystems. Eine theoretische Behandlung der resistiven Kühlung von einem in der Erzeugungsfalle produzierten Ion-Ensemble wurde durchgeführt und mit verschiedenen Ionen-Ensembles getestet.

Non-Destructive Detection and Resistive Cooling of Highly-Charged-Ion Ensembles for Precision Spectroscopy in the ARTEMIS Penning Trap

Abstract: An important aspect of precision measurements in a Penning trap is the ability to cool the confined particles to cryogenic temperatures, which reduces the measurement uncertainty. The ARTEMIS Penning trap, located at the HITRAP facility at GSI, is designed to measure the $g-$factor of heavy to medium highly charged ions, such as $^{40}Ar^{13+}$ and $^{209}Bi^{82+}$, using microwave-laser double resonance spectroscopy on a ppb level of accuracy. The foreseen measurement scheme involves spectroscopy of a large number of confined particles in the form of an ensemble, typically of the order of 10^5 ions. This thesis presents the development and upgrades of the non-destructive detection system of ARTEMIS, which is also used for resistive ion cooling through dissipative interaction with the effective resistance of the detection system. A theoretical treatment of resistive cooling of an ion ensemble created in the creation trap of ARTEMIS was performed and test with different ion ensembles.

CONTENTS

CHAPTER

ONE

INTRODUCTION

Highly charged ions offer one of the most versatile frameworks for a test of quantum electrodynamics (QED). A prime example is the measurement of magnetic moment ($g-$factor) of a bound electron. The extreme electromagnetic field in the close vicinity of the nucleus —of the order of $10^{16}\,\mathrm{V\,cm^{-1}}$ at the position of the electron in a heavy hydrogen-like ion—leads to two effects making the bound electron of a highly charged ion an interesting case for such a study. Firstly, the $g-$factors of the free electron [1] and bound electron [2, 3] are significantly different, which is the result of different categories of phenomena, among them the QED effects that roughly scale with the square of the nuclear charge number Z. Secondly, in heavy few-electron systems, such as $^{207}\mathrm{Pb}^{81+}$ and $^{209}\mathrm{Bi}^{82+}$, the energy of the ground-state hyperfine structure transitions are optically accessible via laser spectroscopy [4, 5]. The same is true for the fine structure transitions in medium to heavy highly charged ions such as $^{40}\mathrm{Ar}^{13+}$ or $^{84}\mathrm{Kr}^{17+}$ [6]. The present experiment aims at precision measurements of the bound electrons' magnetic moments via a technique which exploits the optical transitions available in such highly charged ions by use of optical and microwave spectroscopy of ions confined in a Penning trap.

A superposition of a harmonic electrostatic and a homogeneous magnetic potential for stable charged-particle confinement—later known as a Penning trap—was first proposed by J.R. Pierce in 1949 [7]. Shortly after, H.G. Dehmelt (1959) utilized this configuration for electron confinement and precision spectroscopy measurements [8, 9]. Later in 1986, using a Penning trap, Dehmelt's group succeeded in measuring the g-factor of the unbound electron with a relative precision of 4×10^{-12} [10]. This experimental confinement technique rapidly became adapted to a broad range of high-precision measurements making use of confinement and cooling of particles in Penning traps. A typical g-factor measurement of this kind is commonly performed using the so-called continuous Stern-Gerlach scheme, which involves probing the spin orientation of the confined particle with microwave signal and continuous

measurements of the relevant radio-frequency of ion oscillations[11]. As the particles in a Penning trap can be prepared in well-defined states for extended periods, and all observables are frequencies, potentially high precisions are to be expected. The measurement of the bound-electron $g-$factor of hydrogen-like carbon $^{12}C^{5+}$ [2] and oxygen $^{16}O^{7+}$ [3] with an uncertainty of 10^{-9}, lithium-like calcium Ca^{17+} isotopes with an uncertainty of 10^{-11} [12], and lithium-like calcium $^{28}Si^{11+}$ with a relative uncertainty of 10^{-9} [13] are outstanding examples of applying such an approach to highly charged ions.

The Stern-Gerlach scheme is the method of choice when measuring ions with zero-spin nuclei, while the microwave-laser double resonance spectroscopy can serve as a complementary $g-$factor measurement method in the case of non-zero spin nuclei [14]. In addition, the double-resonance method is capable of measuring the bound-electron g-factor and the nuclear $g-$factor simultaneously. The ARTEMIS setup is optimized for the measurement of the $g-$factor utilizing the double resonance spectroscopy for highly charged ions. In the double-resonance spectroscopy technique, the microwave probing of the Larmor frequency is measured through the laser-spectroscopy of the fine or hyperfine structure of the ion [15]. To be able to perform this scheme of measurement, a modification in the conventional open-end Penning trap design is required, in order to maximize the optical access to the ion ensemble. As a result, the concept of the half-open trap has been developed and utilized [16]. Currently, for commissioning reasons, ARTEMIS at HITRAP is set to measure the $g-$factor of an electron bound to $^{40}Ar^{13+}$ with parts-per-billion accuracy [17] and similar measurements with heavy highly charged ions, such as $^{209}Bi^{82+}$, have been foreseen.

An important feature of Penning traps, especially the ones that operate at cryogenic temperatures, is the ability to cool the confined particles. In doing so, the uncertainties arising from the Doppler effect are reduced significantly. Among many cooling techniques available for trapped particles, resistive cooling is a primary choice in many experiments, such as ARTEMIS. Resistive cooling is based on the interaction of the image current induced on the trap electrodes by the charged trapped particles and the effective parallel resistance of the RLC detection circuit that connects these electrodes and form a dissipative element. The resistive cooling effect is proportional to the square of the ion charge q, hence a good choice for highly-charged-ion cooling. Using this cooling technique, temperatures as low as the electronic noise temperature of the detection system, typically $4\,\mathrm{K}$, can be achieved [15]. A more efficient cooling technique commonly used is laser cooling, however due to a lack of proper optical transitions, this cooling approach is not applicable for highly charged ions. Instead, sympathetic cooling of the highly charged ions using calcium or beryllium laser-cooled ions is a good option to be considered in the future [18].

A number of theoretical and experimental studies have been dedicated to characterization of resistive cooling behavior of a single ion or an ion cloud with a limited number of particles

(figure 5.5); however, in the case of ARTEMIS the number of desired particles for the double resonance spectroscopy is considerably higher (of the order of 10^5). This circumstance raised the need to perform an in-depth study of the cooling behavior of an ion ensemble with considerable number density. The theoretical ground for this experiment was laid by J. Steinmann [19], who generalized the concept of the effective electrode distance D in his PhD thesis. Adapting his calculation for D and implementing the geometrical parameters involved in the creation trap of ARTEMIS, first a theoretical estimation of the resistive cooling of a typical ion ensemble was performed. Afterwards, the refreshed understanding of the resistive cooling behavior was put to the test in three different cases: (1) an extremely hot and populated ion cloud of mixed argon charge states directly after creation, (2) a purified Ar^{13+} ion ensemble and (3) a mixed-charge-state ion cloud with a majority of Ar^{13+}, which had been initially cooled and excited afterwards.

This thesis is structured into seven chapters. After this brief introduction, a look into the theoretical motivation leading to the ARTEMIS setup and the adaptation of the Penning trap concept for double-resonance spectroscopy is presented in chapter 2. Afterwards in chapter 3, the concept of an RLC-detection system, development and upgrade of the detection system are discussed. The experimental setup has been discussed in detail in some of the previous reports, e.g. [20, 21], therefore a brief review alongside minor updates of ARTEMIS are stated in chapter 4. The theoretical concept of ion temperature and cooling, with focus on resistive ion cooling, is discussed in chapter 5. Furthermore this chapter includes the result of calculation of the effective electrode distance D (section 5.2.3.4). Finally, the studies of ion ensemble preparation and three case studies of resistive ion cooling are presented in chapter 6. This thesis finishes with brief take-home messages and future outlook.

CHAPTER

TWO

THEORETICAL MOTIVATION, FUNDAMENTALS OF PENNING TRAPS AND ARTEMIS

Studying the magnetic moment (or, equivalently, the g-factor) of elementary particles, such as electrons and protons, independently or in a physical system has proven to yield remarkable results; for instance high-precision measurements leading to considerable improvements of the fundamental constants [1, 22] and studies of anti-particles and anti-matter [23, 24]. These studies are used in a variety of physics contexts; ranging from fundamental physics such as charge-parity-time (CPT) invariance [25, 26] and test of quantum electrodynamics (QED) [27, 28] to practical applications e.g. solid state physics electron spin resonance (ESR) measurements [29, 30].

Ever since the early stages of QED theory [31], this theory has been challenged by anomalies observed in measurements [32, 33]. Nevertheless, the strong framework offered by this theory has resolved these discrepancies and evolved to one of the most advanced and precise theories available [34, 35]. Contemporary computation has enabled tackling far more complex problems in the framework of QED with a high level of precision [36, 37]. To match this precision experimentally, measurement schemes such as the HARVARD UNIVERSITY g-factor setup [38], the MAINZ-HEIDELBERG g-factor measurement [12] and ARTEMIS in the framework of the HITRAP collaboration are required [39].

2.1 Theoretical Motivation of ARTEMIS

The matter at hand at ARTEMIS is the magnetic moment of the bound electron in highly charged ions (HCI) [13, 36, 11]. The significant difference of the g-factor of free electron [38] and of a bound electron in highly charged ions is not surprising, since the high electromagnetic fields (up to $10^{16}\,\mathrm{V\,cm^{-1}}$) of the nucleus affect the bound electron considerably[11].

The largest source of difference between free and bound electron $g-$factor is the so-called relativistic correction, the Breit term [40]. The next-biggest contribution in this difference is from the bound-state QED which scales with the square of the nuclear charge number Z. In case of a bound system, in contrast to a free electron, the level scheme is like in any atom or ion, but the high charge state (high field strengths) change the transitions. The ground-state energy of the hyperfine structure (HFS) splitting is proportional to Z^3 (the nuclear charge number) and the fine structure splitting depends on Z^4 [41], which makes these transitions for certain medium-heavy ions in the optical regime, for instance $^{209}Bi^{82+}$ [5]. The magnetic moment is commonly expressed by a dimensionless value known as the g-factor

$$\mu = -g\mu_B \frac{\vec{J}}{\hbar}. \tag{2.1}$$

Here μ_B is the Bohr magneton $\mu_B = e\hbar/(2m_e) = 9.27400912(23) \times 10^{-24}\mathrm{J/T}$ and the minus sign indicates the opposite orientations of μ and the angular momentum $\vec{J}$. In case of a bound electron $\vec{J} = \vec{L} + \vec{s}$, where $\vec{L}$ and $\vec{s}$ are the orbital angular momentum and the spin of the bound electron, respectively. Due to the spin-orbit coupling the effect of direct determination of either s or L is not possible when dealing with a bound electron, therefore hereafter the magnetic moment under discussion is referred to as g_J-factor. The determination of the g_J-factor values are ensured through the measurement of the Larmor frequency ω_L, the precession frequency of the electron spin in an external magnetic field B_0, where ω_L reads

$$\hbar\omega_L = \mu B_0 = g_J \mu_B B_0, \tag{2.2}$$

such that for a precise determination of the g_J-factor an accurate knowledge of B_0 is required. Generally the value of B_0 is obtained through the cyclotron frequency of a single ion in the trap, $\omega_c = qB_0/m_i$ (section 2.2.1), with q being the ion's electric charge and m_i its atomic mass. Figure 2.1 is a schematic of the parameters used to perform a g-factor measurement in a hydrogen-like highly charged ion.

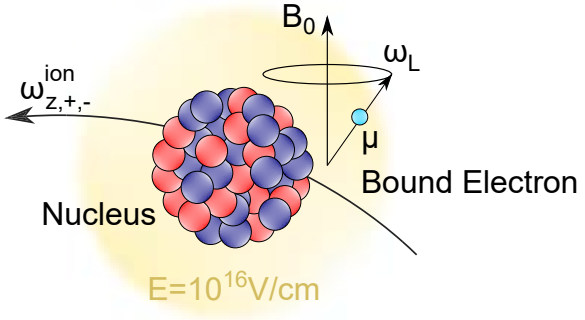

Figure 2.1: Schematic overview of the parameters involved in measurement of the magnetic moment. The precession of the electron spin about the magnetic field B_0 is denoted by the ω_L and the cyclotron frequency is denoted by ω_c. Please keep in mind that $\omega_c \ll \omega_L$. The extreme electric field of the nucleus $E = 10^{16}\mathrm{V/cm}$ modifies the g_J-factor noticeably.

Stern-Gerlach-Type g-factor Measurement Scheme

Conventionally, for precision measurements of the magnetic moment of bound electrons, a Stern-Gerlach-type g-factor scheme is utilized. This technique is based on the measurement of ω_L using the probability of spin state transitions ('spin flips') during a frequency scan of the driving microwave radiation. In order to determine the spin state, a continuous Stern-Gerlach effect in a magnetic bottle is applied [42, 43]. The presence of the magnetic bottle makes the oscillation frequencies dependent on the spin state, such that it can be determined from a radio-frequency measurement. The magnetic bottle introduces a new degree of inhomogeneity in the magnetic field, thus limiting the final precision of the measured magnetic moment [11]. By applying a double trap technique the effect of the residual field of a magnetic bottle can be minimised [2], resulting in outstanding precision measurements [44, 26]. Generally, one confined particle is enough to perform this measurement, thus reducing the systematic errors and increasing the precision of the measurement [11].

This technique is suitable for HCI with zero nuclear spin [15], thus to measure the bound electrons and nuclear magnetic moment in an atomic system with non-zero moment nuclei a different measurement scheme is required, namely the laser-microwave double-resonance spectroscopy technique.

Laser-Microwave Double-Resonance g-factor Measurement Scheme

The so-called laser-microwave double-resonance technique complements to the Stern-Gerlach-type measurements. This approach has been successfully applied for measuring the g_J-factor of atoms and singly charged ions [45]. ARTEMIS is the first adaptation of this concept for measurement of magnetic moments and Zeeman transitions for HCI [14, 17]. Application to the optical hyperfine structure splitting in a highly charged ion with non-zero nuclear spin and the microwave Zeeman splitting of the levels yields precise information of the involved magnetic moments. As a benefit of the double-resonance technique the magnetic moment of nuclei and the bound electron can be obtained simultaneously in one Penning trap. Furthermore this technique enables one to measure nuclear magnetic moments in absence of diamagnetic shielding. The Larmor frequency is probed by a scanned microwave signal and detected via laser spectroscopy of the corresponding fine or hyperfine structure [14, 17].

The first HCI chosen for studies is $^{40}Ar^{13+}$, a boron-like ion with a spin-less nucleus. At this instance the $1S$ and $2S$ shells are fully occupied. Nevertheless the $2p$ valence electron is sufficient for the double-resonance scheme. This electron exhibits a fine-structure doublet due to spin-orbit coupling, $2^2P_{1/2}$ and $2^2P_{3/2}$. This degeneracy is lifted by an external magnetic field (in this case the $B = 7\,\mathrm{T}$ of the Penning trap), which gives access to six fine-structure transitions. In addition, the Zeeman splittings are present, with their corresponding transi-

tions in the microwave regime and equivalent to the Larmor frequency. Due to the mentioned effect of the nucleus of the HCI on the bound electrons, the fine-structure splitting between $2^2P_{1/2}$ and $2^2P_{3/2}$ of $^{40}Ar^{13+}$ is optically accessible with a $441.256\,\mathrm{nm}$ laser [46] (See section 3.6); which translates to an energy of approximately $2.8\,\mathrm{eV}$ for this level splitting. These transitions are summarized in figure 2.2.

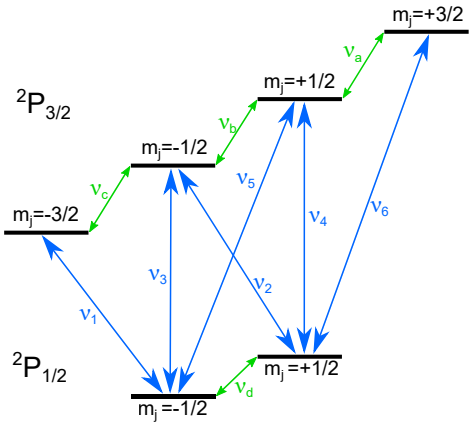

Figure 2.2: Level diagram of possible transition of $2^2P_{1/2} - 2^2P_{3/2}$ for Ar^{13+} at 7 T. Here the six optical transition between fine-structure levels are shown in blue (ν_1 to ν_6) and the microwave transitions between the Zeeman splittings levels are demonstrated in green (ν_a, ν_b , ν_c and ν_d). Except ν_d which has transition frequency of 65 GHz, the other three are equal to the Larmor frequency (≈130 GHz)

The double-resonance scheme utilized at ARTEMIS on $^{40}Ar^{13+}$ is depicted in figure 2.3. As the first step the closed optical cycle between $|1/2,+1/2\rangle$ and $|3/2,+3/2\rangle$ is probed using a laser with frequency ν_6, which populates the $|3/2,+3/2\rangle$ state with roughly half of the electrons. The excited electrons spontaneously start to decay via a magnetic dipole (M1) transition back to $|1/2,+1/2\rangle$, creating a fluorescence signal with lifetime of $9.573(6)\,\mathrm{ms}$ [47]. Thereafter, while monitoring the fluorescence signal with a high-quantum-efficiency detector (Section 3.6); a tunable microwave signal around ν_a is transmitted inside the spectroscopy trap. In the instance that this frequency matches the ω_L resonantly the excited electrons populate the $|3/2,+1/2\rangle$ state resulting in a dark state through a secondary transition to $|1/2,-1/2\rangle$. Obtaining the ω_L in this fashion and measuring the ω_c through a RLC detection system (section 3.1), from equation 2.1 one obtains

$$g_J = \frac{\hbar\omega_L}{\mu_B B_0} = \frac{\hbar\omega_L q}{\mu_B \omega_c m_i} = 2\frac{\omega_L q m_e}{\omega_c m_i e} \tag{2.3}$$

where m_e and e are the mass and the charge of the electron, respectively.

Higher-order Nonlinear Zeeman Effect

As a by-product of the double-resonance measurement scheme, the higher-order nonlinear Zeeman splittings can be measured at ARTEMIS. These energy levels reveal themselves typically in high magnetic fields, for example at the $7\,\mathrm{T}$ magnetic field of ARTEMIS. Since a good theoretical knowledge foundation for boron-like argon is already available, it seems to be a good candidate for studying this effect in HCI. Figure 2.4 shows the level scheme of

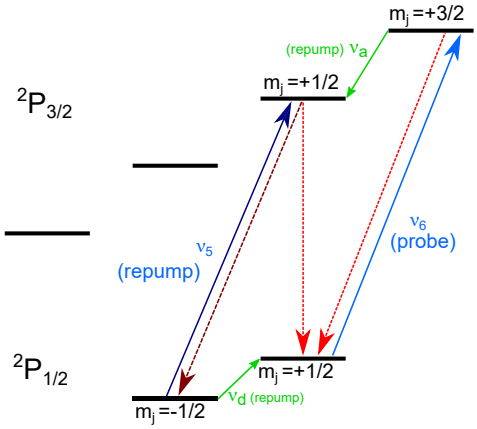

Figure 2.3: The level structure foreseen for the laser-microwave double resonance spectroscopy technique in P-doublet boron-like ion (Ar^{13+}). The ν_6 is the optical probed transition and the ν_a is the microwave sub-level transition. The red arrows depict the possible decays. The dark red arrow shows the decay leading to dark state and the dark blue arrow is the required repump laser to bring the electron back to the fluorescing state.

the Zeeman splitting for Ar^{13+}. The Zeeman splitting beyond its equidistant first order loses symmetry and a perturbative correction to account for this field-driven phenomenon reads as

$$\Delta E_A = \Delta E_A^{(1)} + \Delta E_A^{(2)} + \Delta E_A^{(3)} + ..., \tag{2.4}$$

where $|A\rangle = |J, m\rangle$ is the 2^2P_J state with angular moment J and its projection m_J. The first order shift (regular Zeeman splitting) can be related to g_J as follows

$$\Delta E_A^{(1)}(B_0) = g_J \mu_B B_0. \tag{2.5}$$

Higher order shifts and their relation with g_J are presented in full detail in references [48, 20]. Figure 2.4 shows the frequency shift caused by these higher-order Zeeman effects and their relative frequency shifts in the case of Ar^{13+}. In the final stage of the precision measurement of the g_J-factor of the bound electron in Ar^{13+} these contributions should be considered [48]. As depicted in figure 2.4 some of these contributions are within the expected resolution of the measurement (kHz and above), and in [20] schemes to disentangle them from the desired frequencies are presented.

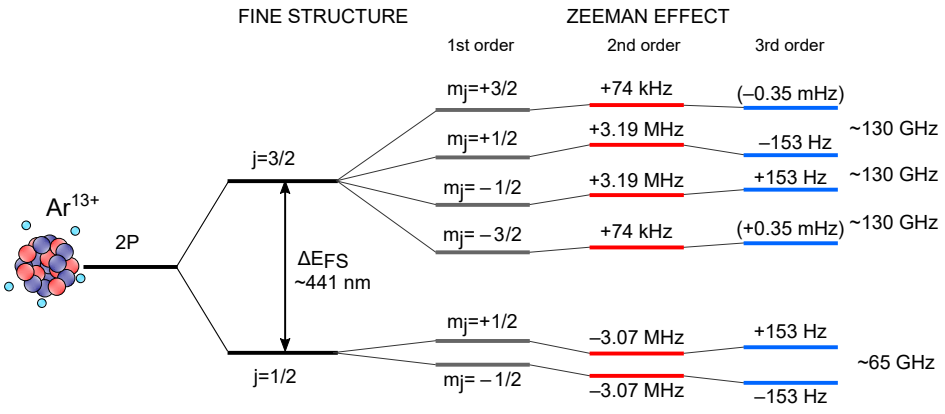

Figure 2.4: Higher-order Zeeman effect energy level lay-out with their relative transition frequencies for Ar^{13+}. Beside the optical transition of the Fine-structure the oder transition lay in the microwave regime.

2.2 Fundamentals of Penning Traps

Over the past half-century H.G. Dehmelt's vision of using Penning traps as devices for high-accuracy spectroscopy measurements of confined particles [49] has achieved many milestones. The advancement of trapping and cooling techniques [11] has turned them into important tools for a variety of modern measurements including fundamental physics experiments, mass spectroscopy of exotic ions and quantum computing, just to name a few [50].

ARTEMIS stands for "**A**symmet**R**ic **T**rap for the measurement of **E**lectron **M**agnetic moments in **I**on**S**", which is a combination of two Penning traps tailored for the double-resonance measurement scheme and connectivity to the HITRAP facility [51]. These two traps are the spectroscopy trap (ST) and the creation trap (CT). The former has the purpose of carrying out the spectroscopy measurement and the latter for commissioning reasons, is based on a built-in ion source. In this chapter an introduction of Penning trap principles and ion motions will be given (section 2.2.1). A further detailed look into open-end-cap Penning traps with cylindrical electrodes follows the discussion (section 2.2.2), which is the basic concept applied in the ARTEMIS design introduced in section 2.3. This section is summed up by introducing frequency shifts in a Penning trap and an example about ARTEMIS (Section 2.4).

2.2.1 Charged Particles in an Ideal Penning Trap

To confine a particle with charge q and mass m in three dimensions of space, a superposition of a homogeneous magnetic field $\vec{B} = (0, 0, B)$ and an electrostatic quadrupole field of $\vec{E} = -\nabla\Phi$ is required, where Φ reads

$$\Phi(x, y, z) = \frac{U_0}{2d^2}(2z^2 - x^2 - y^2). \tag{2.6}$$

This configuration is known as a Penning trap. Here $d = \frac{1}{2}\sqrt{\rho_0^2 + 2z_0^2}$ is the characteristic dimension of the trap. The $\vec{B}$ field is responsible for radial confinement and the electrostatic quadrupole field traps particles axially (parallel to the z-axis). Establishing such a potential in the center of the trap requires at least three hyperbolically shaped electrodes—a ring electrode and two end-cap electrodes. The end-caps are connected and a DC potential is applied between them and the ring, which in equation 2.6 is denoted as U_0. Figure 2.5a shows such a trap configuration, where the distance from the trap center to the ring and the end-caps are depicted as ρ_0 and z_0, respectively.

Assuming the charged particle has a velocity of $\vec{v}$ it will experience a Lorentz force

$$\vec{F} = q(-\nabla\Phi + \vec{v} \times \vec{B}), \tag{2.7}$$

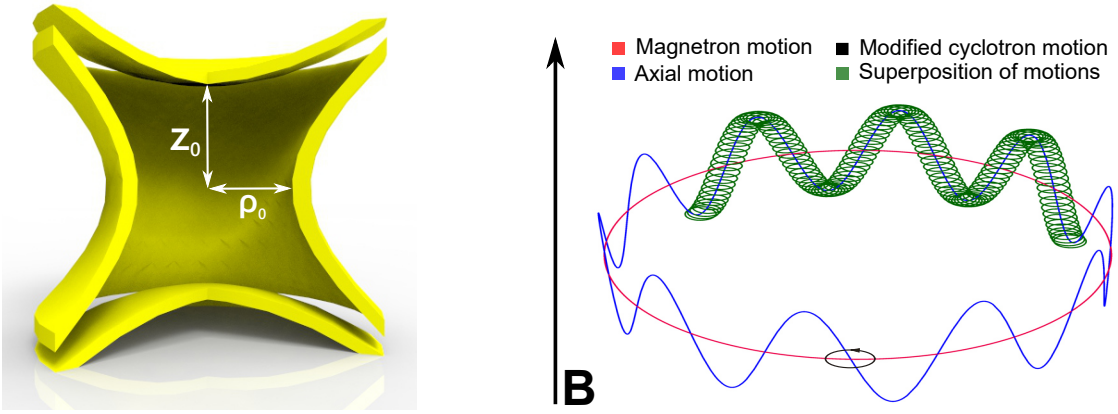

(a) (b)

Figure 2.5: (a) An ideal Penning trap with hyperbolic shaped electrodes, demonstrating ρ_0 and z_0 the distance from the trap center to the ring and the end-caps, respectively. (b) Three fundamental motions and the superposition of them for a charged particle in a perfect harmonic Penning trap.

which translates to a simple harmonic motion in the axial direction with the following axial angular frequency [52]:

$$\omega_z = \sqrt{\frac{q\,|U_0|}{md^2}}. \tag{2.8}$$

Although the radial motion appears to be more complex ($z = 0$ plane), a cyclotron motion caused by the $\vec{B}$ field with a cyclotron frequency follows

$$\omega_c = \frac{|qB|}{m} \tag{2.9}$$

and can be formalized by introducing a complex variable $\rho = x + iy$. Hence, the radial equation of motion of the trapped particle is

$$\ddot{\rho} = -i\omega_c\dot{\rho} + \frac{\omega_z}{2}\rho, \tag{2.10}$$

which can easily be shown that its solution is a superposition of two circular motions with the following frequencies:

$$\omega_+ = \frac{1}{2}(\omega_c + \omega_1), \tag{2.11}$$

$$\omega_- = \frac{1}{2}(\omega_c - \omega_1), \tag{2.12}$$

with

$$\omega_1 = \sqrt{\omega_c^2 - 2\omega_z^2}.$$

The ω_+ is known as the modified cyclotron frequency and ω_- is known as the magnetron frequency. Figure 2.5.b demonstrates the trapped charged particle motions discussed in this

section.

The cyclotron frequency is one of the most important parameters measured in Penning trap experiments (e.g. ARTEMIS). For an ideal trap, with no imperfections, ω_c is given by $\omega_c = \omega_- + \omega_+$. Due to the difficulties in producing perfect trap electrodes, violating the ideal trapping potential is inevitable in reality. Nevertheless, it has been shown by Brown and Gabrielse [42] that

$$\omega_c^2 = \omega_-^2 + \omega_+^2 + \omega_z^2, \tag{2.13}$$

holds true regardless of first order trapping field tilts and ellipticities and misalignments. This equation is known as the invariance theorem and introduces a practical scheme for accurate ω_c measurements.

2.2.2 Open-Endcap Penning Traps with Cylindrical Electrodes

To avoid the difficulties of machining hyperbolic electrodes, creating optical access and openings for charged particle loading, different compositions of electrodes have been already used for quite a long time [53]. One suitable geometry for precision measurement is a trap with cylindrical electrodes, including anharmonicity compensation electrodes. Although closed end-caps can provide the highest harmonicity in such a Penning trap, long open-ended electrodes which are about four times longer than z_0 can also simulate closed-end-caps. The benefit of long open end-caps is optical and charged particle loading access (See Figure 2.6).

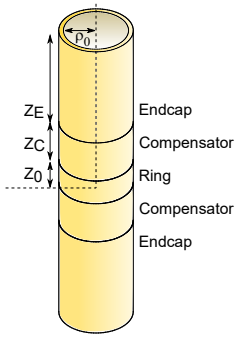

Figure 2.6: An electrically compensated open-end Penning trap.

The electrostatic quadrupole potential in equation 2.6 can be rewritten in terms of Legendre polynomials, $P_k(\cos\theta)$, as

$$\Phi = U_0 \sum_{k=0}^{\infty} C_k (\frac{\rho}{d}) P_k(\cos\theta). \tag{2.14}$$

Here $\cos\theta = z/\sqrt{\rho^2 + z^2}$ with ρ and z as the radial and axial distances from the trap center, respectively. This equation holds best near the center of the trap and due to azimuthal symmetry in a cylindrical trap in the xy-plane of $z = 0$, all the odd coefficients will be zero. C_0 has no effect on the ion motion since it is a constant potential offset, whereas C_2 is the dominant term in an ideal quadrupole trap and is the only non-zero term. In such a trap the

axial frequency reads as

$$\omega_z^2 = \frac{qU_0}{md^2}C_2. \tag{2.15}$$

The C_4 and C_6 are mainly responsible for the anharmonicity, and can be reduced to negligible values by applying a potential (U_C) to the compensation electrodes. For any given C_k coefficient of 2.14 one can show

$$C_k = C_k^{(0)} + D_k\frac{U_c}{U_0}, \tag{2.16}$$

where $C_k^{(0)}$ and D_k are determined by the geometrical properties of the trap. By tuning U_C/U_0 ratio the C_4 term can be set to zero, which is the leading term in the anharmonicity of the potential. Tuning this ratio can simultaneously change the C_2 term, unless the ρ_0/z_0 ratio is set in manner that $D_2 = 0$; Thus making the C_2 term independent of U_C. Such a trap is called an orthogonalized trap and it can be easily shown that in such a trap the ω_z does not vary with U_C [42].

2.3 ARTEMIS and its Two Traps

The ARTEMIS trap system is made out of two connected Penning traps, a Creation trap (CT) and a Spectroscopy trap (ST). Figure 2.7.a depicts a CAD drawing of the two traps. The CT includes the electrodes between H19 to H8, whereas the ST starts from S6 and goes on to S1. The two traps are connected to each other by a transport electrode T7. The electrodes are made out of OFHC copper (oxygen-free high thermal conductivity copper), with an inner diameter of $17.51\,\mathrm{mm}$ (for the CT and the ST electrodes). They have a gold-plated protection layer of less than a micrometer with a $20\,\mu\mathrm{m}$-thick diffusion barrier of silver (with the exception of S1).

For electrical insulation, in between the CT electrodes $3\,\mathrm{mm}$-thick Macor spacer rings and between the ST electrode $3\,\mathrm{mm}$ thick sapphire spacer rings have been implemented. The electrodes and the spacers are put in order on top of each other and kept together using six copper rods as shown in figure 2.7.b. Using the S6 electrode the entire assembly is mounted on the UMF[1] with four other copper rods. It is of utmost importance to keep the axis of the trap perpendicular to the plane of the UMF, while the axis of the UMF is also set to be parallel to the B-field (section 4.2.1).

[1] Unterer Montageflansch: A German expression which translates into lower construction flange

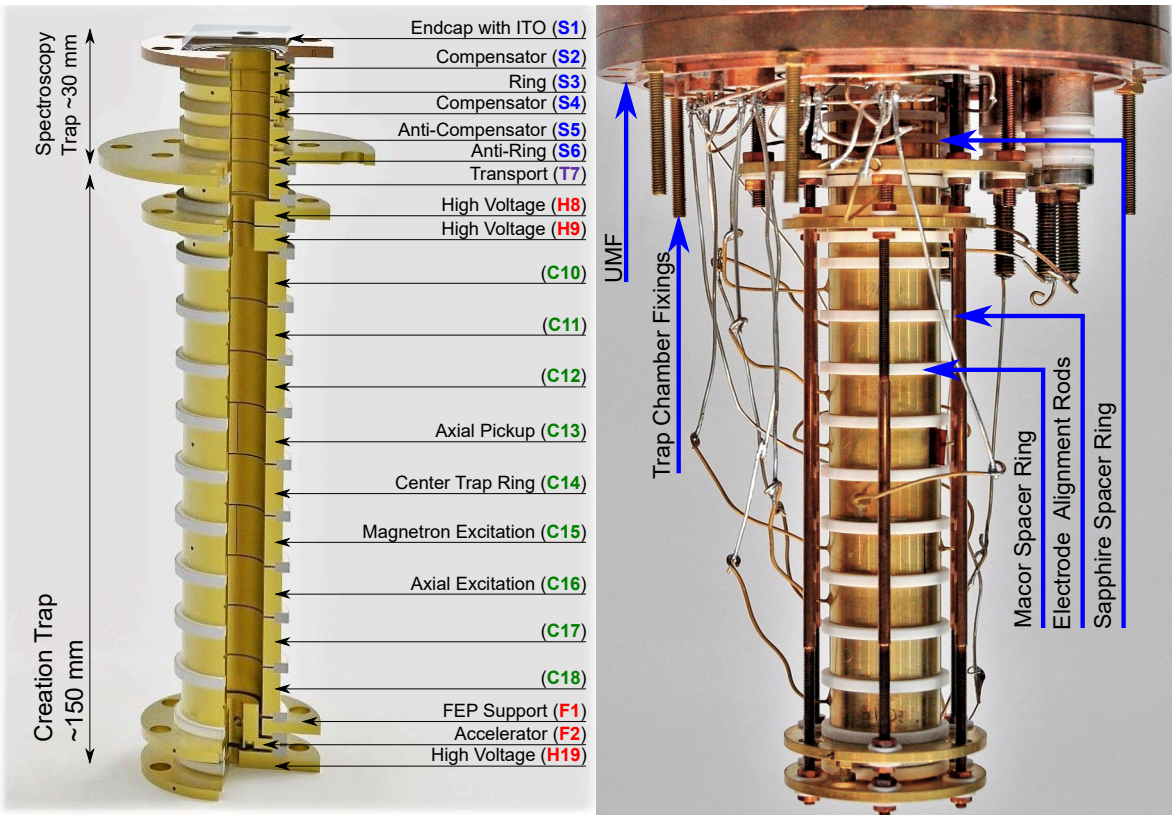

(a) (b)

Figure 2.7: (a) A section view of the two traps of ARTEMIS, including the conventional names used on daily a basis. Please notice some of the important functions assigned to the electrodes. (b) A photo of ARTEMIS mounted on the UMF and including the trap wiring.

2.3.1 Spectroscopy Trap (ST), the Half-open Trap

While designing the ST, four main goals were required to be attained. First, for an efficient laser-microwave double resonance spectroscopy it is required to maximize the fluorescence detection. Second, since the aim is to perform a precision measurement, a high electrostatic harmonicity is essential. Third, loading the ST with HCI should be possible. Fourth, the trap size should be chosen in a manner that the electronic detection would be still efficient. A conventional cylindrical Penning trap with long end-caps limits the optical solid angle to $\sim 0.2\,\mathrm{sr}$, hence to optimize the solid angle an indium tin oxide (ITO) coated glass window is used as a closed-end-cap (figure 2.8). The ITO window is optically transparent and at the same time electrically conductive, which makes the end-cap optically open but electrically closed [54]. As illustrated in figure 2.9, this modification has resulted in optimization of the solid angle to $\sim 2\,\mathrm{sr}$.

On the other end of the ST, the end-cap is required to be physically open and connected to the CT. Utilizing a long end-cap was not desirable, because it makes adiabatic transport challenging. Instead, two cylindrical electrodes identical to the ring electrode and compensator electrode were used to mimic the potential for a closed end-cap. Biasing these two electrodes,

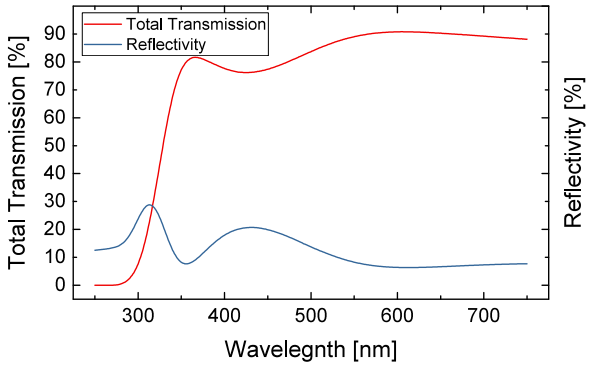

Figure 2.8: Total transmission and reflectivity of the ITO-coated window as a function of wavelength, according to the data-sheet provided by the manufacturer [54].

the anti-ring and the anti-compensator, with opposite voltages of their counterparts creates a so-called 'antitrap'. The antitrap is a mirror image of the closed trap, and due to symmetry at the position, where there should be a closed-end-cap, the effective potential behaves as if there was one. This setup of the end-caps creates the structure known as half-open trap and further technical details and calculations can be found in [16, 20]. Figure 2.9 shows the different types of traps discussed.

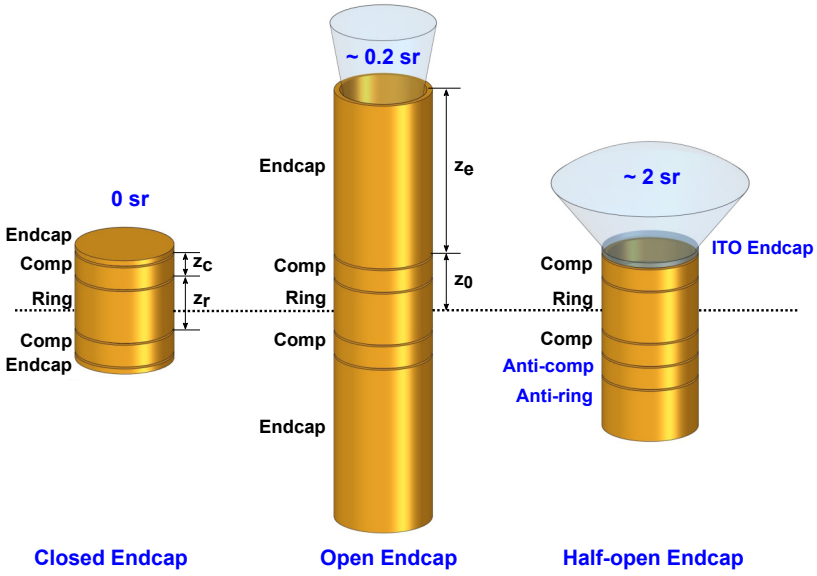

Figure 2.9: A comparison of closed-, open-end-cap and half-open Penning traps. The solid angle improvement and the antitrap concept are demonstrated here.

The ST trap is built around S3 as the ring electrode, with $z_0 = 9.008$ mm and $\rho_0 = 8.704$ mm. Hence the C_2 and C_4 coefficients read 0.5299 and < 0.001, respectively. Table 2.1 shows the values of associated ion motion frequencies, calculated by applying these parameters for a given ring voltage. Beside the fact that the S3 electrode is four-fold segmented, the other electrodes of the ST have the same physical dimensions. The ring electrode is segmented, so that in the future it can be used to drive a rotating-wall technique [55]. To isolate different segments from each other, sapphire balls were placed in special grooves considered in the design (Fig. 2.10.a).

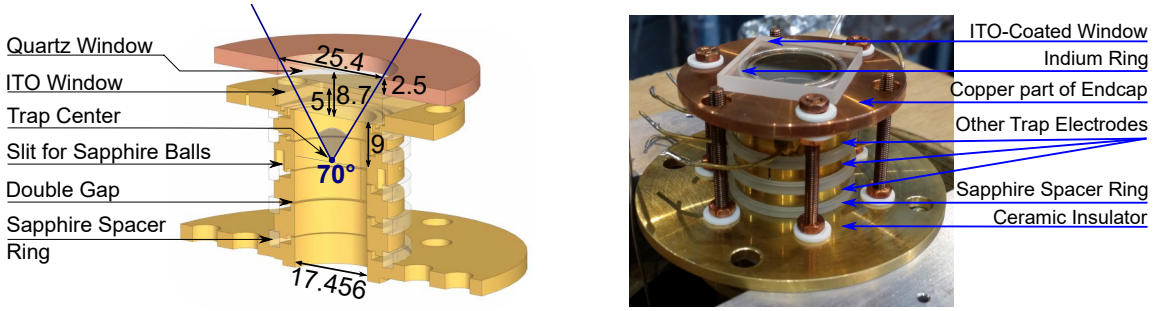

(a) (b)

Figure 2.10: CAD drawing (a) and a photo of the ST (b). Indicating the different parts of the trap with their sizes included and the ITO-coated windows utilized as the end-cap. (a) The large optical solid angle of the ST is apparent in this figure. (b) The structure used to mount the ITO-coated window using an indium ring is shown.

The biasing voltages of the ST electrodes will be supplied in the future by the UM1-14-28 Stahl Electronics power supply. This device has 10 ppm accuracy and 0.004 ppm per minute fluctuations in the output voltage [20]. Currently, to increase the speed of changing the applied voltage the less accurate but faster HV 200-8 Stahl Electronics (output $\pm$ 200 V) is in use. Please note that, due to the limitation of the filter boards it is not recommended to bias the electrodes with more than ± 65 V.

An important modification that has been done on the ST, is replacing the metallic mesh end-cap of the ST reported in [20] with an ITO-coated conducting window. The details of this change is reported in [21, 56]. As a result of this change, the fluorescence transmission is predicted to improve significantly. Also measurements have shown the ability to use the ITO window as a Faraday cup detection system (Section 3.7).

Table 2.1: Different ion motion frequencies (ω_z, ω_c, ω_+ and ω_-) of various charge states of argon ions in ST for $B = 7.003$ T, $C_2 = 0.5299$ and $d = 7.714$ mm at a trapping potential of 39.3 V.

q	$\omega_z/2\pi$ [kHz]	$\omega_c/2\pi$ [MHz]	$\omega_+/2\pi$ [MHz]	$\omega_-/2\pi$ [kHz]
16+	581.041	42.9971	42.9932	3.92630
15+	562.590	40.3098	40.3059	3.92633
14+	543.514	37.6225	37.6186	3.92635
13+	523.743	34.9352	34.9312	3.92638
12+	503.196	32.2478	32.2439	3.92642
11+	481.774	29.5605	29.5566	3.92646
10+	459.353	26.8732	26.8693	3.92652
9+	435.781	24.1859	24.1820	3.92658
8+	410.858	21.4986	21.4946	3.92666
7+	384.322	18.8112	18.8073	3.92676

2.3.2 Creation Trap (CT)

The Creation trap at ARTEMIS has been designed to fulfill three purposes:

- An integrated ion source is beneficial as it can be used to create medium to highly charged ions such as Ar^{13+}. The creation procedure will be explained in section 6.2. This function is chosen to be also used as the name of this trap.
- The CT can be used for in-flight ion capture of externally created highly charged ions up to H-like uranium.
- The benefits of a reservoir trap have been demonstrated [57]. It would be a big advantage to be able to store exotic, externally produced HCI in the CT and extract them as single charged particles or small clouds and transport them to the ST. Preparing a well defined ion cloud of HCI in the CT typically takes over a day, therefore it will be beneficial to extract only the required amount of ions from the ions that are stored in the CT. Alternatively, using the CT will allow to work off-line and extend the measurement periods on exotic HCI.

Table 2.2: Different ion motion frequencies (ω_z, ω_c, ω_+ and ω_-) of various charge states of argon ions in the CT for $B = 6.9995$ T (which is approximately 0.05% lower then the magnetic field in the ST), $C_2 = 0.5631$ and $d = 6.7275$ mm at a trapping potential of 55 V.

q	$\omega_z/2\pi$ [kHz]	$\omega_c/2\pi$ [MHz]	$\omega_+/2\pi$ [MHz]	$\omega_-/2\pi$ [kHz]
16+	817.865	42.9953	42.9893	7.77988
15+	791.895	40.3081	40.302	7.77997
14+	765.043	37.6209	37.6147	7.78008
13+	737.214	34.9337	34.9274	7.78021
12+	708.292	32.2465	32.2401	7.78035
11+	678.138	29.5593	29.5527	7.78052
10+	646.579	26.8721	26.8654	7.78073
9+	613.399	24.1848	24.1781	7.78098
8+	578.318	21.4976	21.4908	7.78129
7+	540.967	18.8104	18.8035	7.78169

At the CT three high-voltage electrodes H8, H9 and H19 can be used for in-flight capture of HCI in the future. Currently, in combination with the electron source they are biased to around $-1.5\,\mathrm{kV}$ to perform the creation procedure, where their role would be to confine the hot electrons emitted from the FEP (section 6.2). Besides the top three high voltage electrodes mentioned above, there are nine similar electrodes from C10 to C18 at the CT. They are used to form three, side-by-side mechanically compensated cylindrical traps[58]. Such a trap is made of a ring and two open end-cap electrodes. Also it should be mentioned that there are no compensation electrodes included in the design of the CT. Hence, it is required to

choose the $\rho_0 \approx 1.203 z_0$ for the ring, which results in $D_4 = 0$ for equation 2.16. To achieve this approximation, all the trap electrodes of the CT have $\rho_0 = 8.704\text{mm}$, $z_0 = 7.459\text{mm}$, resulting in $d = 6.838\text{mm}$, $C_2 = 0.5631$ and $C_4 = 0.001$. Ion oscillation frequencies of ten different charge states of argon ions in the CT based on these geometrical parameters are presented in table 2.2.

Furthermore, the anti-trap principle can be used at the CT to reach maximum possible harmonicity (e.g. biasing the even numbered electrodes at $-250\,\text{V}$ and the odd ones at $250\,\text{V}$). Currently most of the routines done are based on using the central trap with C14 as ring, while the axial resonator is connected to C13 and through the electrodes listed in table 4.2 excitations are possible. These electrode functions are also demonstrated in Figure 2.7. Finally the voltage of the C10 to C18 electrodes are biased using a Stahl Electronics HV 250-8, a device capable of providing $\pm\ 250\,\text{V}$.

2.4 Frequency Shifts in a Penning Trap

There are multiple causes for possible shifts of motion frequencies in a Penning trap, some related to the trap intrinsic properties and others to the trapped particle. Field misalignment and ellipticity are the main two reasons of shifts related to trap configuration; whereas image charge, image current and space charge effects can be considered as sources of shift related to the presence of charged particles. There are also other effects due to motions of the particles that lead to shifts, such as radiation damping, power shift of the Larmor frequency [11]. Nevertheless, they can be neglected at this stage of ARTEMIS measurements due to their magnitudes.

Except the space charge effect that by nature is related to a trapped ion cloud, the other effects are relevant also for an individual trapped particle. Hence, when studying an ion ensemble with an energy distribution across the confined particles, a frequency distribution from the energy-dependent effects are also expected. As a result, it is important to perform cooling procedures in advance to thermalise the ion ensemble to avoid such energy dependent shifts (chapter 5). Based on [11] and [59] the field induced and space charge shifts (which are considered to have a stronger effects) will be discussed in this section.

2.4.1 Field Misalignment and Ellipticity

Although many efforts are made to align the z-axis of a trap with the magnetic field in the ARTEMIS setup, it is estimated that tilt angles of the order of 0.1° are inevitable. If a non-vanishing ellipticity ε is present it adds a $-\varepsilon(x^2 - y^2)/2$ term to the electrostatic field of the

trap Φ, then equation 2.6 reads as [60]

$$\Phi'(x,y,z) = \frac{U_0}{2d^2}(2z^2 - x^2 - y^2 - \frac{1}{2}\varepsilon(x^2 - y^2)). \tag{2.17}$$

In the case of ARTEMIS the production of the trap electrodes are done with an accuracy of $\pm 0.01\,\mathrm{mm}$ resulting in maximum $\varepsilon = 0.0239$. As a result, the value of $\Phi'(x,y,z)$ in comparison to an ideal case on a disk geometry ($x \neq 0, y \neq 0$) on the trap center ($z = 0$) is maximum about 1%. Electrostatic field changes of these orders can be neglected, specially due to the fact that the modifications are smaller towards the center of the trap[2].

For any given angle θ between the z-axis and the magnetic field axis of the trap and a non-vanishing ellipticity ϵ of electric field, the shift can be calculated as [61]

$$\begin{aligned} \omega_z{}' &\approx \omega_z \left(1 - \frac{1}{4}(3+\varepsilon)\sin^2\theta\right) \\ \omega_\pm{}' &\approx \omega_\pm + 1 - \frac{1}{2}\omega_-(3+\varepsilon)\sin^2\theta. \end{aligned} \tag{2.18}$$

These tilts introduce modifications in the configuration of the electric field with respect to the magnetic field, hence resulting in a shift in the frequency. An important observation from the equations 2.18 is their energy-independence from the energy of the confined particles. Hence, while studying a frequency width for a thermal ensemble these shifts have no contribution. As presented already, the invariance theorem (equation 2.13) can be used practically to deal with shifts initiated from the trapping fields alignment issues.

2.4.2 Radially Symmetric Field Imperfections

The effects of field distortions have to be considered more carefully, including an improperly optimized magnet for precision measurements, an unstable power-supply or bad machining of the electrodes, just to name a few. An electric field imperfection in cylindrical traps appears as a non-zero C_4 coefficient of equation 2.14. The inhomogeneity of the magnetic field can be formulated by an expansion of the magnetic field similar to the expansion of the electric field in equation 2.14 with a quadratic component B_2 (the so-called magnetic bottle). Based on [11] the shift observed due to field distortion for ω_+, ω_-, ω_z and ω_L reads as

$$\begin{pmatrix} \Delta\omega_+/\omega_+ \\ \Delta\omega_z/\omega_z \\ \Delta\omega_-/\omega_- \\ \Delta\omega_L/\omega_L \end{pmatrix} = (M_E + M_B) \begin{pmatrix} E_+ \\ E_z \\ E_- \end{pmatrix}, \tag{2.19}$$

[2] calculations performed using WOLFRAM MATHEMATICA program.

where M_E and M_B are 3×4 matrices defining the oscillation frequencies related to the motional energies of the trapped particles, E_-, E_+ and E_z,

$$M_E = \frac{6C_4}{qC_2U_0}\begin{pmatrix} \eta^4/4 & -\eta^2/2 & -\eta^2 \\ -\eta^2/2 & 1/4 & 1 \\ -\eta^2 & 1 & 1 \\ 0 & 0 & 0 \end{pmatrix} \quad \text{and} \quad M_B = \frac{1}{2m\omega_-\omega_+}\frac{B_2}{B}\begin{pmatrix} -\eta^2 & 1 & 2 \\ 1 & 0 & -1 \\ 2 & -1 & -2 \\ -\eta^2 & 1 & 2 \end{pmatrix} \tag{2.20}$$

Where $\eta = \omega_z/\omega_+$. Nonetheless, with the aid of the correction electrodes the effect of electric anharmonicities can be reduced significantly. Furthermore, the invariance theorem can also be applied for shifts due to electric field anharmonicities, but not for the shifts caused by the magnetic field.

2.4.3 Space Charge Effect

In case of a trapped ion ensemble, the charge of the cloud changes the trapping potential locally and shifts the oscillation frequency in comparison to the case of single confined ions. Also, since the charge of the particles decreases the depth of the trapping potential, the amount of the charge that can be trapped is limited. According to [62] for an ion cloud the shifted axial and radial frequencies are

$$\omega_z{}' = \omega_z\sqrt{1 - \frac{\omega_p^2}{3\omega_z^2}} \tag{2.21}$$

$$\omega_\pm{}' = \frac{\omega_c}{2}\left(1 \pm \sqrt{1 - (1 + \frac{2\omega_p^2}{3\omega_z^2})\frac{2\omega_z^2}{\omega_c^2}}\right) \tag{2.22}$$

respectively. It should be considered that the ion cloud has to be assumed to possess a roughly spherical space distribution. $\omega_p = (q^2n)/\epsilon_0 M$ is the plasma frequency with n being the number density, M the ion mass and ϵ_0 the vacuum permittivity. For an unmagnetized and cold plasma, this frequency is the natural frequency of collective oscillation of the plasma [63]. The change of plasma frequency in the CT at ARTEMIS versus the ion number are depicted in figure 2.11.a for five different charge states of argon as ion clouds of single species. Through a few simple steps from the two square-roots, the maximum ion density can be extract [11]

$$n^{(\max)} = \frac{\epsilon_0 B^2}{2M}. \tag{2.23}$$

This value is known as the Brillouin limit. If the assumption that the cloud is spherical is not considered, for any trapping potential that fulfills the stability criterion $2\omega_z^2 < \omega_c^2$, the Brillouin limit is accessible and typically of the order of 10^9 charge per cm^3. For trapping potentials that violate this condition the confinement is lost.

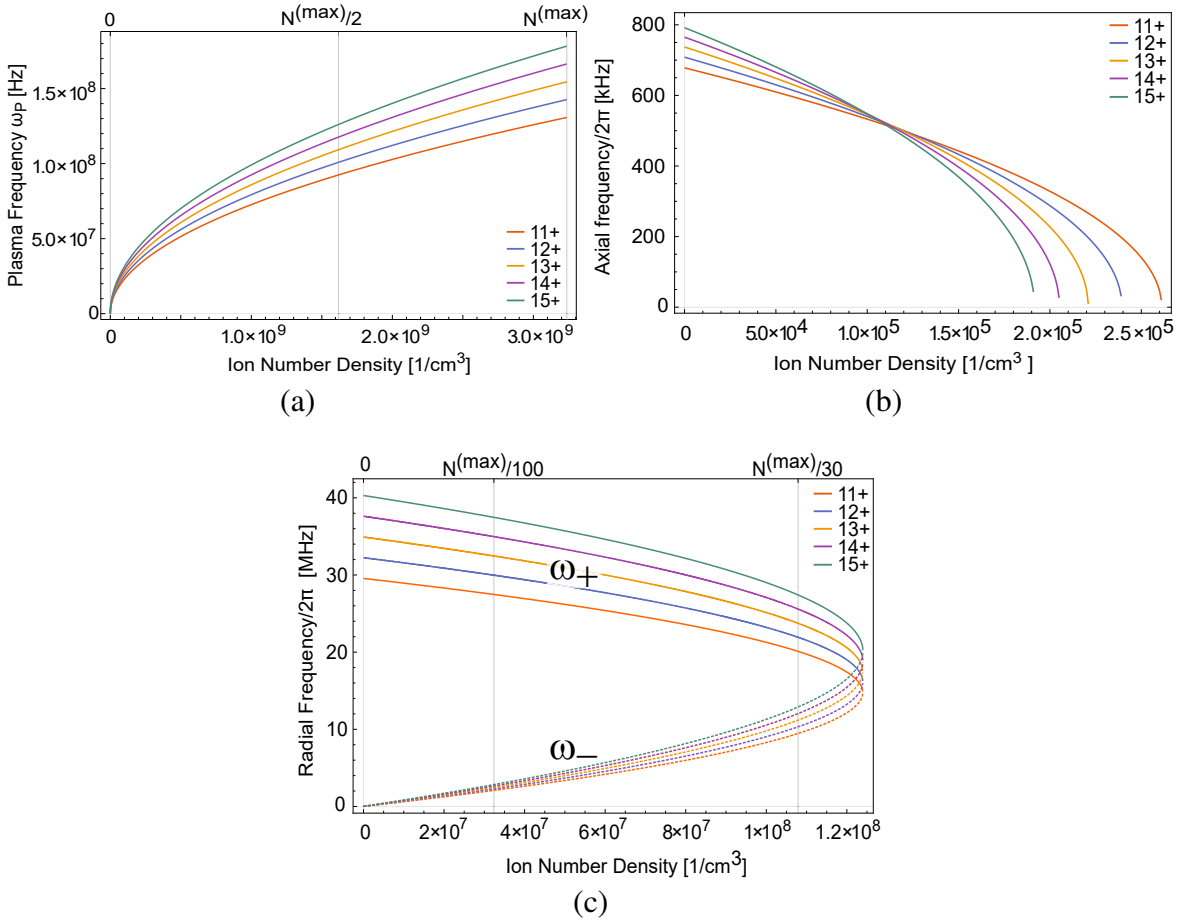

Figure 2.11: Space charge effect frequency shift calculation for 5 different charge states of argon ions in the CT stored at 55 V (a) ω_p evolution based on the ion number density (b) $\omega_z{}'$ shift due to space charge build-up by ion number density. (c) Radial frequency components, $\omega_+{}'$ and $\omega_-{}'$ change versus the ion number density. The solid lines illustrate the $\omega_+{}'$ and the dashed ones the $\omega_-{}'$. Also in (a) the position of the Brillouin limit (or the possible fraction of it) is marked.

Figures 2.11 demonstrates the space charge effects on the eigenfrequency of five different charge states of argon ions in the CT of ARTEMIS stored at 55 V. These simulations have been carried out using WOLFRAM MATHEMATICA. Initially the plasma frequency (ω_p) evolution based on the ion number density was calculated (2.11.a). Using the evolution curve of ω_p, the $\omega_z{}'$ due to space charge build up by ion number density was studied (2.11.b). Finally, as shown in the radial frequency components, the change of $\omega_+{}'$ and $\omega_-{}'$ versus the ion number density were simulated (2.11.c). As expected due to the electrostatic nature of these shifts by increasing the number of the particles the shifts becomes stronger for all three ion motion degrees of freedom. Furthermore, based on the same origin the shifts have higher slope for higher charge states. This difference in the slope for ω_z results in the convergence of this

frequency for different charge states around an ion number density of 1.1×10^5 charge/cm^3.

From the changes observed in the reduced cyclotron ω_+ and magnetron ω_- frequencies, the independence of the free cyclotron frequency $\omega_c = \omega_+ + \omega_-$ from the number of ions is clear. In addition, figure 2.11.c suggests that the Brillouin limit is about 1.2×10^8 Charge$/\mathrm{cm}^3$, which is more than an order of magnitude smaller than what is estimated using equation 2.23. However, in reality this discrepancy is due to the trapping potential $C_2 U_0 = 55\,\mathrm{V}$ applied in the calculation of the plot 2.11.c and by setting the trap potential to its maximum value, $250\,\mathrm{V}$, the discrepancy will be negligible.

CHAPTER

THREE

DEVELOPMENT AND UPGRADES OF THE DETECTION SYSTEM

High signal-to-noise ratio (SNR) detection systems have an inseparable role in Penning trap precision measurements such as ARTEMIS at HITRAP. The experiment has been designed to benefit from various detection schemes, destructive and non-destructive test methods. The two main non-destructive methods incorporated in ARTEMIS include the electronic detection system based on resonance RLC-circuit and the laser-optical detection system. Also the idea of using the ITO window as a Faraday cup has been realized at the spectroscopy trap (ST). The main focus of this chapter will be on the development and upgrades done on the electronic detection system. The laser-optical detection system has been described in detail in [64] and the ITO Faraday cup in [21]. Nevertheless, for the sake of completeness a short review of this system will be also presented.

3.1 Non-destructive Electronic Ion Detection

The oscillation of a confined particle in a Penning trap creates an oscillating image current I_p on the electrodes, which is typically of the order of fA to pA. To obtain detectable voltage signals a RLC-circuit is connected to the electrodes as resistances. To quantify the interaction between ions and RLC-circuit, one may regard the ion as an rlc-circuit itself and look at the properties of the combined circuit [65]. In an ideal Penning trap in the absence of dissipative elements like detection circuits, the ion motion is basically equivalent to an intrinsically undamped oscillator [65, 66]. It can be described in terms of a series LC circuit as follows

$$l_p \frac{dI_p}{dt} + \frac{1}{c_p} \int I_p dt = U_p, \tag{3.1}$$

where c_p and l_p are respectively the capacitance and the inductance of the equivalent LC circuit, if it were connected to a voltage of U_p. For a single-species ion cloud with a defined number of particles and total ensemble charge Nq, for any given radial coordinate ρ_i this image current reads as

$$I_p = Nq\frac{\dot{\rho}_i}{D_i} = \omega_i \frac{Nq}{D_i}\rho_i, \tag{3.2}$$

with ω_i being the oscillation frequency of a specific ion motion (ω_z or $\omega_\pm$) and D_i the effective electrode distance of that specific particle motion, which is determined by the geometry of the electrodes involved in detection of a motion (section 5.2.3.4)[67]. To detect this ion motion an inductor L is connected to the trap electrodes. Alongside its self-capacitance C_P and the capacitance of the trap C_T[1] it forms a parallel RLC (or resonator) circuit. Figure 3.1 shows this configuration and the electrical equivalent representation of the ion cloud and the RLC-circuit together.

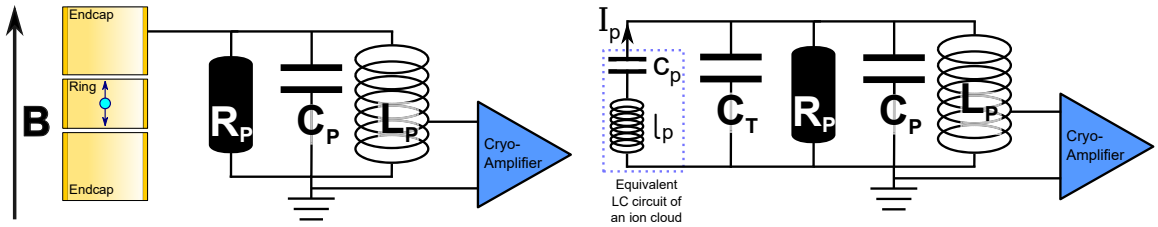

Figure 3.1: (a) Schematic representation of a parallel resonator circuit connected to cylindrical trap with ions loaded, where L, C_P and R_P are the circuits inductance, parasitic capacitance and effective resistance, respectively. (b) Equivalent circuit of trap ions and the RLC-circuit, which the ions are demonstrated as a series LC circuit and the trap as its capacitance.

For any given resonator circuit, the parameter known as the quality factor Q is the ratio between the stored and dissipated energy per angular cycle. In practice it can be demonstrated that the quality factor reads as

$$Q = \frac{\nu_0}{\delta\nu}, \tag{3.3}$$

where $\nu_0 = \sqrt{LC}/(2\pi)$ is the resonance frequency and $\delta\nu$ the full width at half maximum (FWHM) of the resonance spectrum, which typically is in the form of a Lorentzian function (Fig. 3.2). Practically, $\delta\nu$ can be measured at the position of $-3\,\mathrm{dBm}$ from the resonance frequency amplitude [68].

The impedance of the resonator circuit at its resonance frequency is considered as an effective parallel resistor that reads

$$R_P = \omega_0 LQ. \tag{3.4}$$

[1] Since a Penning trap is made of stacks of electrodes a capacitance can be easily calculated for it.

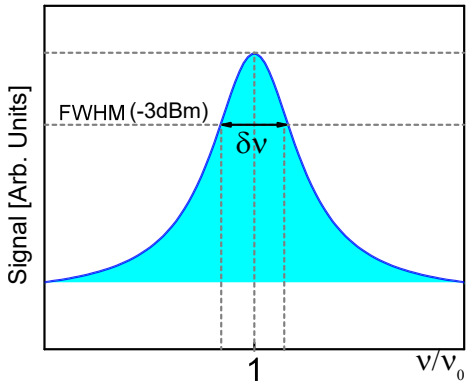

Figure 3.2: Typical Lorentz spectrum response of RLC-circuit, and the and the definition of the width $\delta\omega$ at -3 dBm from the resonance signal at $\omega/\omega_0 = 1$.

When the resonance frequency of the RLC-circuit matches the eigenfrequency of the single ion (or ion cloud) ν_i a voltage drop of

$$U_P = R_P I_p = \omega_0 L Q I_p \tag{3.5}$$

is observed, here I_p given by equation 3.2. Therefore a higher quality factor Q-factor and inductance L of the connected inductor is favorable and should be maximized (section 3.2.1). Eventually after amplification stages this voltage can be Fourier-transformed to the motional frequency spectrum of the ion(s).

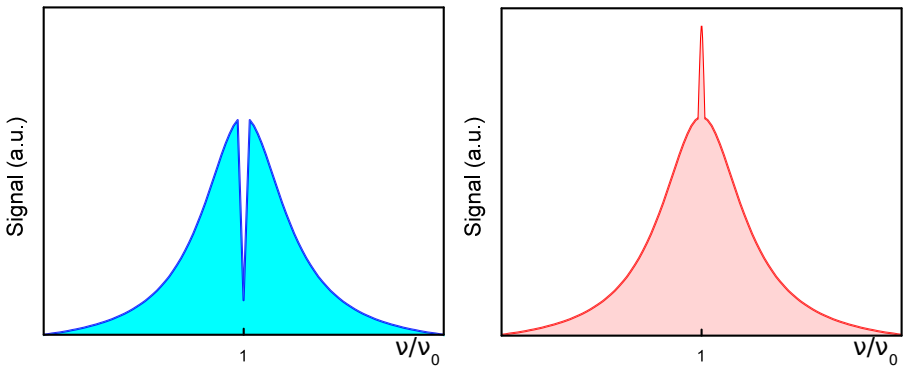

Figure 3.3: (*Left*) Signal of a resonant ion cloud with a motional temperature lower than the electronic noise temperature, known as an ion dip. (*Right*) A peak created by a resonant ion cloud with higher temperature in comparison to the electronic noise temperature.

Figure 3.3 demonstrates two important cases of the Fourier-transformed RLC signals including a single ion (or few ions with an in-phase oscillation) in resonance with the RLC detection system as a function of the frequency. If the motional temperature of the ions is lower than the electronic noise of the detection system, a dip is observed at the resonance frequency as in the left part of the figure; whereas a hot ion (cloud) with a temperature higher than the electronic noise will create a peak on the resonance spectrum (right). Considering the rlc model used to describe the ion motion, the dip observed is equivalent to a short circuit for the RLC detection system at the oscillation frequency ω_0. The FWHM of the axial motion

dip can be used to calculate the number of particles confined in the trap as follows

$$\Delta\nu_z = \frac{N}{\pi}\frac{1}{\tau_z} = \frac{N}{2\pi}\frac{R_P}{m}\frac{q^2}{D^2}, \tag{3.6}$$

with τ_z being the axial cooling time constant (section 5.2.3) and m the ion's mass.

For ion clouds with large number of particles the dip is too broad and shallow compared to the RLC-circuit noise of a high Q-factor circuit, hence this kind of ion signals are not observable at ARTEMIS. Instead the ion signal is obtained using mass-spectra readout technique (section 6.1).

3.2 Design Principles of the Non-destructive Detection System

A typical non-destructive detection system of Penning trap experiments , such as ARTEMIS, is composed of the following components which are connected to a spectrum analyzer capable of fast-Fourier-transform (FFT) analysis:

- Trap's pick-up electrodes
- Resonator
- Varactor-diode circuit board (if a tunable resonance frequency is required, e.g. at ARTEMIS)
- Cryogenic and room-temperature amplifiers
- Feedthroughs and connection cables.

The importance of the trap's pick-up electrodes and its effective electrode distance D in the non-destructive detection scheme will be discussed in section 5.2.3.4, hence the other parts of the detection system will be discussed in further detail here. Nevertheless they are an important parts of the detection system which in the future should be tested for the insertion loss. Due to the fact that all components contribute in the overall quality factor of the detection system, which one can write [69]

$$\frac{1}{Q_{\text{Dec}}} = \frac{1}{Q_{\text{Trap}}} + \frac{1}{Q_{\text{Res}}} + \frac{1}{Q_{\text{Var}}} + \frac{1}{Q_{\text{Amp}}} + \frac{1}{Q_{\text{Con}}} + ... \tag{3.7}$$

Here Q_{Dec} is the overall quality factor of the detection system and Q_{Trap}, Q_{Res}, Q_{Var}, Q_{Amp}, Q_{Con} are the quality factors of trap electrodes, resonator, varactor diode board, amplifier board, connectors, respectively. To this end, it is preferable to have the resonators as close as

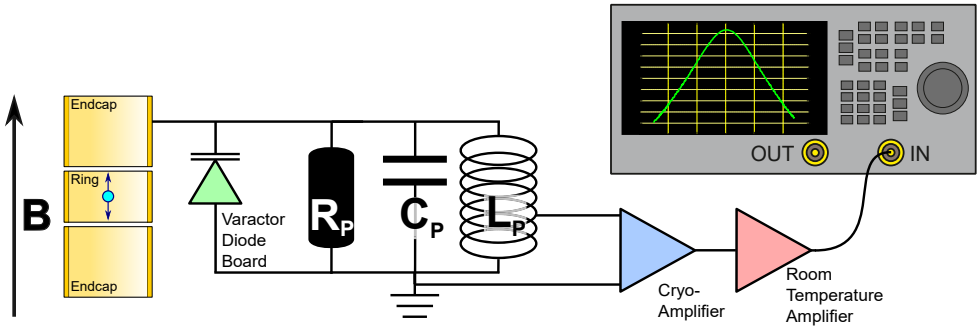

Figure 3.4: Schematic of a typical non-destructive detection setup for a measurement of ion motion in a Penning trap including the equivalent RLC-circuit.

possible to the trap electrodes, to eliminate introduction of any further components with low quality factor. Figure 3.4 shows the schematic overview of a typical non-destructive detection system.

3.2.1 Design Principles of the Resonator

As demonstrated already in equation 3.5, the ion voltage signal strength scales with the resonance resistance of the RLC circuit $R_P = \omega_0 L Q$. In order to achieve an high-sensitivity RLC detection circuit it is required to maximize the Q-factor and the inductance L of the inductor coil, while minimizing the parasitic capacitance, resulting in a high resonance resistance R_P. Space limitation, magnetic field and cryogenic environment are the main physical criteria that should be considered while designing the resonator. Two main designs of inductors are conventionally used in trap experiments such as ARTEMIS, namely helical and toroidal coil designs. An approach to making these coils is to wind a cable (normal-conducting or superconducting) around an insulator core, often made of polytetrafluoroethylene (PTFE), as depicted in figures 3.5 and 3.6. They are placed in a grounded housing made of OFHC copper to shield them from external noise as much as possible.

Although there have been efforts to accurately formulate the design of the resonator and its housing, designing and fabricating a resonator is mostly based on trial and error. Nevertheless there are some semi-empirical formulas extracted from [70, 71] for the helical resonator and from [72] for toroidal inductors, that can make this procedure easier.

3.2.2 Helical Resonator

The resonance frequency of a helical inductor reads as

$$\nu_0 = \frac{1}{2\pi\sqrt{LC}}, \tag{3.8}$$

where for a single-layer coil with air core the inductance follows from

$$L \approx \frac{D_1^2 \times N^2}{18D_1 + 40l_1}\,, \tag{3.9}$$

here D_1 and l_1 are the diameter and length of the coil in inches, respectively (figure 3.5) and the resulting inductance is given in µH. The number of turns N for such a coil to achieve the calculated inductance is immediately apparent. If a housing as depicted in figure 3.5 is used, the inductance will be modified to

$$L_H \approx L \times \left[1 - \left(\frac{D_1}{D_2}\right)^3\right] \times \left[1 - \left(\frac{l_1}{2l_2}\right)^2\right], \tag{3.10}$$

where D_2 and l_2 are geometrical parameters of the housing (Fig. 3.5). There are two empirical golden ratios for equation 3.10, $l_1 = 0.55D_2$ and $l_1/2l_2 = 0.377$, resulting in the minimal decrease of the coil's inductance L. Limitation of space demands a multi-layer coil and in such instances the inductance is calculated as

$$L \approx \frac{0.2\,(D_1^2 \times N^2)}{3D_1 + 9l_1 + 10D_w}. \tag{3.11}$$

As before, the same unit considerations are valid and D_w is the thickness of the windings on top of each other (number of layers times thickness of the wire). One can estimate the Q-factor of such a resonator as $Q \approx 50D_2\sqrt{\nu_0}$, but as mentioned before this estimation is practically difficult to be realized in the experiment's environment.

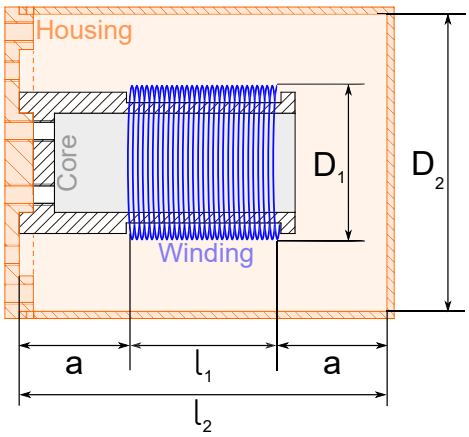

Figure 3.5: The CAD-drawing cross-section of a helical resonator typically used in experiments such as ARTEMIS. The orange color indicates the housing.

The capacitance of a single-layer air-core resonator can be estimated for the turn-to-turn

C_{TT} and coil-housing C_{TH} contributions as

$$C_{\mathrm{TT}} \approx \frac{\pi^2 D_1 \epsilon_0}{ln\left(p/2r + \sqrt{(p/2r)^2 - 1}\right)}, \qquad C_{\mathrm{TH}} \approx \frac{2\pi^2 D_1 \epsilon_0}{ln\left(h/r + \sqrt{(h/r)^2 - 1}\right)}. \tag{3.12}$$

where ϵ_0 is the vacuum dielectric constant, r the wire thickness, p the distance of two adjacent wires and h the distance of the wire from the housing (fortunately all lengths are in m). The result of capacitance calculations in such a system is typically orders of pF, describing how sensitive a resonator is regarding its capacitance changes imposed by the environment or additional components (such as wires or feed-throughs).

3.2.3 Toroidal Resonator

A toroidal structure has the advantage of containing the magnetic field flux within itself in comparison to a helical coil. This translates to minimizing the eddy-current losses in the housing and results in an increase of the Q-factor. Hence, it reduces the effect of the housing on the final performance of the resonator. The resonance frequency obeys the same formula as in the helical case (equation 3.8).

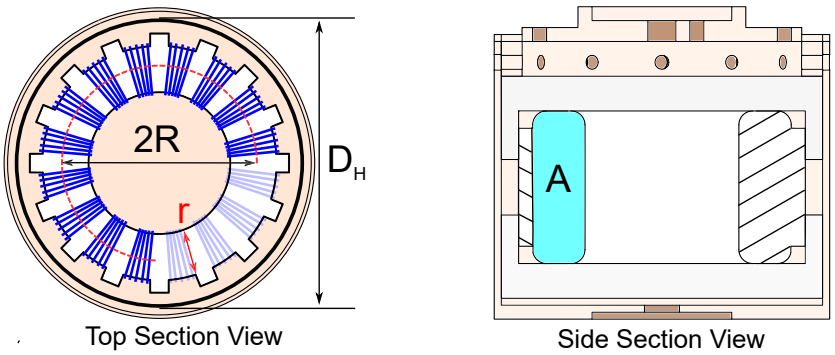

Figure 3.6: The schematic drawing of a toroidal resonator typically used in experiments such as ARTEMIS. The orange color indicates the housing.

The inductance of a single-layer toroidal inductor can be estimated as

$$L \approx \mu \frac{N^2 A}{2\pi R}, \tag{3.13}$$

with N being the number of winding turns, A the cross-sectional area of the PTFE core, μ the permittivity of the core of the coil and R the major radius of the toroid (Fig. 3.6). Based on [71] the inductance L_T of a toroidal coil with rectangular cross section can be approximated by

$$L_T \approx \kappa N^2 a \ln \frac{d_2}{d_1}, \tag{3.14}$$

where κ =$0.46 \times 10^{-6}\,\mathrm{H\,m^{-1}}$ is the geometry-specific factor, d_1, d_2 and a are the inner and outer diameters and the thickness of the toroid, respectively. In many cases the coils include a multilayer winding, which should modify the obtained values considerably. A further consideration for resonators with higher resonance frequency is the dielectric constant of the core, therefore the best cost-effective low-loss dielectric, PTFE, has been used as the core of the winding [71].

Calculation of the self-capacitance of a toroidal coil is a non-trivial procedure that includes many estimations and steps, as described for example in [73]. Even after this much consideration the resulting value is not matching accurately enough to be applicable. Anyhow using reference [73] one can estimate the value as

$$C_T \approx \chi\epsilon_0 l \left(\frac{\epsilon_r \theta}{\ln\frac{d_w}{d_2}} + \cot\frac{\theta}{2} - 1 \right). \tag{3.15}$$

Here $l \approx (d_2 - d_1) + 2a$ is the average single-turn conductor length and

$$\theta = \arccos(1 - \epsilon_r^{-1}\ln(d_w/d2)), \tag{3.16}$$

accounts for the effective diameter of the core including the winding, ϵ_r is the relative permittivity of the insulator and χ is again a geometry factor [73].

3.2.4 Inductor Tapping

While coupling the pick-up signal from the resonator to the cryogenic amplifier, it is essential to decouple any external noises from the stored ions in the trap; thus a capacitive, an inductive pick-up scheme, or a combination of both is commonly used for this purpose. In the current setup, inductive coupling has been used to input the signal from the resonator into the cryo-amplifier, which at its input has a capacitive coupling built in (Section 3.5).

The inductive coupling is normally established via a separate secondary coil or by a wire which is soldered to the inductor coil at a point based on the calculations. The latter technique is the method of choice at ARTEMIS, which is known as tapping and basically creates an

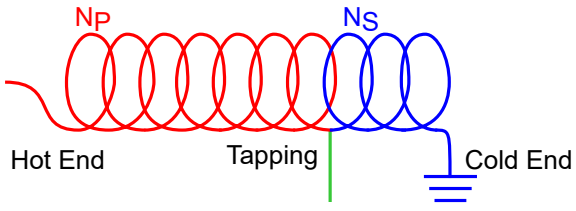

Figure 3.7: Tapping signal coupling of a resonator, Creating a typical auto-transformer. Primary coil illustrated in red and secondary in blue.

auto-transformer [72]. The coil with higher number of windings N_P —the primary coil—is connected to the trap's electrode from the side referred to as hot end, whereas the fraction with lower number of winding N_S —the secondary coil—is grounded from one side named the 'cold end'. The tapping wire is connected to the amplifier (Figure 3.7).

Similar to any other transformer configuration, the transformer-turn ratio, relates to the voltages across each of the two coils as

$$\frac{V_P}{V_S} = \frac{N_P}{N_S}; \tag{3.17}$$

here V_P and V_S are the voltages across the primary and secondary coil, respectively. An important consideration is that by tapping the coil, the self-capacitance and the inductance of the coil will change. Nonetheless, applying the tapping coupling is a common technique and a winding ratio of 70% primary to 30% secondary has been widely used [67, 66, 20].

3.2.5 Resonators at ARTEMIS

At ARTEMIS the initial (and current) setup design includes three RLC detection systems. One axial resonator at the creation trap (CT), known as the ARES CT. Two detection circuits at the spectroscopy trap (ST), first the axial detection system —ARES ST—and second the cyclotron detection system, CRES. The resonators are typically studied in two different scenarios:

- Unloaded: In the absence of the trap and other parts of the detections system. The measured quality factor is a characteristic of the inductor itself.

- Loaded: Including the trap and the rest of the RLC detection system. The trap normally adds an external resistor load to the inductor's resistance, resulting in change of quality factor. In addition, the capacitance of the trap C_T leads to a shift in the resonance frequency.

Normally, a resonator with high quality factor is desirable when dealing with single confined particles or ion clouds with small number of particles and a highly tuned trap. However, since ARTEMIS is designed to operate with ion clouds with high number of ions and considerable frequency widths of the ion signal, the application of really high Q-values (e.g. $Q = 100000$) is not as straightforward as in the case of single charged particle. For detection, a very high Q-value can generally be beneficial, whereas for cooling, it is only helpful under certain conditions (really fast equilibration of an ion ensemble).

3.2.6 Superconducting Helical Axial Resonator

Since the beginning of the ARTEMIS setup development, the ARES CT has not changed —a helical structure with 300 windings of NbTi superconducting wire in a gold-plated copper cylindrical housing (designed and made by M.Shaaban, reference [20]). Figure 3.8 shows the loaded spectral response of the ARES CT after excitation with tracking generator of the KEYSIGHT spectrum analyzer with $-120\,\mathrm{dBm}$ (including $-70\,\mathrm{dBm}$ attenuators in the excitation line) at liquid helium temperature and a magnetic field strength of $7\,\mathrm{T}$. From this spectrum a resonance frequency of $\nu_0 \approx 741\,\mathrm{kHz}$ and a quality factor of $Q \approx 1000$ can be derived.

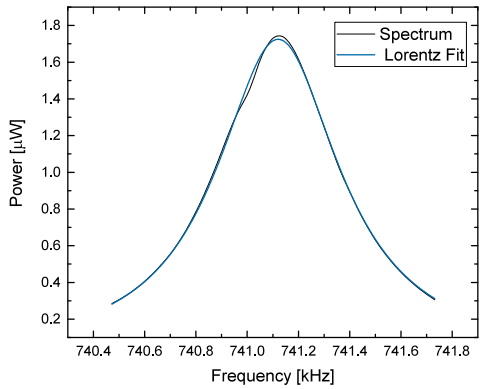

Figure 3.8: The spectral response of the ARES CT after excitation with tracking generator of the KEYSIGHT spectrum analyzer, loaded and at a temperature approximately equal to $4\,\mathrm{K}$.

The resonators at the ST, on the contrary, have been changed several times in comparison to the 2015 measurement campaign. Figure 3.9 shows the arrangement of these resonators in two consecutive years, 2016 and 2017.

3.2.7 Superconducting Toroidal Axial Resonator

The axial resonator used in the 2016 measurement campaign has been developed by the author of this thesis according to the design of the BASE collaboration [75], during his visit to CERN in the beginning of 2016. Also this resonator has been later used to study the effect of a variable magnetic field on a superconducting resonator [76]. This resonator is made out of a niobium-titanium (NbTi) wire with a diameter of $0.075\,\mathrm{mm}$ and a perfluoroalkoxy (PFA) insulation. The coil has toroidal geometry. It is wound on a PTFE core with a rectangular cross-section, that has an inner diameter of $23\,\mathrm{mm}$ and an outer one of $38\,\mathrm{mm}$ and a toroid thickness of $22\,\mathrm{mm}$ (figure 3.6). The toroid is divided into 16 sections, where in each section three layers of 15 to 20 windings are positioned tightly, resulting in roughly 800 rounds of winding (including the connections between sections), this results in a NbTi wire length of about $48\,\mathrm{m}$. For optimal thermalisation and fixation of the NbTi wire in the sections, it is

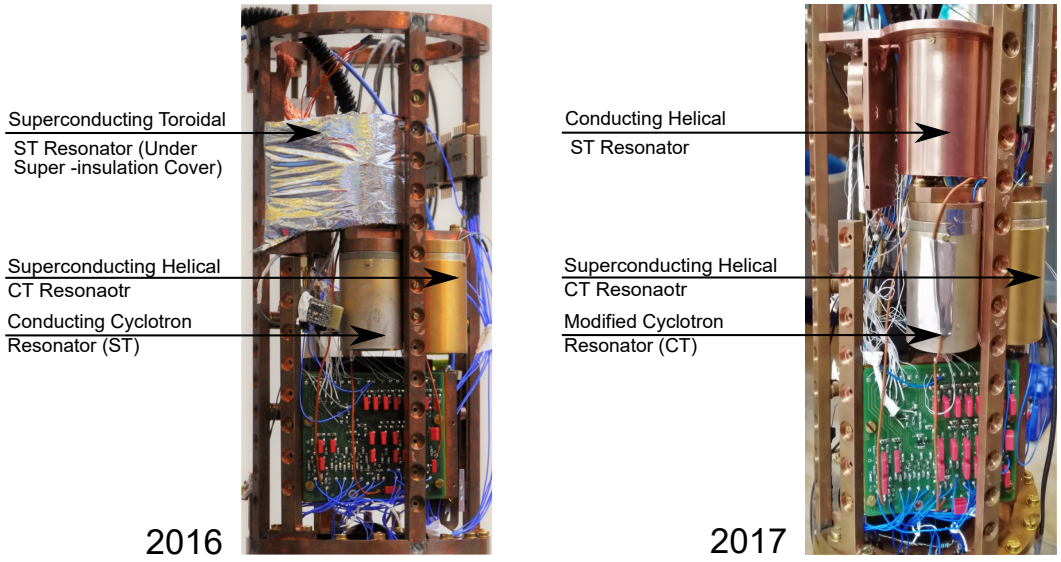

Figure 3.9: The RLC detection system at ARTEMIS comparing the arrangement of resonators in two consecutive years. On the left hand side the superconducting toroidal resonator is highlighted while it is wrapped in super insulation foil [74].

required to have each layer of the wire wrapped with layers of PTFE tape tightly. According to equation 3.14 the inductance of this coil is $L_T \approx 3\,\mathrm{mH}$. Due to the consideration made regarding the housing, this value is estimated [2] to be reduced to $L_T \approx 2.4\,\mathrm{mH}$. The self-capacitance C_T of this coil can be approximated by equation 3.15, considering $d_W \approx 42\,\mathrm{mm}$, $\epsilon_0 \approx 8.85\,\mathrm{F\,m^{-1}}$,$\epsilon_r \approx 2.1$ and $\chi \approx 1.366$ which results in a value of $C_T \approx 8\,\mathrm{pF}$. Also considering that the parasitic capacitance of the housing this value is modified to $C_T \approx 10\,\mathrm{pF}$ and using equation 3.8 the resonance frequency is approximately equal to $2\pi \times 1\mathrm{MHz}$.

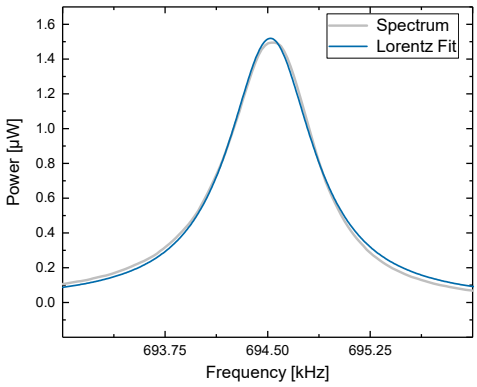

Figure 3.10: The spectrum of the superconducting toroidal axial ST resonator at 4 K and 7 T with tracking generator excitation.

The unloaded quality factor of this resonator has been measured to be approximately $Q \approx 21000$ at 4 K using a Keysight E5061B ENA Vector Network Analyzer (matching the value obtained from the Rigol DSA-815TG spectrum analyzer with tracking generator [76]). Figure 3.10 shows a loaded excited spectrum of this resonator paired with its amplifier at a tem-

[2] this value is estimated using equation 3.10 and it is named L_T to indicate that the resonator under discussion is in fact a toroidal one.

perature of approximately $4\,\mathrm{K}$ and at $7\,\mathrm{T}$. From this spectrum a quality factor $Q \approx 950$ at a resonance frequency of $\nu_0 = 694.520\,\mathrm{kHz}$ is calculated.

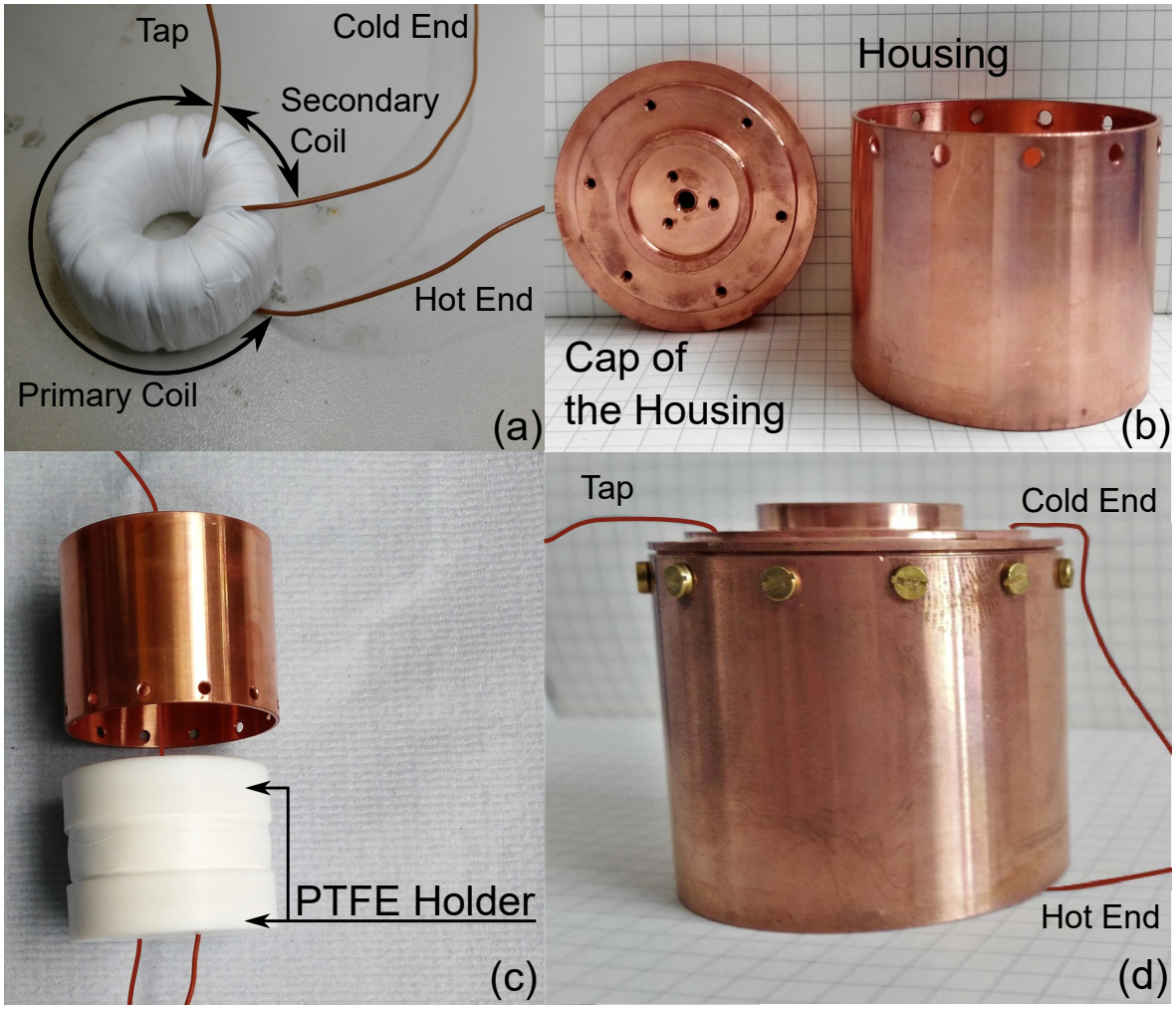

Figure 3.11: Four different stages of a superconducting resonator production. From winding the toroidal coil (a), to the final assembly(d). Sub-figure (b) shows a polished housing and sub-figure (c) depicts the internal assembly of the resonator.

Figure 3.11 shows four different stages of a toroidal resonator production. In each sub-figure there are some points that have been considered while constructing this resonator, which they are as follows:

(a) To ensure the that all superconducting wires are kept in place firmly, each layer of the winding is tightly wrapped with a PTFE tap. Superconducting wires must be uniformly thermalised, otherwise the different sections with unequal temperatures will have different impedances resulting in a decrease of the quality factor and shift in resonance frequency. Also, it should be pointed out that this resonator has approximately a 3:1 ratio between the primary and secondary coil.

(b) The resonator housing has been designed for optimal heat conduction to keep the coil at

liquid helium temperature and also it has been carefully cleaned and polished to remove any contamination.

(c) The PTFE holders are designed to keep the toroidal resonator fastened in its position to make it robust against physical changes plus good thermal contact.

(d) A high number of brass screws (with higher thermal contraction in comparison to OFHC copper) are used for fixing the cap and housing together to ensure good thermal connection and stability.

(e) Special care was taken while connecting a NbTi wire to the copper wires, since the soldering joint between the superconducting and normal-conducting wires affects the total amount of effective resistance of the coil [77]. If the joint is not well-made, a shift of the resonance frequency, a severe decrease of quality factor and total loss of signal can happen [21]. There are several publications concerning proper soldering of the superconducting joints [78, 79].

As a practical point, the superconducting resonator should be covered with superinsulation (e.g. 'Coolcat 2' foil from RUAG), to isolate the resonator form radiative heat transfer of components with higher temperature. In this manner the chances of not reaching temperatures below the superconducting transition temperature T_C are minimized. The results regarding behavioral studies of this resonator in an unloaded case in a magnetic field up to $6\,\mathrm{T}$ can be seen in section 3.3.

3.2.8 Normal-conducting Axial Resonator

Although the high quality factor of a superconducting resonator is a convincing reason to prefer them to the normal-conducting resonators, the lack of required infrastructure to produce, test and maintain a superconducting resonator has motivated its replacement with a normal-conducting resonator at the 2017 measurement campaign. Since a normal conducting resonator can be manufactured, characterized and tested without any cryo-cooling requirement. To this end, based on the helical design of section 3.2.2 (with $D_1 = 35\,\mathrm{mm}$ and $l_1 = 20\,\mathrm{mm}$) and using a normal conducting copper wire with a diameter of $0.13\,\mathrm{mm}$, a new axial resonator with 270 windings as the ARES ST was constructed and mounted in ARTEMIS. Using this resonator, a faulty soldering junction (that had formerly caused a decrease and eventually loss of the signal with the superconducting resonator) at the feed-through of the trap chamber was detected and fixed. Figure 3.12 shows the winding, final internal structure and mounting location of this resonator from left to right, respectively.

Figure 3.13 depicts a comparison between the spectral responses of the newly-made non-superconducting ARES CT at room temperature without any extra capacitive load from the

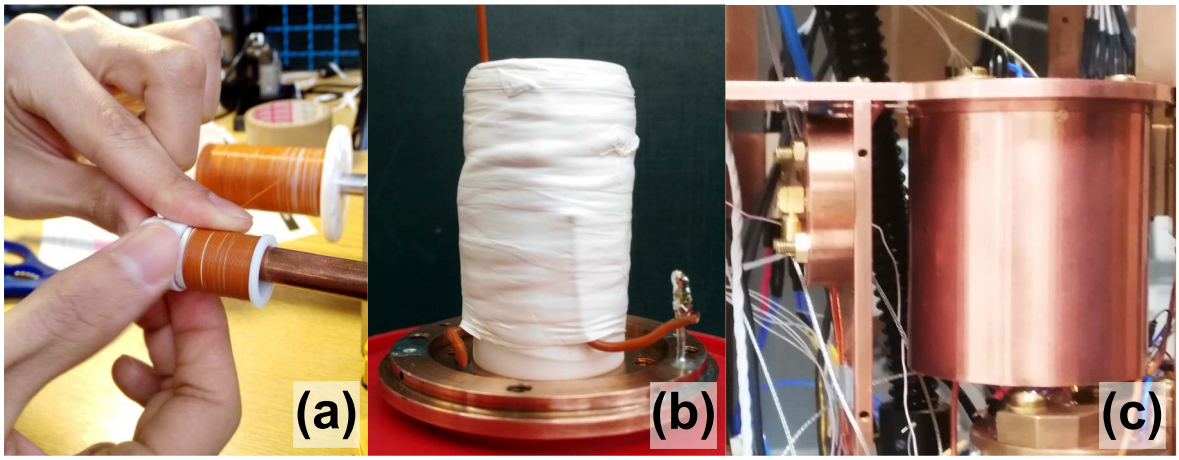

Figure 3.12: The construction of the new helical non-superconducting axial ST resonator.

trap and the rest of the detection system (left side), and the loaded resonator at $4.2\,\mathrm{K}$ mounted at the electronic section of ARTEMIS (section 4.2.3). This measurement is performed using the tracking generator of the KEYSIGHT with an excitation power of $-120\,\mathrm{dBm}$ (including attenuators in the excitation circuit). When unloaded this resonator has a quality factor of approximately 100 and an unloaded resonance frequency $\nu_0 \approx 1.23\,\mathrm{MHz}$, while in the loaded case demonstrated a $\nu_0 \approx 940.7\,\mathrm{kHz}$ and $Q \approx 87$.

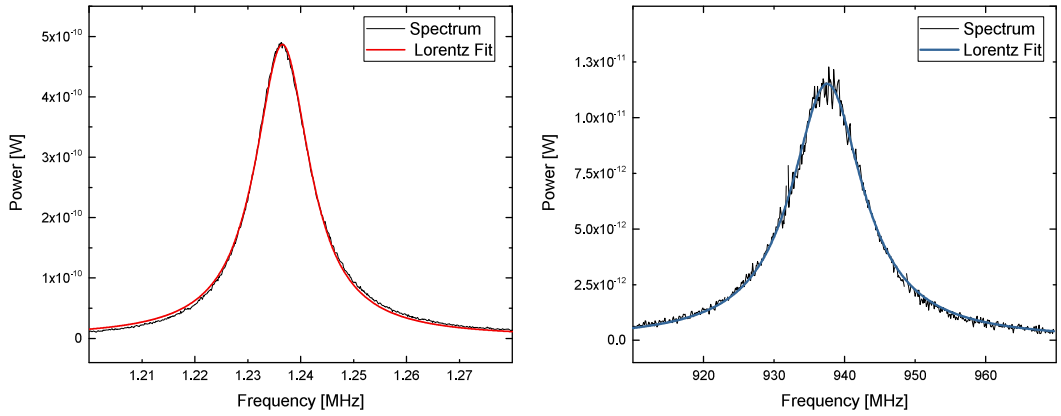

Figure 3.13: The spectral response of the new non-superconducting resonator, unloaded at room temperature verses the loaded at $4\,\mathrm{K}$.

3.2.9 Modification of the Cyclotron Resonator

The current cyclotron resonator at ARTEMIS is a modified version of the one designed and built by M. Hüllen [80]. This resonator has a helical design and is built on a PTFE core using $1.5\,\mathrm{mm}$ thick copper cable. Originally, the resonance frequency of about $2\pi\times35\,\mathrm{MHz}$ and quality factor of around 140 has been reported for the resonator in [20].

Nevertheless, it has been shown previously (section 3.2.1), that the resonator's capacitance is sensitive to any parasitic capacitance load from the setup, which consequently changes

the resonance frequency. Hence, applying a varactor diode board (section 3.4) is presently required for the cyclotron resonator. It enables one to match the resonators frequency of the CRES to the value of the reduced cyclotron frequency of the trapped charged particles.

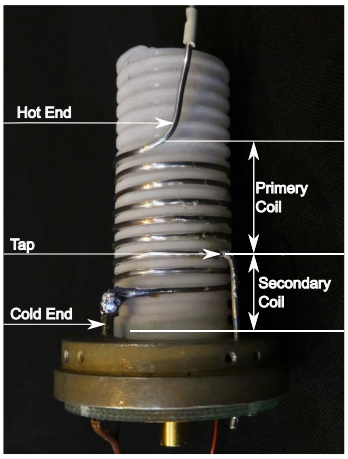

Figure 3.14: The structure of the new cyclotron resonator with 7.5 rounds of winding on a PTFE core. The modification was performed to match the frequency of the CRES to utilize a varactor diode board. Showing the primary and secondary ratio and the connection.

Using the same OFHC gold-plated housing and PTFE core, reducing the number of winding rounds from ten windings to seven-and-a-half rounds and $1/3$ secondary-to-primary ratio the required modification was done. As a result, its unloaded resonance frequency when coupled to a circular shape amplifier (section 3.5) at room temperature was measured to be $\nu_0 \approx 110.422\,\mathrm{MHz}$ with $Q \approx 85$ (figure 3.15). Later on when coupled to the rest of the detection system and at $4\,\mathrm{K}$, the resonance frequency was modified to approximately $33\,\mathrm{MHz}$, in a manner that the final resonance frequency with the help of a varactor diode board could be adjusted to $35\,\mathrm{MHz}$. The full results of these efforts are presented in section 3.4, but for comprehension of this section, figure 3.15.b shows the loaded CRES at $4\,\mathrm{K}$ and located at ARTEMIS. The quality factor of $Q \approx 135$ at $\nu_0 \approx 34.940\,\mathrm{MHz}$ can be calculated from the spectrum.

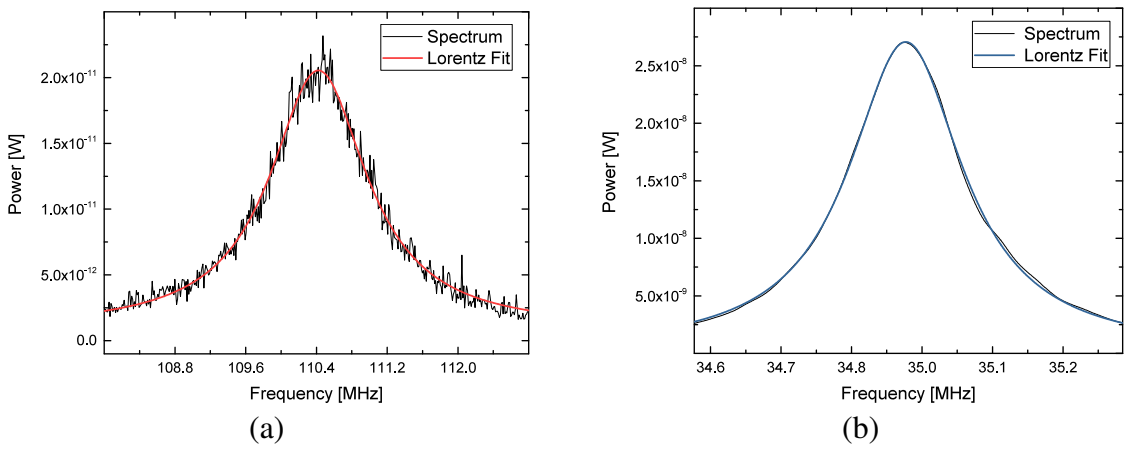

Figure 3.15: Spectral response of the CRES unloaded(a) and loaded(b), at room temperature and $4\,\mathrm{K}$, respectively. These spectra were acquired with a spectrum analyzer and using its tracking generator excitation.

In conclusion, currently there are three detection systems at ARTEMIS available, with the following specification:

- Axial CT (ARES CT): $\nu_0 \approx 741\,\mathrm{kHz}$, $Q \approx 1000$
- Axial ST (ARES ST): $\nu_0 \approx 940\,\mathrm{kHz}$, $Q \approx 90$
- Cyclotron ST (CRES): $\nu_0 \approx 33$ to $36.5\,\mathrm{MHz}$, $Q \approx 135$.

Due to the high level of back ground noise present at the actual experimental environment of ARTEMIS, the two non-superconducting resonators have not been producing ion signal data, drawing the conclusion that further developments are required for successful measurements.

Considering the typical mass spectra obtained at the CT of ARTEMIS (Section 6.1), for typical ion numbers Ar^{13+} at ARTEMIS spectral-width of approximately $10\,\mathrm{kHz}$ is expected —after subsequent sufficient cooling. Thus, for the desired resonance frequency of the Ar^{13+} at the CT —about $737\,\mathrm{kHz}$ —a quality factor of better than 70, results in ion signal-width broader than the spectrum width of the resonator. Nevertheless, such quality factors are not suitable considering the attempts made with the normal-conducting resonator in 2017 measurement campaign. In addition, this value might have undesired effect on the resistive cooling of the ion ensemble (5.2.3)

3.3 Superconducting Resonators

An established method of accomplishing a high-quality-factor resonator is using type-II superconducting wires for winding the inductor, since operating these resonators below the superconducting critical temperature T_C suppresses the ohmic losses. However, the superconducting resonators are only superior up to a certain frequency of about $100\,\mathrm{MHz}$ and after this limit due to the strong current-vortex interaction the losses become dominant [81]. Due to the typically high magnetic fields in Penning trap experiment environments (Section 4.2.1), it is preferable to use a type-II superconducting material, such as pure niobium (Nb), niobium-titanium (NbTi) or niobium-tin (Nb_3Sn). In type-I superconducting materials (e.g. vanadium, tantalum or lead) below the critical magnetic field strength B_C, the material is in so-called Meissner phase; totally excluding an external magnetic field and maintaining superconductivity. In contrast to the sharp transition of type-I superconductors, a type-II superconductor in magnetic field undergoes a gradual flux penetration. The phase diagram of type-II superconductor is schematically demonstrated in figure 3.16; for field strengths below the first critical magnetic field strength B_{C1} the Meissner phase is maintained. For values of B between the B_{C1} and the second critical magnetic field strength B_{C2} the so-called Shubnikov

Phase is established, which is the gradual magnetic field flux penetration in the superconductor. Subsequently, the phase transition from superconducting to normal state happens at the B_{C2}.

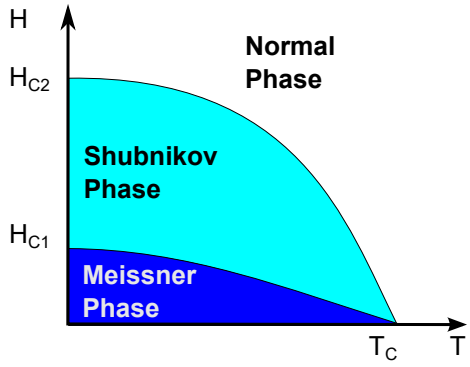

Figure 3.16: Schematic depiction of three different phases of a type-II superconductor.

In the Shubnikov phase the magnetic field penetrates the superconducting material as quanta of the magnetic flux $\Phi_0 = hc/(2e) \approx 2.067 \times 10^{-15}\,\mathrm{T\,m^2}$ across the bulk of the superconducting material, resulting in vortices in the superconductor. A vortex can be described as a circular super-current around a normal-conducting core parallel to the magnetic field lines [81]. The Shubnikov phase, is typically where the resonator wires are stated at typical magnetic field strengths of Penning trap experiments. The values of the T_C, B_{C1} and B_{C2} have an important role in choosing the material of the wire used to build a superconducting resonator. Based on [81, 82, 83, 84] these values for some of the popular superconductors are listed in table 3.1. The type-II NbTi superconductor is normally used as a prominent choice in many experiments, such as ARTEMIS and the BASE collaboration [23] . It should be considered

Table 3.1: Some common type-I (the first three listed rows) and type-II superconductors (the second listed rows) and their $B_{C1}(T=0)$, $B_{C2}(T=0)$, $T_C(B=0)$ values.

Superconductor	$B_{C1}(T=0)$	$B_{C2}(T=0)$	$T_C(B=0)$
Pb	81 mT		7.2 K
V	102 mT		5.3 K
Ta	83 mT		4.5 K
NbTi	22 mT	14.5 T	9.3 K
Nb_3Sn	19 mT	24.5 T	18 K
Nb	180 mT	410 mT	9.25 K

that the values presented in table 3.1 for the B_{C1} and B_{C2} are at absolute zero temperature,

which in reality these field strengths scale with temperature as [81]

$$B_{C1}(T) \approx B_{C1}(0)\left(1-\left(\frac{T}{T_C}\right)^2\right) \tag{3.18}$$

$$B_{C2}(T) \approx B_{C2}(0)\left(1-\left(\frac{T}{T_C}\right)^2\right)\left(1+\left(\frac{T}{T_C}\right)^2\right)^{-1}, \tag{3.19}$$

and the T_C for superconductors within a magnetic field reads as

$$T_C(B_0) \approx T_C(0)\sqrt{1-\left(\frac{B_0}{B_C}\right)}. \tag{3.20}$$

The interaction of the vortices and an AC-current in a type-II superconductor, e.g. radio-frequency signal, gives rise to considerable loss channel. In the simplest picture[3], this loss can be formulated as an effective resistance, leading to a non-zero energy loss per oscillation [81]. However, since the rf signal of the trapped ions are at maximum in the order of a few tens of MHz, this losses which scale with the third power of the frequency are not an obstacle to utilize type-II superconductor resonators. In addition, the local inhomogeneities in the lattice structure create an energetic favorable site for localization of the vortices reducing the effect of the losses. This phenomenon is know as pinning [87].

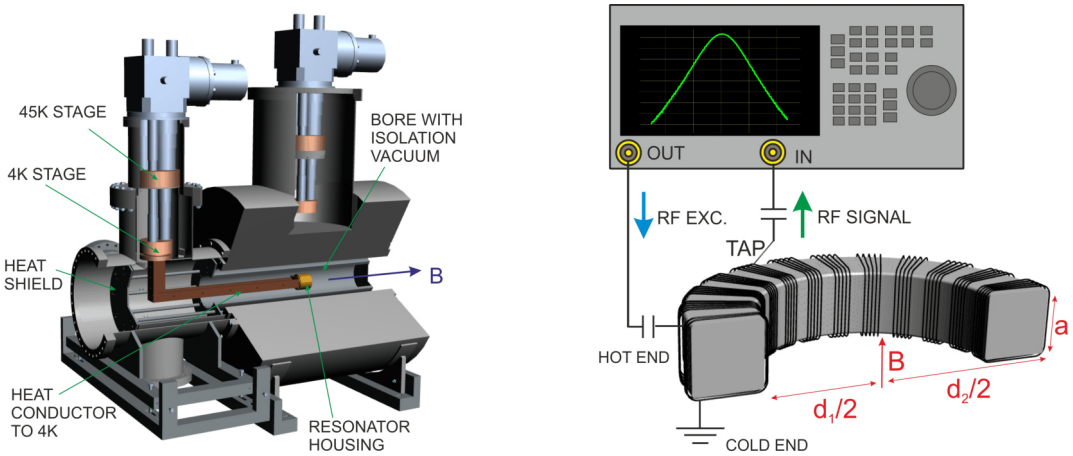

Figure 3.17: The setup used for studies on the behavior of a superconductor resonator in magnetic field. On the left side the magnet of HILITE and the mounting system is depicted and on the right hand the rf circuit for such a measurement is shown.

Inspired by studies performed by [88], in order to have better understanding of the behavior of the superconducting resonators, studies on an superconducting toroidal resonator described in 3.2.5 have been performed. The result of these studies have already be reported in [76] and with minor considerations can be applied to a vast range of type-II superconducting detection

[3]For more detailed explanation please see [85], [86] and [87].

systems.

The resonator has been placed in the center of the homogeneous magnetic field of the superconducting magnet of the HILITE experiment [89](figure 3.17.left). This magnet has continues variable field strength in the range of 0 to $6\,\mathrm{T}$. The axis of of the toroidal coil was aligned with the axis of the magnetic field. Using a pulse-tube cryo-cooler system (similar to the system in section 4.2.3), the resonator is cooled down to $4\,\mathrm{K}$, well below the T_C of NbTi.

Figure 3.17.right depicts the rf signal setup used in this measurement; the resonator is excited capacitively by placing the excitation line in vicinity of the 'hot end' and using the tracking generator of RIGOL DSA-815TG spectrum analyzer. The response spectrum is measured capacitively via a feed-through from the tap of the resonator.

3.3.1 Superconducting Resonator Behavior in Magnetic Fields

In these measurements the resonator was first cooled down below the T_C. Afterwards, the magnetic field strength was swept between 0 to $6\,\mathrm{T}$ with step size of $10\,\mathrm{mT}$. This sequence of cooling and magnetic field application is known as zero-field cooling, which might have slightly different results in comparison to a when the opposite order—field cooling—is performed. The vortices enter and distribute differently in the superconductor for this two different processes [81, 82], nevertheless further studies are required to clarify this differences.

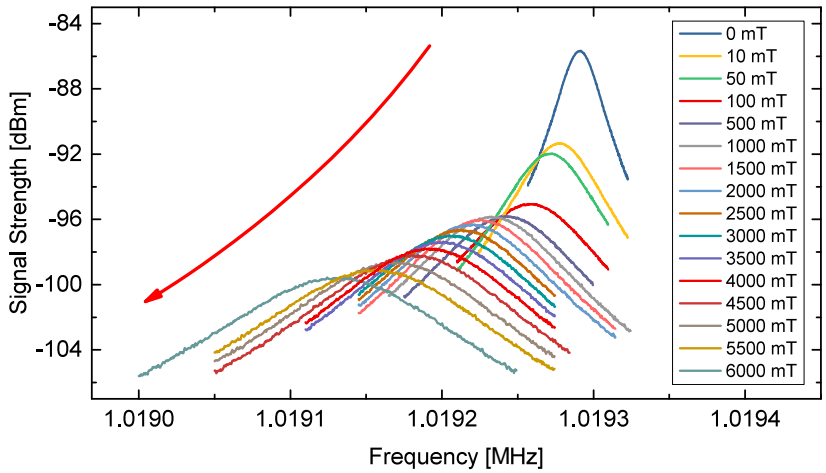

Figure 3.18: A selected set of sixteen spectral responses of the resonator at different magnetic fields strengths. The red arrow marks the direction of magnetic field increase.

A selection of sixteen spectra acquired at different magnificent field strengths of the obtained spectral responses of the resonator circuit is plotted versus the their corresponding resonance frequency in figure 3.18. Here the red arrow indicates the direction of increase of the magnetic field B towards $6\,\mathrm{T}$. A considerable shift in the resonance frequency to lower values, an increase of the signal width, and a decrease magnitude is apparent. Those changes

in the spectra also clearly indicate a decrease in quality factor.

For further investigation, the evolution of the resonance frequency and the Q-factor of the spectra were extracted and plot as a function of magnetic field strength (Figures 3.19 and 3.20). As illustrated in the figures 3.19, a monotonic decrease of the resonance frequency is obvious with the increase of the magnetic field strength, specially for lower values of the magnetic filed strength. Most noticeably, an initial sharp decrease happens from the field-free case to a field strength of $10\,\mathrm{mT}$ and the rate of the changes became relatively smaller at around $120\,\mathrm{mT}$ (inset of fig. 3.19). An overall frequency decrease of $161\,\mathrm{Hz}$ from the initial resonance frequency ($1\,019\,290\,\mathrm{Hz}$) at field-free environment happens by increasing the magnetic field strength to $6\,\mathrm{T}$.

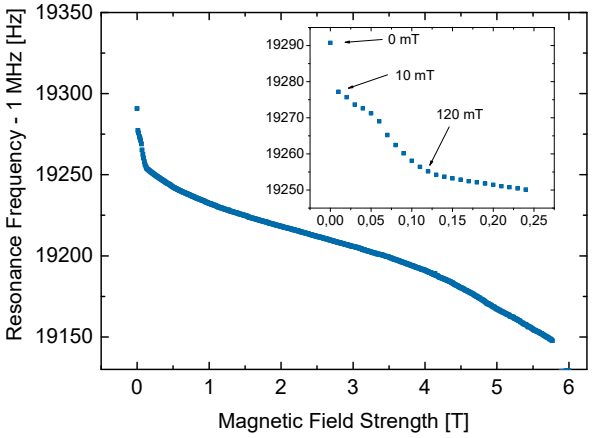

Figure 3.19: The resonance frequency response of the superconducting resonator as a function of magnetic field strength increase from zero up to 6 T.

The broadening of the resonance while increasing the magnetic field translates into a decrease of the quality factor $Q(B)$. Although the finite bandwidth of the spectrum analyzer might have affected the real quality factor of higher values of $Q(B)$, due to this decrease this issue becomes irrelevant rapidly. Figure 3.20 shows this modification as a function of the magnetic field strength. Up to $120\,\mathrm{mT}$ the value of $Q(B)$ decreases by a factor of about 3.5, thereafter the decrease slow down. These changes are much stronger than the ones reported in reference [88] for helical resonator, where a decrease of -15% is reported for the quality factor between zero and $1\,\mathrm{T}$. Therefore, it can be concluded that the overall structure of the resonator used in [88] is more resilient against magnetic field and temperature changes.

The observed frequency shift could be attributed to resistive losses in the superconductor from the interaction of the vortices of the magnetic field with the AC-current at the frequency ω [81]. This energy loss is first observable at the phase transition from the Meissner to the Shubnikov phase. Based on the B_{C1} of NbTi at zero temperature and equation 3.19 the value of the B_{C1} at the temperature of $4.2\,\mathrm{K}$ is estimated to be $18\,\mathrm{mT}$, which seems to be in acceptable range of the acquired data considering this measurements approach.

A convolution of the spatial distribution of vortices $\sigma(r)$ as a function of the magnetic field strength with the spatial current density distribution $j(r)$ is proposed to be the reason behind

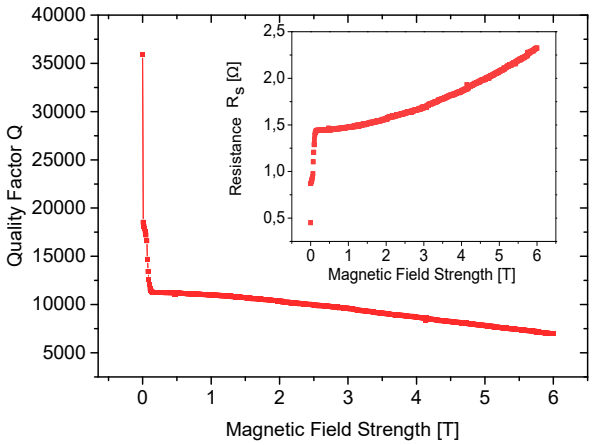

Figure 3.20: The behavior of the quality factor of the superconducting resonator versus the ramping up of the magnetic field strength from zero up to 6 T.

this loss [90, 91]. In other words the resistive loss $\epsilon(r)$ is proportional to $j^2(r)\sigma(r)$. However these two distributions are complicated enough to make the calculation of the loss without further input data of the involved quantities, out of the scope of this measurements.

If we assume that the resonance frequency shift is only generated by the variation of the magnetic field strength, a dampening factor η can be introduced that reads

$$\eta^2(B) = \omega_0^2(B=0) - \omega^2(B). \tag{3.21}$$

This factor can be rewritten as

$$\eta^2(B) = R_s(B)/2L, \tag{3.22}$$

where $R_s(B)$ represents a series ohmic resistance causing the loss. The observation made in the course of this measurement leads to a R_S value of the order of hundreds of ohms. Considering that $Q = \omega_0 L/R_s$, the quality factor has to be about two orders of magnitude lower to match the observed ones. Thus, other mechanisms rather then resistive loss must be responsible for the shift. The inset of 3.20 also confirms this conclusion, since the equivalent R_s from the measured $Q(B)$ is only a few ohms.

A possible explanation for the changes observed in the resonance frequency and quality factor could be a field-dependent increase of the resonator's capacitance and inductance. The value of the capacitance and inductance of resonator are highly dependent on the geometrical parameters (Section 3.2.1), and therefore are viable to changes of temperature due to thermal contractions and expansions. As proposed in [73] a change of the effective coil diameter d_w results in a response of the resonators capacity as follows

$$\frac{\partial C_C}{\partial d_w} = \chi\epsilon_0\epsilon_r l \frac{1}{d_w}\ln^{-2}\left(\frac{d_w}{d_2}\right)\arccos\left(1-\frac{1}{\epsilon_r}\ln\left(\frac{d_w}{d_2}\right)\right). \tag{3.23}$$

For the present resonator configuration it results in spatial derivative of the capacity of about

$11.5\mathrm{pF/mm}$. A relative change of 10^{-4} is equivalent to an effective coil diameter variation in the micrometer scale. Such a small change may well be created by the effect magnetic forces temporal and/or spatial field gradients. As explained earlier in section 3.2.7 efforts to restrict the sensitivity of the winding against external magnetic field influences (specially for high field strengths) have been applied during the construction of this resonator, but apparently they were not sufficient. Hence, for future superconducting resonator developments other methods of minimizing such an effect should be foreseen.

3.3.2 Hysteresis

The magnetic field hysteresis in the quality factor and resonance frequency has been observed for superconducting microwave resonators for smaller values of magnetic field strengths before [90, 92]. A hysteresis is normally created while ramping up the magnetic field from zero to certain values and subsequently ramps down to zero again. Similar studies with an extended range of magnetic field, 0 to $6\,\mathrm{T}$, has been performed on the rf toroidal superconducting ARES. In total five cycles of magnetic field scans have been performed and the results of the first cycle is depicted in figure 3.21.

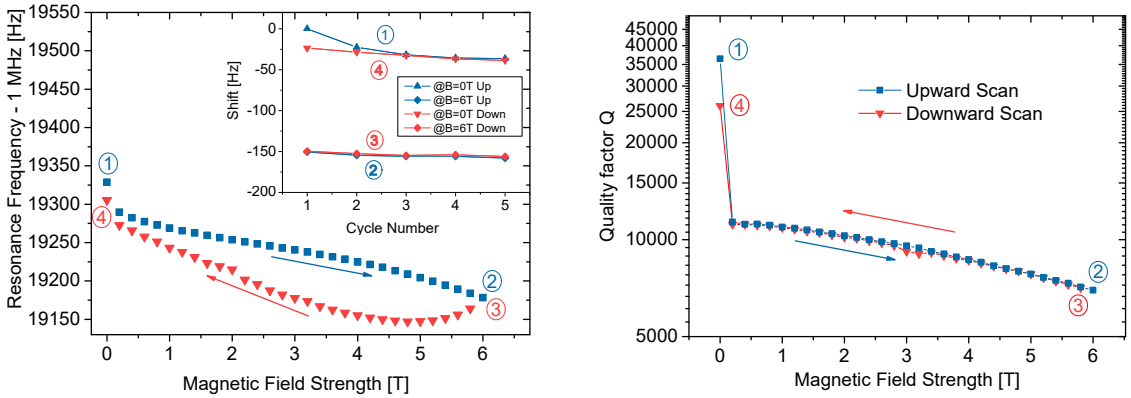

Figure 3.21: Hysteresis studies of rf superconducting ARES for a cycle of ramping up the magnetic field from zero to $6\,\mathrm{T}$ and back down to zero. (a) Shows the pronounced frequency hysteresis observed, with insert showing the behavior of the starting and turning point of magnetic field strength scan. (b) Hysteresis in quality factor.

For the resonance frequency, a clear hysteresis is observed throughout the entire range of the magnetic field scan. As a general trend, the resonance frequency of the upward scan stay clearly above the downwards scan with a relative difference of approximately 10^{-4}. As depicted in figure 3.21.a, the cycle begins in the so-called virgin state at zero magnetic field indicated by (1), the field is scanned up to $6\,\mathrm{T}$ (2), where the down-scan begins (3), and ends at zero field (4). The hysterias effect while changing external field is assumed to be caused by vortex dynamics of the superconductor [71, 93]. With each cycle of the magnetic field scan, the hysteresis effect becomes less clear and as shown in the inset of 3.21.a the frequency of

the four turning points shifts further down as the general trend proposes. The difference of frequency between point (1) and (4) is about -25 Hz, which can be translated to the fact that the superconductor never recovers to its initial vortex-free status without warming up above the superconductivity transition temperature [94].

As figure 3.21.b depicts, the quality factor does not demonstrate a pronounced hysteresis behavior except for the zero-field value, which can be a further evidence for the non-reversible remanent vortices in type-II superconductors. Similar studies on another identical toroidal resonator were carried on later confirming the results presented here, with some exceptions such as the initial resonance frequency of about (1.14 MHz) and quality factor of approximately 22110.

3.4 Varactor-Diode Board

As already introduced in section 3.2, an important part of the non-destructive detection system of ARTEMIS is the varactor diode board. Its fundamental role is to shift the resonance frequency of the detection system by introducing a tunable capacitance in the RLC-circuit as shown in figure 3.4. The centerpiece of this tuning board is a P-N diode with a voltage-dependent capacitance C_V , known as a varactor diode [95]. This diode is commonly used for tuning a LC-circuit's frequency. The capacitance of the detection system can be rewritten as

$$C(U_V) = C_R + C_V(U_V), \tag{3.24}$$

where C_R is the capacitance of the entire detection system without the capacitance of the varactor diode board $C_V(U_V)$. Also it should be considered that due to fact that every varactor diode board has an internal series resistor its quality factor should be considered in calculations (equation 5.20). So the constraints of the varactor diode boards on the overall quality factor should be considered and can be formulated as

$$\frac{1}{Q(U_V)} = \frac{1}{Q_R} + \frac{1}{Q_V(U_V)}, \tag{3.25}$$

with Q_R the quality factor of the rest of the detection system except the quality factor of the varactor diode board $Q_V(U_V)$.

There are two main applications that have been foreseen for the varactor board diode in experiments such as ARTEMIS. Firstly, matching the resonance frequency of the cyclotron resonator with the reduced cyclotron frequency ω_+ of the stored ions. Since according to equation 2.9 the resonance ω_c is dominated by the magnetic filed B, which for most Penning trap experiments is a non-variable parameter. Furthermore, achieving a specific self-

capacitance for the cyclotron resonator is a big challenge as explained in 3.2.5. Secondly, in an experimental environment , e.g. the ESR hall at GSI, isolating the external noise imposed on the resonance circuit is challenging and the resonance circuit does not differentiate between the ion signal and the noise. As a result both of those signals are amplified and sent to the next stages of the detection system. An easy solution would be to tune the resonator to a different frequency and using equation 2.15 by applying a different trapping potential C_2U_0 to bring the stored ion into resonance with the detection system.

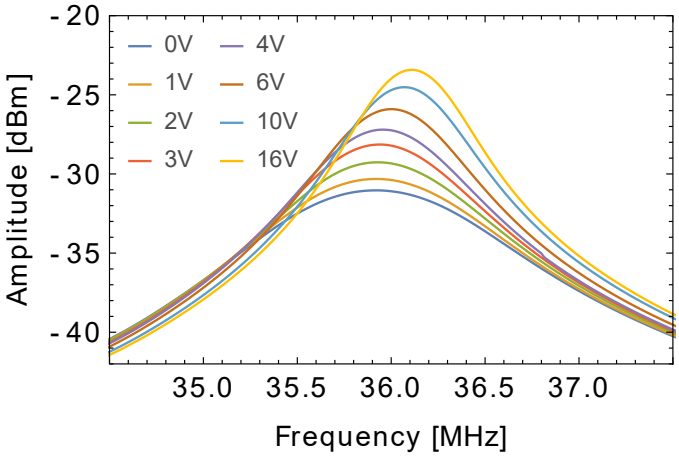

Figure 3.22: A series of excited cyclotron resonance spectra with different biases of the varactor diodes at 4 K and few tesla magnetic field. It is apparent that the varactor diode is not capable of proper functioning, therefore it doesn't shift the frequency more than a 1 MHz.

An attempt to utilize a varactor diode board for tuning the resonance frequency of cyclotron resonator in ARTEMIS was done in the measurement campaign of 2016. A board was built around a MA46H202 varactor diode from Macom, which has a tunable capacitance from 2.2 to 3.3 pF. Although at room temperature and a non-magnetic environment the foreseen resonance frequency of about $\approx 2\pi\times35$ MHz was reached, a combination of high magnetic field and cryogenic temperature resulted in malfunction of the diode, limiting the tuning frequency range to a value less than approximately 1 MHz. Figure 3.22 is taken from PhD thesis of M.Wiesel [21] and demonstrates the limitation in tuning range imposed by the experiments environment. In this figure the cyclotron detection system was excited with the tracking generator of the Rigol DSA-815TG spectrum analyzer through TS-LC channel (section 4.3) and the resonance of the resonators spectral response for eight different diode-biases was read out.

As a result of this observation, in a collaboration with Stahl-Electronics a study to create a functional varactor diode board using the MA46H202 varactor diode suitable for ARTEMIS experiment was conducted. The results of this study can be found in [21], and it indicates the fact that for a varactor diode board to operate properly it is required to either place the varactor diode in regions of the experimental insert where the magnetic field is low or to heat it above 20 K. The first approach is not practical since it means the board has to be placed far from the trap center and it will result in a huge undesired parasitic capacitance load on the detection system. Therefore a heated varactor diode board was produced by Stahl-Electronics and

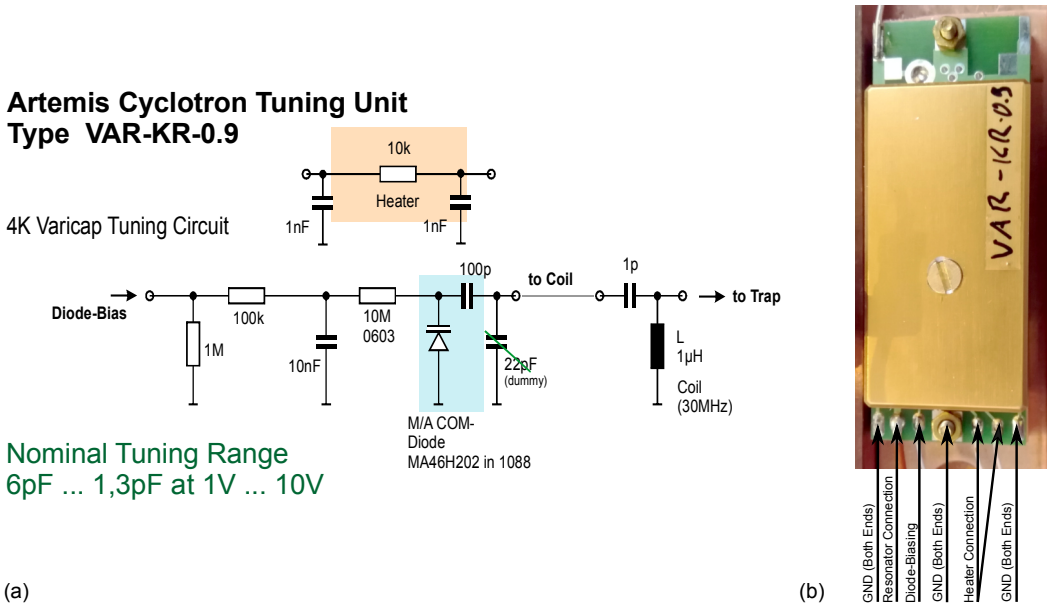

Figure 3.23: The heated varactor diode tuning board at ARTEMIS manufactured in collaboration with STAHL-ELECTRONICS (a) The electronic board layout of the board. (b) Necessary connection required for the board, the screws work as mounting point and ground connections of the board.

installed in ARTEMIS. Figure 3.23.a shows the schematic overview of this tuning board. This board has a nominal tuning range of 1.3 to $6\,\mathrm{pF}$ at a bias voltage of 1 to $10\,\mathrm{V}$ with an expected heating power of $491\,\mu\mathrm{W}$ to rise the diode temperature from 4.2 to $20\,\mathrm{K}$. Figure 3.23.b shows the connection of the tuning board at ARTEMIS. The screw mounts are also working as the ground connections of the board. It is recommended to connect the ground of this board to the rf ground of the inductor coil of the detection system. Further information regarding the technical details of the board are intellectual property of STAHL-ELECTRONICS and can not be reported.

It is required to match the frequency of the cyclotron detection system (3.2.5) to the range that it could be tuned into $35\,\mathrm{MHz}$ with the aid of the varactor diode board. The excited spectral response of the cyclotron detection system was recorded as before. Figure 3.24.a shows the responses of the CRES in a case that the diode is not biased; the blue curve with the heating system of the board off and the red curve after heating it to above $20\,\mathrm{K}$. Afterwards, the diode was biased up to $10\,\mathrm{V}$ in one volt steps and as a result a frequency shift of approximately $3.5\,\mathrm{MHz}$ was measured (ensuring the required frequency flexibility). Figure 3.24.b depicts the Lorentz fits of the spectra corresponding to different voltage biases.

It is also clear that by increasing the bias voltage the quality factor of the resonance spectrum increases. It is a known fact that by increasing the bias voltage of the varactor diodes the quality factor increases as well. Since the quality factor of the diode can be written as $Q_V = 1/(2\pi f R_V C_V)$ [96]. The variation of the resonance frequency (left) and quality factor (right) versus the applied biasing voltage of the varactor diode board (at $7\,\mathrm{T}$, $4\,\mathrm{K}$ and with

the heater set to 2 V) is depicted in figure 3.25.

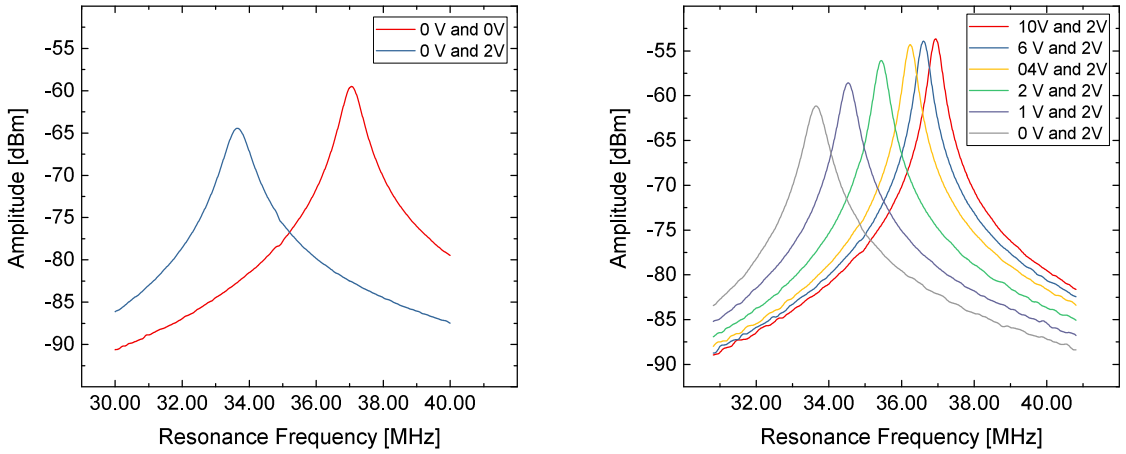

(a) The effect of heating the varactor diode board with 2 V, blue at 4.2 K and read heated above 20 K.

(b) Spectra acquired with different diode bias voltages.

Figure 3.24: The Lorentz fit of the Spectral response of acquired from the cyclotron detection system after implementation of the varactor diode board.

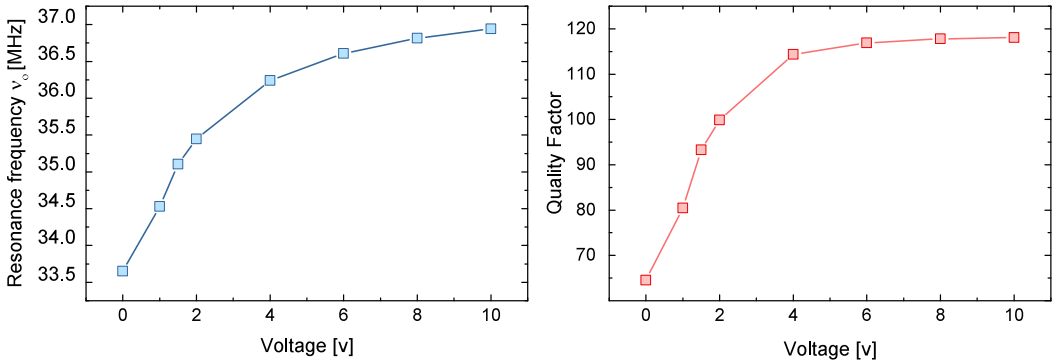

Figure 3.25: The variation of ν_0 (left) and Q (right) of the CRES using a varactor diode at 7 T, 4 K and with the heater set to 2 V).

3.5 Cryogenic Amplifiers

Currently two designs of amplifiers based on the same principle are being commonly used at ARTEMIS. Both of these amplifiers use a variation of metal semiconductor field effect transistor (MES-FET), which is a GaAs semiconductor transistor functional in cryogenic temperatures down to 1 K [97]. One of the amplifiers is designed by M. Hüllen on a circular shaped printed circuit board (PCB) [80], whereas the other amplifier is designed by the BASE collaboration and made by the author during his visit at CERN. After a brief introduction of the MES-FET this two designs will be discussed in this section.

Metal Semiconductor Field Effect Transistor (MES-FET)

MES-FET are GaAs monopolar [4] active devices commonly used as low noise power amplifiers in the microwave and millimeter wave spectrum [69]. It turns out that these devices can also be used for the same purpose in kHz and MHz regime after successfully passing functionality tests in these ranges. Figure 3.26 shows the cross section of a typical n-channel GaAs MES-FET. As depicted, the MES-FET is fabricated on a semi-insulating GaAs substrate. The channel or the conducting layer is a lightly doped thin n-type conducting semiconductor material. On top of the channel a highly doped (n^+) layer is grown so that the ohmic contacts for external circuitry to the transistor is facilitated. Finally, a Schottky barrier (rectifying contact) is fabricated as the gate [98].

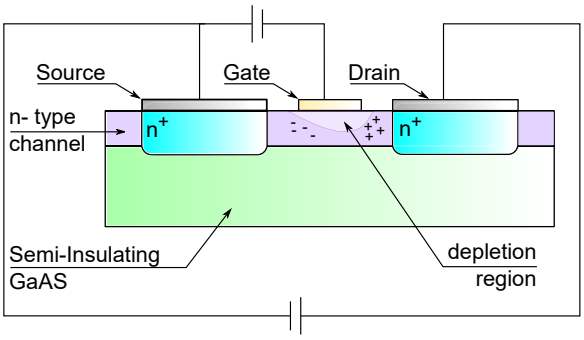

Figure 3.26: Schematic drawing of a basic MES-FET device.

Providing a positive voltage V_{DS} to the drain with respect to the source, creates a flow of electrons from source to drain. The gate acts as rectifying junction by creating a depletion region, which through the width of the region the net opening of the channel is controlled. MES-FET can be considered as a voltage-controlled resistor, where variation of the resistance is achieved by the changes in the depletion layer extension into the channel region. The depth of the depletion region is proportional to the negative voltage applied to the Schottky junction. The source is the reference of the V_{DS} and gate voltage V_{GS} measurements. If $V_{DS} = V_S = 0$ there is no current conduction and the transistor is in so-called equilibrium status. In case the voltage of the gate is above a threshold value V_T the channel current increases with the V_{DS} and eventually saturates to I_{DS} [98]. By applying a positive V_{DS} an electron flow between the source and drain is created. After a signal voltage is applied to the gate, a modulation of the of electron flow with the rf signal happens. This modulation translates to the amplification of the rf signal applied to the gate [69].

Currently, four different types of MES-FET are used to make the amplifiers of ARTEMIS, which there specification according to their data sheets are listed in table 3.2. Please keep in mind that these transistors are vintage and should be treated with high sensitivity. Furthermore, as also indicated in the table, these MES-FETs are specified for applications with higher

[4] With only one carrier type either holes or electrons, n-channel FETs employ electrons and p-channel devices use holes.

Table 3.2: An overview of the four different types of MES-FET transistors used at cryo-amplifiers at ARTEMIS based on their data-sheets. These transistors are currently discontinued, therefore for further information please just search their names in the Internet.

	3SK164	3SK166	CF739	NE3508	unit
Manufacturer	SONY	SONY	Siemens	NEC	
Description	N-channel Dual-Gate	N-channel Dual-Gate	N-channel Dual-Gate	HJ-FET	
Max. V_{DS}	12	8	10	4	V
Max. V_{GS}	$V_{G1S} = -5$ $V_{G1S} = -5$	$V_{G1S} = -6$ $V_{G1S} = -6$	$V_{G1S} = -6$ $V_{G1S} = -6$	-3.0	V
Max. I_{DS}	55	80	80	30	mA
T_{Storage}	-65 ... +150	-65 ... +150	-55 ... +150	-55 ... +150	°C
Max. P_{in}	N.A.	21.7	21.7	0	dBm
Specified Range	0.3 ... 3	0.3 ... 3	0.03 ... 2	0.5 ... 4	GHz

frequency ranges, non-cryogenic and non-magnetic environments (leaving our operation prerequisite condition unspecified 4.2). Hence they can only be used after their compliance with the required condition has been tested on the amplifier board, making the functional transistors even more valuable. These values should be handle cautiously while they are measured and reported for room temperature and the electrical and rf specifications reported are out of consideration for the application in ARTEMIS.

The Amplifiers at ARTEMIS

Both amplifier designs at ARTEMIS follow the same principle and are made of two stages; first stage common-source FET circuit and a second stage source-follower FET circuit. The first stage has a high voltage gain but works at high input impedance. As a result the second stage is built in a way to match the high output impedance of the first stage to the impedance of the rf system (typically $50\,\Omega$). Parasitic reactive loads, resistive loss mechanisms and dielectric losses are three critical loss channels in an amplifier, thus should be avoid to reach a high-quality-factor RLC detection system. The first two can be prevented mostly by circuit-board design and keeping the input resistance of the amplifier high. The dielectric losses at amplifier boards are dominated by the material of the board substrate. The rf quality of a material is defined using the dielectric loss tangent, $\tan(\delta)$. A good option to build a circuit board on are PTFE ($\tan(\delta) = 10^{-4}$) or sapphire ($\tan(\delta) = 10^{-5}$) [69], this level of loss should be considered when dealing with a high Q-factor resonator.

The schematic design (left) and a photo of the ARES CT and CRES cryo-amplifier (from [20]) is demonstrated in 3.27, which as can be seen in the photograph has a circular shape. As it is clear that, it has the same two stage designed structure. The first stage, common-source is built around a SONY 3SK166 and the source-follower stage center piece is the NEC

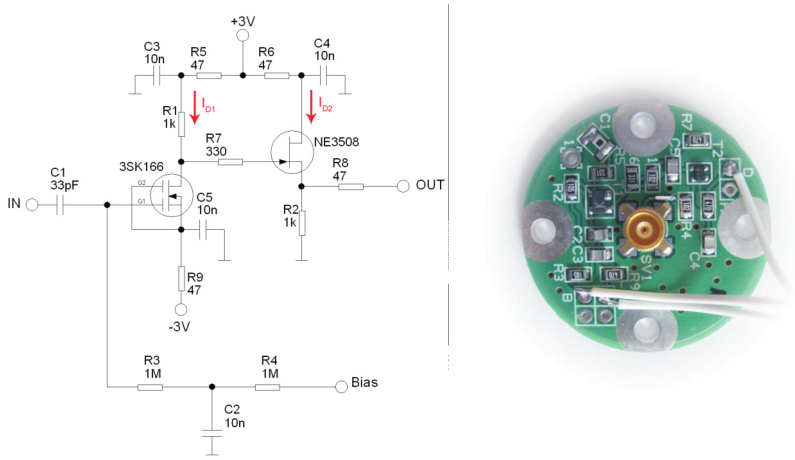

Figure 3.27: Cryo-amplifier used at the CT RLC detection system. Left: Schematic circuit board design Right: photograph of the amplifier board. These figures are taken from the PhD thesis of D. Von Lindenfels [20].

NE350. Further information regarding components, production steps and biasing voltages are available in [20, 21, 80].

The double-stage ST cryo-amplifier is made on a double-sided PTFE laminate board, using again the same architecture. With two different MES-FET, SONY 3SK164 for the common-source stage and the SIEMENS CF739 for the source follower stage. In comparison to the CT amplifier that requires three biasing voltages, this amplifier requires five. Figure 3.28 is a schematic demonstration of the amplifier board including the values of the resistors and capacitors used in this amplifier circuit. The resistors and capacitors used to make this amplifiers are SMD type (surface-mount device) components with a majority of them having 0805 package, except the 1 µF capacitors that are 1206 packages. It is recommended to use components from AVX (NPO type dielectric) or JOHANSON (S-series), since their characteristics in cryogenic environment and high magnetic field are not altered severely.

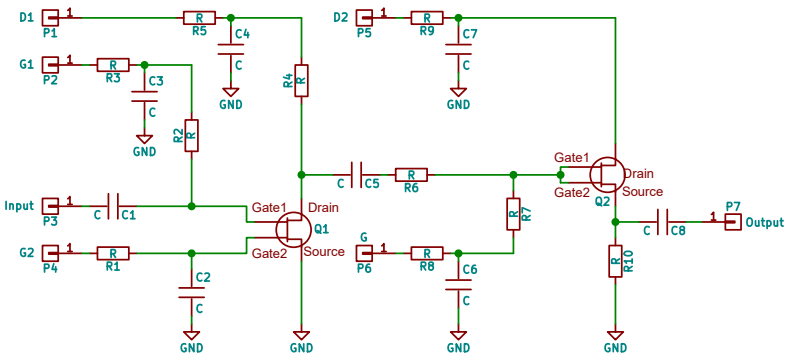

R1 = 10 KΩ	C1 = 2.2 nF
R2 = 100 MΩ	C2 = 1 µF
R3 = 10 KΩ	C3 = 1 µF
R4 = 1 KΩ	C4 = 1 µF
R5 = 100 KΩ	C5 = 2.2 nF
R6 = 250 KΩ	C6 = 1 µF
R7 = 1 MΩ	C7 = 1 µF
R8 = 10 KΩ	C8 = 2.2 nF
R9 = 100 KΩ	Q1 : 3SK164
R10 = 680 KΩ	Q2 : CF739

Figure 3.28: Cryo-amplifier used at ST RLC detection system, made at the BASE collaboration. On the right hand side the values of the components used to make this amplifier board are noted. All the resistor values are denoted by R# and capacitors by C#.

Also as demonstrated on the right side of figure 3.29 the amplifier board is soldered on top of a OFHC copper plate to have a well established ground connection. Finally, a similar plate

in size and shape is mounted on top of the resonator using proper spacers for preventing damages by static electric discharge to the MES-FETs (or mounted in a OFHC copper housing).

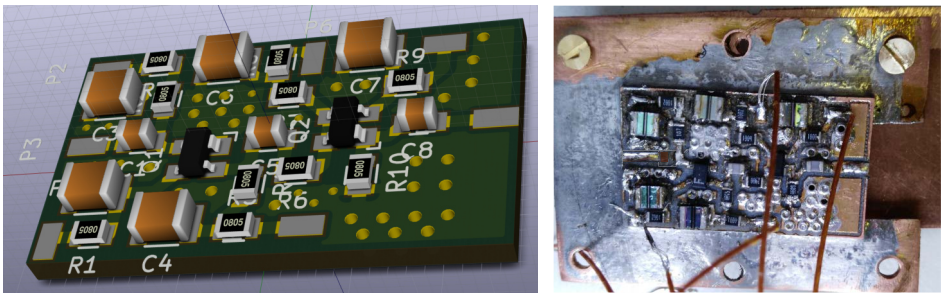

Figure 3.29: Cryo-amplifier used at the CT RLC detection system. left: Schematic circuit board design

Before an amplifier can be paired with a resonator to shape a complete RLC-detection system it is essential to test the performance of the amplifier in cryogenic and magnetic environment. Nevertheless, due to the lack of equipment this test is not put into practice regularly at ARTEMIS currently. The amplifier made for ARES ST made at CERN has been tested in a cryogenic environment as follows. The amplifier is mounted on a $4\,\mathrm{K}$ stage of a pulse-tube cooler. After cool-down the optimum working bias of the amplifier is found via variation of the dual-gate bias voltages of the input stage using a R&S FSU spectrum analyzer (Table 3.3).

Table 3.3: Best working point biasing voltages for the cryo-amplifer made at Base collaboration. Please keep in mind this values have varied in time and have to be readjusted every once in a while. Therefore the first row shows what biasing voltages were measured at BASE and the second row shows the biasing voltages at ARTEMIS when paired to the rest of RLC-detection system.

	Gate 1	Gate 2	Gate	Drain 1	Drain 2
Abbreviation	G1	G2	GSF	D1	D2
Initial (BASE)	-1.123	-0.154	1.402	3	3
Later at ARTEMIS	-1.606	-0.177	1.155	3	3

The equivalent input noise e_n of the amplifier in a range of $400\,\mathrm{kHz}$ to $1\,\mathrm{MHz}$ is measured for two instances afterwards. First when the amplifier is biased but not tuned to its best gain rather to the lowest noise figure achievable (Fig. 3.30.(a)). Then the bias of the amplifier is set to its best gain and the e_n is measured again (Fig. 3.30.(b)). Finally using a E5061B ENA vector network analyzer the gain of the amplifier from $250\,\mathrm{kHz}$ to $1\,\mathrm{MHz}$ is measured (Fig. 3.30.(c)). All the output signal of this cryo-amplifier is further amplified using a coaxial ZFL500LN amplifier before readout. Therefore, it is required to do corrections on the values reported, but at the moment due the fact that the gain of the room temperature amplifier is negligible in comparison to the cryo-amplifier and this measurements were performed in an extremely limited time, the required parameters for calculations were not measured (for proper example of this procedure see [99]).

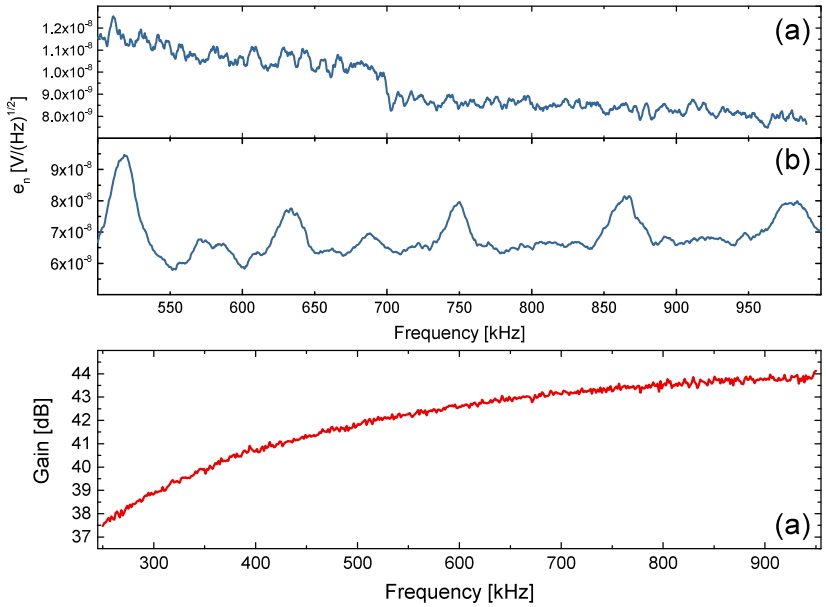

Figure 3.30: Noise figure and gain measurements performed on the amplifier attached to ARES ST in measurement campaign 2016 (done at BASE).

Unfortunately, after many cool-downs and physical modifications related to the RLC- detection system made at BASE, this detection system requires to be repair and undergo extensive tests before being usable again. Building a test stand using a pulse-tube cooler from SUMITOMO RP-082 for cryogenic tests benefiting from a network analyzer at ARTEMIS has started, and currently is work in progress.

3.6 Optical and Laser Detection System

Beside the optimization of the spectroscopy trap of ARTEMIS (as discussed in section 2.3.1), to carry out the laser-microwave spectroscopy (section 2.1) another important requirement is the optical-laser system. Currently a laser with a wavelength of $441\,\mathrm{nm}$ designed for double-resonance spectroscopy of $^{40}Ar^{13+}$ is installed and ready to be used. This optical-laser system is mostly the result of the PhD project of A. Martin at TU DARMSTADT and the detailed description of it can be found in [64].

Figure 3.31 depicts the overall layout of the laser-optical system configuration. The $441\,\mathrm{nm}$ laser used for illuminating the ions consists of four main parts:

- Spectroscopy laser at $441\,\mathrm{nm}$: A DL 100 pro by TOPTICA commercial external cavity diode laser (ECDL), with a maximum output power of $16\,\mathrm{mW}$. The laser is tunable between 439.4 to $445.8\,\mathrm{mm}$, which incorporates the frequency range estimation for observing the fine-structure transition of Ar^{13+}.

- Master laser at $452.756\,\mathrm{nm}$: A custom-made ECDL laser built and characterized at TU

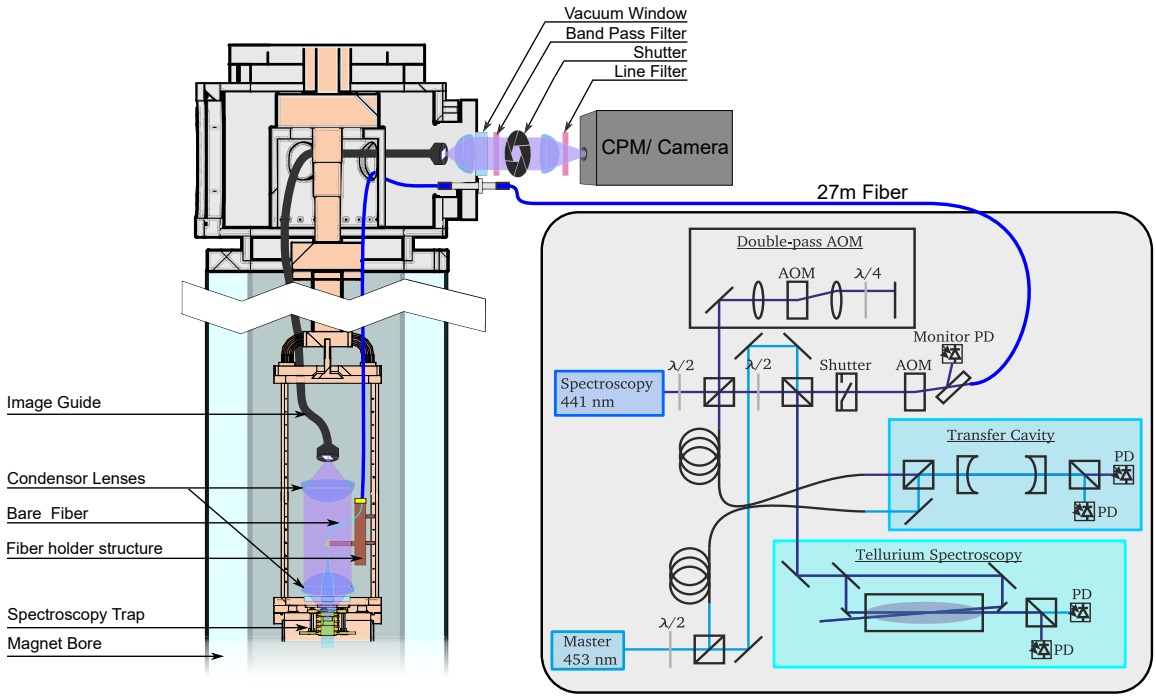

Figure 3.31: The overview of optical and laser detection system at ARTEMIS setup for $^{40}Ar^{13+}$. A 441 nm laser beam is shone on the stored particles via an optical path consisting of the optical fiber and image guide. The emitted light is collected through a custom-made light collimator and transmitted to a CPM or camera through the image guide.

Darmstadt. The stabilization scheme is built upon the master laser which is frequency-stabilized to a tellurium spectroscopy cell and has a long-term stability (over several days) [100, 101].

- Transfer cavity: The resonator is installed with the purpose of frequency stabilization of the spectroscopy laser to the master laser. Utilizing two mirrors with a geometrical distance $l$geo and a medium with refractive index n, the cavity creates equidistant resonance frequencies over the complete spectrum based on longitudinal mode N. The resonance frequencies can be formulated as $\nu = (Nc_0)/(2nl\text{geo})$, with c_0 being the speed of light.

- Doppler-free tellurium spectroscopy: Since optical transitions of tellurium have been well documented in the so-called tellurium atlas[102], they can be used as absolute frequency reference for the spectroscopy of the fine-structure transition of Ar^{13+}. In addition, the frequency stabilization of the master laser can be done using these transitions. The heart of this system is a $^{130}Te_2$-cell, which operates at 504 K in gas phase.

In principle, after heating up the $^{130}Te_2$-cell, using a probe beam and a saturation beam, a Doppler-free spectroscopy according to [103] is established. Afterwards based on the tellurium atlas, a frequency stabilization is performed and an absolute frequency reference is created. Which then the master laser is locked on one of the Lamb dips to stabilize the fre-

quency and through the locking of the length of the transfer cavity to the length corresponding to this frequency, the spectroscopy laser is locked to the master laser. The locking of the spectroscopy laser is done on a different mode of the transfer cavity, using a double pass acousto-optical modulator(AOM) and frequency shifting of the laser. After the laser beam is set to the proper frequency, it is transfered to ARTEMIS with the help of a fiber. The laser setup resides in the laser lab, which is located beneath the HITRAP platform (4.1). Using an optical fiber feed-through on the optical and microwave feed-through flange of the six facet extension (Section 4.2.2) the laser light is coupled into a two meter optical fiber which ends with a section of bare fiber (protective layer removed). The bare end is fixed to a position that the light is collimated and focused using a combination of two condenser lenses into the center of the ST. The holder of the bare fiber is custom-made from OFHC copper to the smallest dimensions technically possible at the time, to decrease the amount of light blocked by the holder. Therefore the efficiency of scattered fluorescence light collection could be improved in comparison to the reported structure in [20]. The final diameter of the laser light delivered to the ion cloud is roughly $3\,\mathrm{mm}$. This laser setup is schematically demonstrated in figure 3.31 along side the optical detection system, which will be described next.

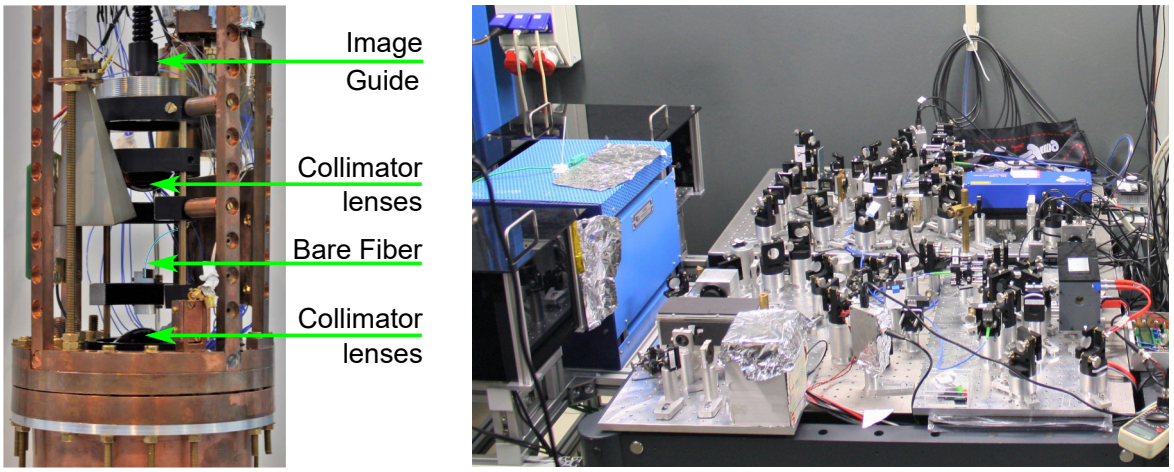

Figure 3.32: Photographs of the optical detection system and the laser setup for performing double resonance spectroscopy. The one on the left shows the new optical structure inside the magnet bore optimized for higher efficiency laser transmission and fluorescence light collection. The picture on the left shows the laser system illustrated earlier schematically.

After using the laser system to excite the trapped ions, the fluorescence response of the ion cloud should be collected, collimated and transfered to the analyzing unit. There are two devices at one's disposal for the fluorescence detection: (1) MP-984 CPM from EXCELITAS (2) The ImagEM X2 EM-CCD camera from HAMAMATSU. The optical path to the detectors includes a bundle of optical fiber, which are structured in a 72×72 square array of fibers with an area of $16\,\mathrm{mm}^2$, the so-called image guide. The first section that the light pass through after it transmits out of the trap chamber through the ITO end-cap and the quartz window is the collimation structure including two aspherical lenses. This structure includes an adapter

where the image guide is mounted on it. After the light passed through the image guide, it is out-coupled from the magnet bore through a window. Due to the fact that in the setup of ARTEMIS there are many components that might emit fluorescence light after illumination with the laser close to the desired $441\,\mathrm{nm}$ light, two purifying filters have been implemented in the light path to the detector. First a band-pass filter with a bandwidth of $10\,\mathrm{nm}$ at a center wavelength of $440\,\mathrm{nm}$ and second a line filter with a bandwidth of $1.7\,\mathrm{nm}$ at a center wavelength of $441\,\mathrm{nm}$ are placed in the beam path. Additionally, two extra collimation lenses are built in to cancel out any light dispersion before detection.

In order to be able to create a delay between the laser illumination of the ion cloud and fluorescence detection by the detectors (to protect the detectors from over-exposer) an shutter has been installed in the beam path outside of the magnet. Figure 3.32 shows the photographs of the laser and the optical detection system.

3.7 ITO Faraday cup

In addition to the non-destructive RLC and optical-laser detection systems, the concept of a Faraday cup has been considered, and the requirements of performing such measurement are also implemented at ARTEMIS. A Faraday-cup measurement scheme is a destructive detection, which is performed by guiding the charged particles to a conducting surface. The created current is normally amplified, measured and translated into the number of particles using an oscilloscope or current meter.

The end-cap electrode of the ST is implemented to be the Faraday conducting surface of this detection system. The ITO window is currently the end-cap of the ST (section 2.3.1), so the durability of it against the HCI bombardment had to be validated. Therefore, an identical ITO window (Thorlabs) was mounted on a special electrode holder with electric connections proper for Faraday-cup measurements and tested in a Drebit type-3 Electron Beam Ion Source (EBIS) at Hilite [56]. The EBIS delivered an ion current with charge states up to around $16+$ and an ion current of several nA at a kinetic energy of $5\,\mathrm{keV}$ per charge to the ITO window every $7.5\,\mathrm{s}$. Using a Femto DHPCA-100 current amplifier the ion current across the conductive layer of the window is translated into a voltage signal and eventually measured on an oscilloscope. Finally, for the sake of comparison the same measurement was performed on a commercial metallic Faraday cup.

The time-resolved results of this measurements is depicted in figure 3.33. As it is apparent despite the different amplitude of the signal of the ITO window and the commercial Faraday cup, which can be explained due to different overall resistances of the measurement arrangement, the overall temporal structure is identical. Hence concluding the functionality of the ITO windows as a Faraday cup. Furthermore this experiment was continued with the de-

scribed harsh condition on the ITO-coated window for an hour, resulting in no noticeable effect on the signal. As a conclusion there should be no obstacles to use the ITO Faraday cup at the cryogenic environment of ARTEMIS with HCI similarly to a metallic one.

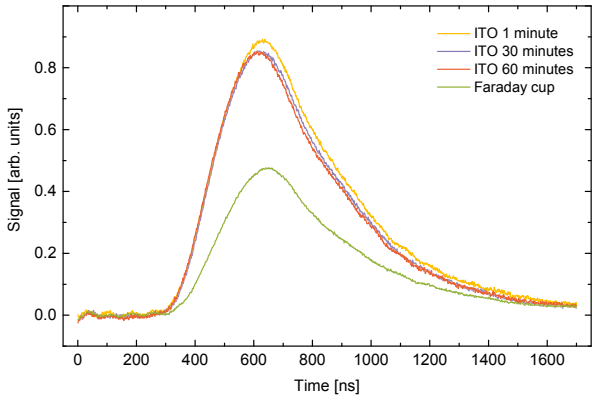

Figure 3.33: Signal comparison of the ITO Faraday-cup verse the commercial one and its stability after an hour of ion impact.

CHAPTER

FOUR

TECHNICAL REMARKS ON THE ARTEMIS EXPERIMENT

ARTEMIS at HITRAP approaches the measurement of bound-electron g-factors in a Penning trap based on optical spectroscopy, such that in comparison to the other g-factor measurement experiments, a good optical access for optical excitation and fluorescence detection is required (Section 2.1). Therefore, many innovative designs are required to achieve the optimizations for an optical measurement method based on the half-open trap concept. In an attempt to facilitate the understanding of the apparatus, Figure 4.1 shows an overview chart of ARTEMIS in its current state. As depicted in the chart, the experiment is based on *eleven* main pillars. Each category of instruments and parts has many details incorporated, requiring equally detailed reports. To achieve measurement goals a well-established connection between different parts is essential. Based on former extensive reports [20, 21] and recent updates, this chapter will provide some technical details. Collectively with technical sections presented in chapters 2 and 3 it should be convenient to get familiar with ARTEMIS .

ARTEMIS, as well as its neighboring trap experiments SPECTRAP and HILITE, are located at the GSI facility, Darmstadt. Hence, it serves justice to first give an introduction of the GSI facility (section 4.1). Section 4.2 discusses three outstanding environmental characteristics of ARTEMIS as a modern precision Penning trap experiment. The cryo- and room temperature filter boards are summarized in 4.3 in table formats for practical use and their recent changes have been noted. The installation of the $65\,\mathrm{GHz}$ microwave system has been done in 2016, which is reported in 4.4. Finally, the gas injection system, a strong candidate for residual gas pressure improvements, is discussed in section 4.5.

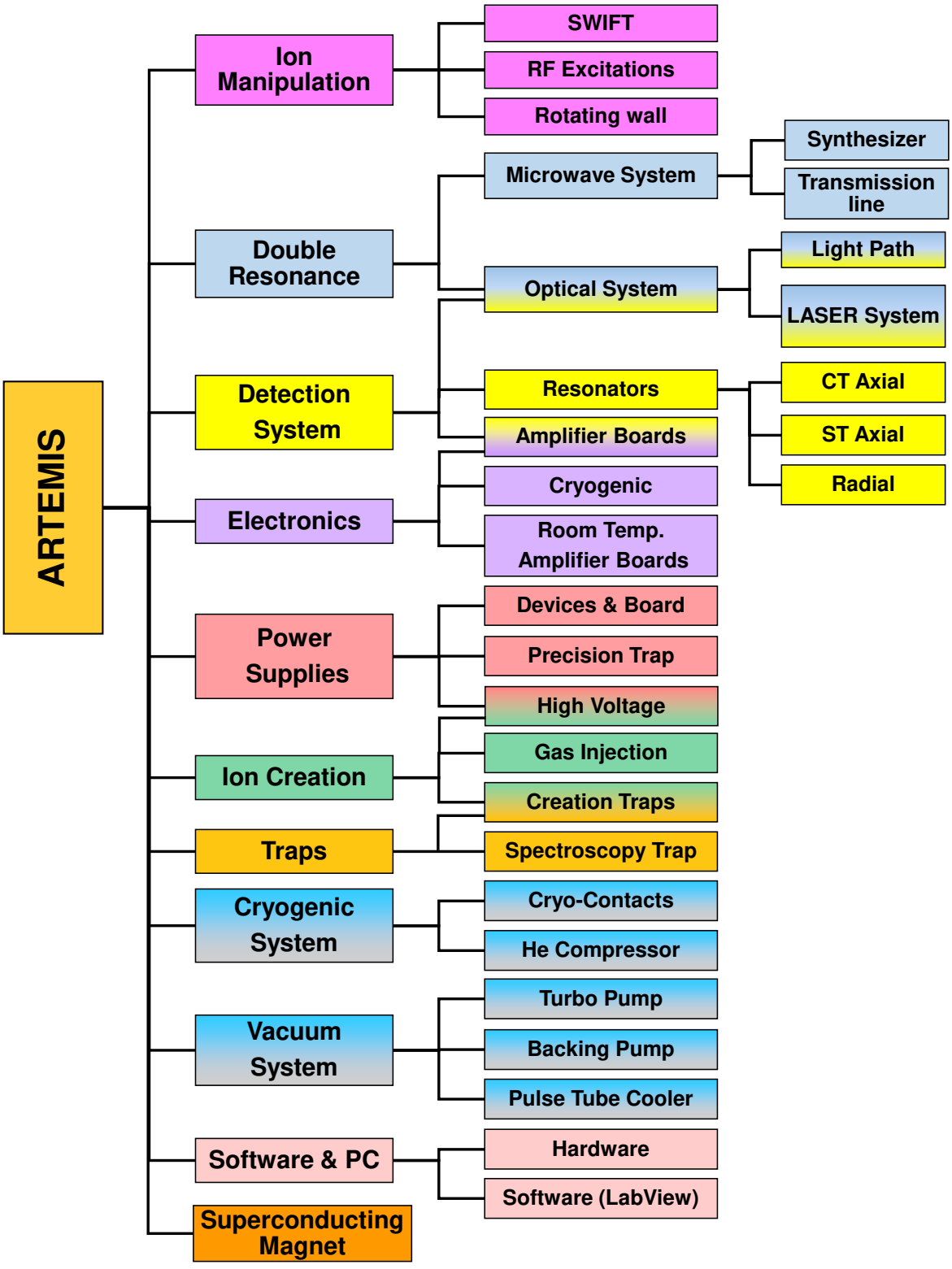

Figure 4.1: The technical relationship chart of ARTEMIS setup, demonstrating eleven main categories of ARTEMIS components. To demonstrate components used commonly by two different sections, the two-color scheme has been applied. The cryogenic and the vacuum systems have mutual influences on each other, thus they are depicted in the same color.

4.1 GSI Helmholtzzentrum für Schwerionenforschung

Located in Darmstadt, Germany, GSI is an accelerator complex providing the possibility of unique heavy-ion research. Figure 4.2 shows an overview of the GSI accelerator center. Among different sections of GSI the Ion Source, Linear Accelerator (UNILAC), Heavy Ion Synchrotron (SIS18) and Experimental Storage Ring (ESR)[4] are crucial for the measurement scheme of ARTEMIS.

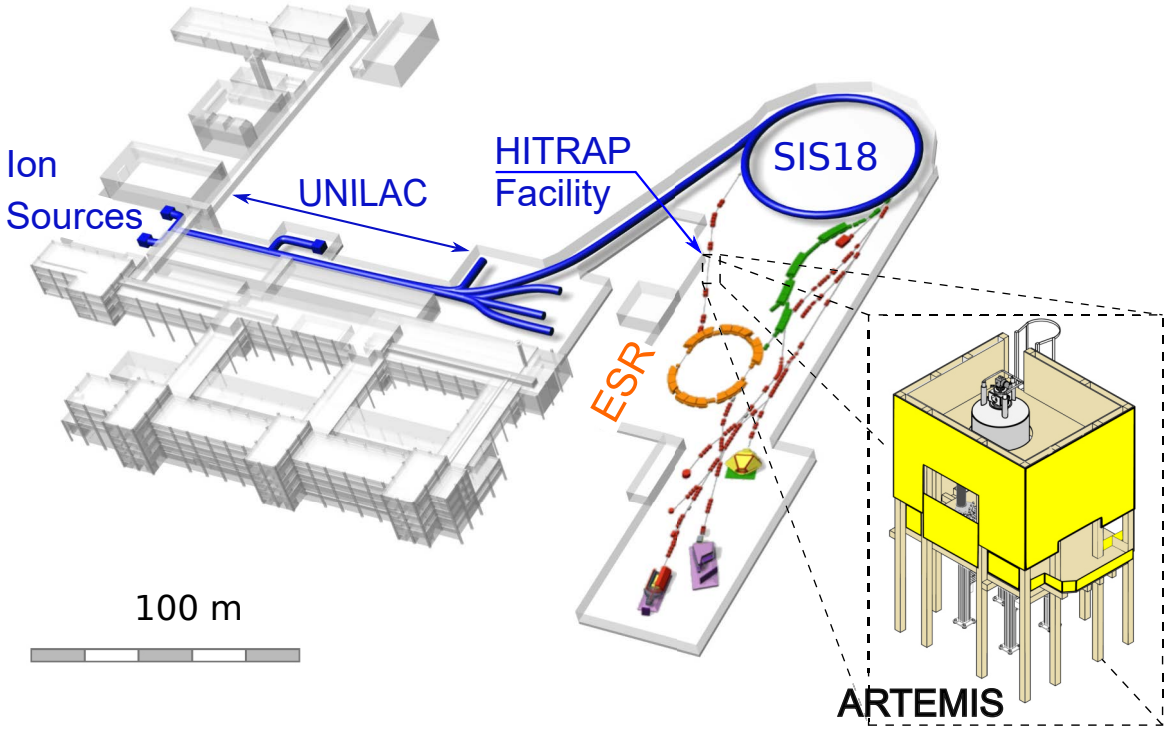

Figure 4.2: Schematic drawing of the GSI infrastructure, showing the important parts of the accelerator facility for ARTEMIS. This drawing is adapted from the PhD thesis of T. Gassner [104] by adding the location of ARTEMIS and its appearance in the yellow painted wooden tower.

Ion Source is the first step of HCI creation at GSI. This section creates a high number of lowly charged ions. To be able to deliver a variety of elements ranging form hydrogen ($Z = 1$) up to uranium ($Z = 92$), seven types of sources are applied. The lowly charged ions are transfered to UNILAC, where they are accelerated to kinetic energies of $11.4\,\mathrm{MeV/u}$. At this stage the ion beam will be further ionized by passing through a stripper-foil, yielding charge states as high as U^{73+}. The peak of ionization energies, $1\,\mathrm{GeV/u}$, at GSI is achieved at SIS18, which means the ion beam can now undergo another stripper-foil, resulting in ions as highly charged as bare uranium. The next step of the HCI journey is the ESR, capable of decelerating and storing the ion beam extracted from the SIS18 with energies up to $560\,\mathrm{MeV/u}$. Besides the possibility of physics experiments being performed at the ESR [4], after decelerating the ions to $4\,\mathrm{MeV/u}$, an extraction for the ions to HITRAP has been implemented. The HITRAP decelerator uses resistive and electron gas sympathetic cooling to further decrease the ion

beam temperature[51], ideally down to $4\,\mathrm{K}$. At this point the ions are transported at $5\,\mathrm{eV/q}$ to the HITRAP-platform beam-line and eventually injected into the experiments located there . To perform an in-flight capture of the ions in ARTEMIS a pulse drift tube is required, which cools down the ions to $4\,\mathrm{eV/q}$ (design principle and drawings found in [105]). It is worth mentioning that the HITRAP-platform beam-line is also equipped with a commercial electron beam ion trap (EBIT) from the company DREEBIT to keep suppling HCI to the experiments even during beam-offline periods.

4.2 Prerequisite Experimental Environment

Strong magnetic field, high vacuum and cryogenic environment are the main three criteria that must have been considered in the design of ARTEMIS. It should be noted that the cryogenic environment is a blessing for the vacuum system, while vacua up to about $1 \times 10^{-16}\,\mathrm{mbar}$ in the trap chamber are achieved via cryo-pumping in ARTEMIS. In the following sections these topics will be reviewed briefly.

4.2.1 Magnetic Field, $7\,\mathrm{T}$

As mentioned before in Section 2.2.1, an essential requirement for any Penning trap is its magnetic field. ARTEMIS applies a $7\,\mathrm{T}$ superconducting magnet (NbTi coil) in persistent-mode made by VARIAN, model number 7T160. The solenoid is immersed in a $300\,\mathrm{L}$ liquid-helium (LHe) reservoir, which is isolated from the room temperature environment by liquid nitrogen and two layers of evacuated-double-wall dewars. All these measures have resulted in minimizing the LHe reservoir refill interval to approximately eight to nine months.

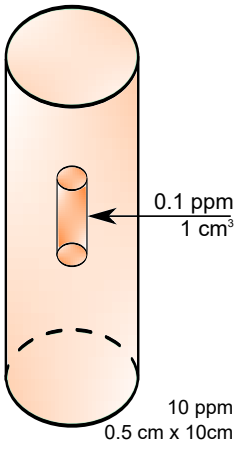

Since the magnet has been energized in 2009 by a current of $210\,\mathrm{A}$, evidence has pointed to a field reproducibility of $7.003\,\mathrm{T}$. By design, this magnet has better stability than $1\,\mathrm{ppm/h}$. Furthermore, at the center of the magnetic field in a $1\,\mathrm{cm}^3$ volume the field should have a homogeneity of $0.1\,\mathrm{ppm}$. In addition, this volume is centered in a cylinder with a diameter of $0.5\,\mathrm{cm}$ and height of $10\,\mathrm{cm}$ homogeneous magnetic field better then $10\,\mathrm{ppm}$. This precious performance is achieved by superconducting shim coils for minimizing field distortion and ferromagnetic material adjusting the magnetic field as close as possible to the theoretical value. The magnet has a cylindrical vertical room temperature bore of $1730\,\mathrm{mm}$ length and diameter of $160\,\mathrm{mm}$. There are flange connections at either end of the magnet bore, enabling it to be used as an isolation vacuum for the experiment. Figure 4.3 shows a section view of the magnet including a zoomed

image of ARTEMIS insert.

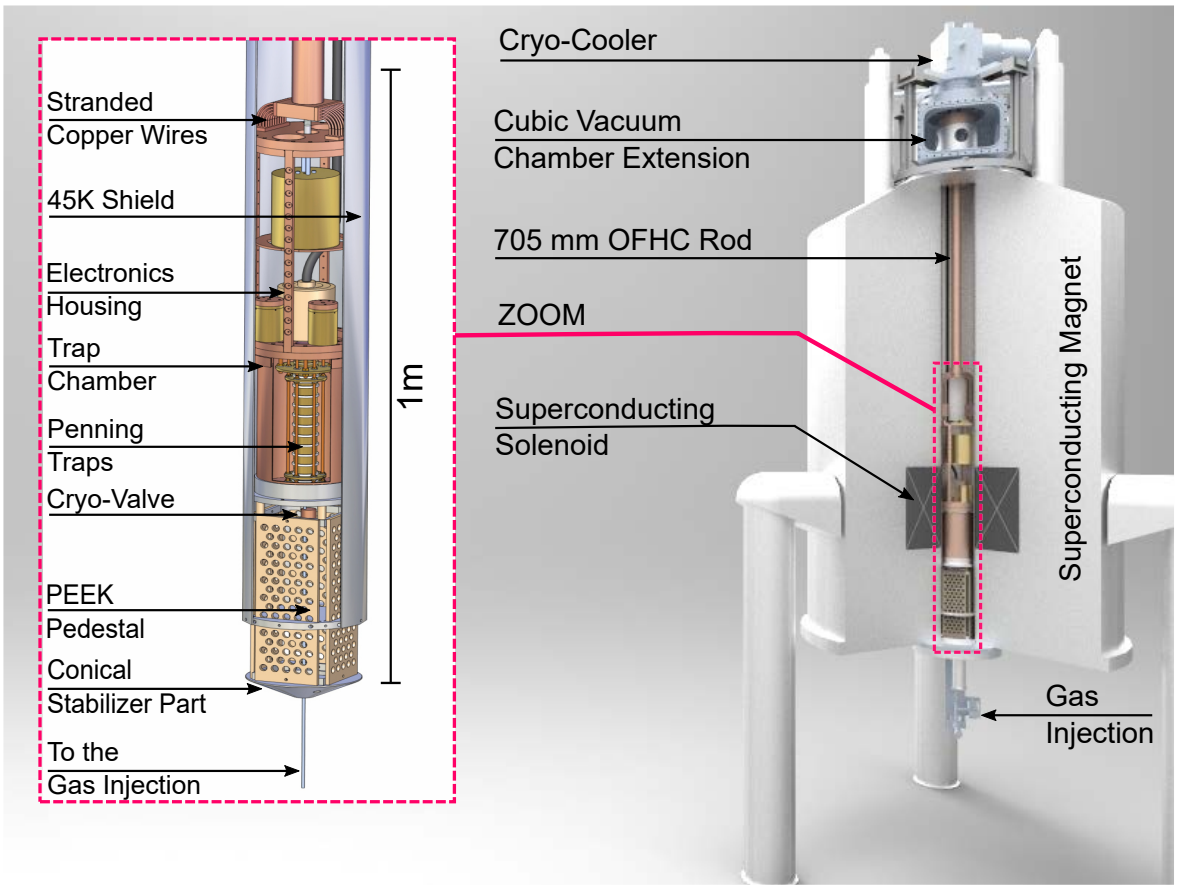

Figure 4.3: ARTEMIS experiment section drawing optimized to demonstrate technical details regarding the superconducting magnet, vacuum and cryogenic system applied. The experiment is inserted in the magnet bore from above and secured on flange connected to the magnet (For a detailed description of mounting the insert please check [21]).

4.2.2 Vacuum System at ARTEMIS

Due to a desire to have long storage times for the HCI, ultra high vacuum conditions are mandatory. Two layers of vacuum have been incorporated in the design of ARTEMIS. The magnet bore has a vacuum of approximately $1 \times 10^{-7}\,\mathrm{mbar}$, while in the trap chamber the vacuum is estimated to be better than $1 \times 10^{-16}\,\mathrm{mbar}$ (section 6.5)

The vacuum of the magnet bore is achieved through sealing the bore with a rubber gaskets and CF flanges. The flange on the bottom has a KF40 connection for the Edwards AIGX active ion gauge, reading pressures down to $6 \times 10^{-10}\,\mathrm{mbar}$. Also the gas injection system is mounted using this flange (explained in more detail in section 4.5). On the top part, the magnet bore is closed by a cubic vacuum chamber extension with six CF flange structures on each facet as listed in the following:

- Magnet bore connection

- LEYBOLD Mag W 400 P turbo-molecular pump
- Optical and microwave feed-through
- High-voltage feed-through
- Room temperature filter board feed-through
- SUMITOMO SRP-082B-F-70H pulse-tube cooler.

The LEYBOLD Mag W 400 P turbo-molecular pump is backed with an EDWARDS RV12 pump, and the exhaust is monitored by an EDWARDS APG active Pirani vacuum gauge. This vacuum system is the means of reaching a primary vacuum of $1 \times 10^{-7}\,\mathrm{mbar}$. The ultra high vacuum (UHV) is obtained due to the cryo-pumping effect in the semi-closed trap chamber. The chamber is composed from the UMF and the cylindrical chamber, both from OFHC copper. They are connected to each other using sixteen brass screws and the sealing is achieved by an indium wire ring. The UMF is the part where all feed-throughs for the connections of the trap are mounted.

4.2.3 Cryogenic Environment

Besides the UHV, operating a Penning trap at $4\,\mathrm{K}$ reduces the electronic noises and enables the use of a superconducting detection scheme. A cooled ion cloud at $4\,\mathrm{K}$ possess a lower motional amplitude, resulting in a smaller deviations from their theoretical motional and optical frequency.

The heart of the cryogenic system is the SUMITOMO RP-082 $4\,\mathrm{K}$ pulse-tube cryo-cooler. Cold head, helium compressor and $20\,\mathrm{m}$ helium gas lines are the three main parts of this system. The cold head has two cooling power stages, the first stage of $40\,\mathrm{W}$ at a temperature of $45\,\mathrm{K}$ and the second stage of $1\,\mathrm{W}$ at a temperature of $4.2\,\mathrm{K}$. The first stage is responsible for thermally isolating the second stage and the inner parts of the experiment via an attached thermal shield. The shield is cover with 'Coolcat 2' superinsulation foil from RUAG, resulting in a significant radiation thermal load reduction [74].
The $4.2\,\mathrm{K}$ stage is where the main inner part of the experiment is assembled on using a $705\,\mathrm{mm}$-long OFHC copper rod. The pulse-tube cooler produces undesired vibration, therefore a set of 24 stranded copper wires with a total cross section of $240\,\mathrm{mm}^2$ ensure thermal coupling and with vibrations isolated from the experiment.
The inner parts of ARTEMIS consist mainly of the electronics 4-leg frame and the trap chamber. The 4-leg housing is where the two filter boards (high and low voltage), the detection system, optical connections and microwave system are located. The trap chamber hangs downwards from the 4-leg housing and through the UMF the two Penning traps inside the

trap chamber are cooled down to temperatures around $4\,\mathrm{K}$.
Further measures are also taken to decouple the system from external heat-loads. Such as resting the entire insert on a pedestal of four PEEK (polyether ether ketone) boards. PEEK has low thermal conduction ($0.25\,\mathrm{mW/m}$). Also for the sake of alignment and stability this pedestal structure is connected to a conical part resting on the lower magnet flange (figure 4.3).

4.3 Electronics (Filter Boards)

The electronic system of ARTEMIS has two main functionalities, amplification and filtering. These electronics can be divided into room-temperature and cryogenic categories. The cryo-amplifiers been covered in section 3.5, due to the fact that they are an inseparable part of the detection systems. A low-noise environment is an essential part of the setup scheme, based on two facts: The signal of the trapped ions is easily obstructed by the noise signal and external high-frequency noise on the trap electrodes can heat up the stored ion cloud. ARTEMIS incorporates room-temperature and cryogenic filter boards. An updated version of the wiring diagram of ARTEMIS is presented in appendix A.

Room-temperature Filter Boards

The room-temperature filter boards have been specifically developed for ARTEMIS by Stahl Electronics. There are four different filter boards, which are mounted on a dedicated flanges of the cubic vacuum chamber extension. They are shielded in a cubic housing, also on its side a mount for the UM power supply is considered. These filter boards include low-pass filtering on the DC supply lines (with cutoff frequencies of about 130 to $300\,\mathrm{Hz}$ for different electrodes), low noise amplifiers (noise density approx. $1.2\,\mathrm{nV}/\sqrt{\mathrm{Hz}}$) and frequency down-conversion on the ST/CT ARES and CRES signal.In addition, the rf lines are also filtered. Table 4.1 provides a summary of key features of them. The varactor diode heater voltage supply line has been added to the HE1 in 2017 (The purpose of adding the varactor diode is explained in 3.4), besides this line no other changes have been done on the room-temperature filter boards.

Cryo-Filter-Boards

There are two cryo-filter boards, the low-voltage (LV) and the high-voltage (HV) filter boards. These boards are mounted on the 4-leg housing close to the UMF, using a copper board screwed to the back side of the filter boards. The LV board performs filtering, damping,

Table 4.1: An overview of the room-temperature filter boards. Including their functions, input, output connections and their available connectivity. This table is based on [20] and documentation of filter boards by STAHL ELECTRONICS

HE 1	
Functions	Temperature sensors and heaters filtering
Input	Heaters voltage supplies, varactor diode heater voltage supply
Output	Temperature sensors readout
Connectivity	25 pin male Sub-D socket.
HE 2	
Functions	Low voltage trap filtering, varactor diode board biasing, rf excitations
Input	Low voltage trap biases, varactor diode board bias, all rf inputs except S3 supplies (TS-LC,CT-Exc. Ax., CT/ST Magn. Exc), S5 AC/DC coupling
Output	Faraday-cup readout signal (currently grounded)
Connectivity	9 pin female Sub-D socket (BS device), 6 rf SMA connectors, 4-banana connectors (UM) and power connector ($5\,\mathrm{V}$ and GND)
HE 3	
Functions	Filtering the cryo-amplifiers supply lines, ARES signals amplification, optional signal down-conversion of one of ST/CT channels
Input	Two down-conversion reference frequencies, ST/CT ARES multiplexer control signal, cryo-amp biases,
Output	Down-converted ARES signal output, ST ARES line out, CT ARES line out
Connectivity	15 pin female Sub-D socket (cryo-amp biases), 6 rf SMA connectors and power connector
HE 4	
Functions	readout filtering, down-conversion and amplification of CRES signal, cyclotron motion excitation(dipole/rotating wall)
Input	Rotating wall (4 coaxial line in), Dipole excitation, PCI-card $5\,\mathrm{V}$ control voltage, down-conversion reference frequency
Output	CRES Signal
Connectivity	9 rf SMA connectors, impedance selector key and power connector

cooling of incoming lines and rf excitation coupling/decoupling into some DC bias voltage electrode. Table 4.2 shows a summary of these excitations and their relevant electrodes.

Two important notes about the LV board are as following:

- Resistors with values of approximately $50\,\mathrm{k}\Omega$ have been installed at the input of each

line. Hence, one can validate proper connection of them versus the GND.

- RC high-pass filters have been implemented on the lines involving S2, S4.5 and C13, because these electrodes are a part of the RLC-detection system (discussed in section 3.1). Also via a $2\,\mathrm{pF}$ capacitor a test line, TS-LC, has been coupled with all three resonators for test and maintenance reasons.

The HV board has five channels of low-pass filters for electrodes H8, H9, H19, F1 and F2. The original design incorporated a $30\,\mathrm{M\Omega}$ resistor and $37\,\mathrm{pF}$ capacity boards. The resistors (SLIM MOX10203 RM 10,16) have proven over time to be not suitable for the cryogenic environment, breaking into pieces as a result of cooling cycles. Therefore, these resistors have been replaced by two $10\,\mathrm{M\Omega}$ resistors is series (Vishay CRHV2010AF10M0FKET), that have been cooled down to $45\,\mathrm{K}$ and warmed up to $300\,\mathrm{K}$ more than fifteen times and withstood against damages.

Table 4.2: The excitations coupled through the LV board to the DC biased electrode and their effect on the stored ion cloud [20].

Electrode	rf Excitation	Functionality
S3	Rotating wall Oscillating dipole field exc.	Radial compression Cyclotron motion excitation
S4.0 & S15.5	CT/ST Magnetron exc.	Quadrapole mixing of axial and radial motion
S5 & S16	Dipole field	Axial excitation at respective trap

4.4 The 65 GHz Microwave System

As already mentioned in Section 2.1, to be able to perform the Microwave-laser spectroscopy scheme on Ar^{13+} two microwave bandwidths are required (ν_L): $65\,\mathrm{GHz}$ for the two ground-state $2^2\mathrm{P}_{1/2}$ transitions and $130\,\mathrm{GHz}$ for the four excited-state $2^2\mathrm{P}_{3/2}$ transitions (figure 2.4). The $65\,\mathrm{GHz}$ system has been designed and implemented in ARTEMIS in the year 2016, which can irradiate microwave signals within frequency range of $64 - 66\,\mathrm{GHz}$. A comprehensive review of the system is presented in [21].

The design of the microwave system follows five main principles: sufficient microwave power delivery to the ST (low loss), constructional and space limitations, low thermal conductivity, leak-tight vacuum feed-through availability, high magnetic field compatibility. To tackle technical challenges achieving these aims a system based on hybrid-transmission line was developed. Figure 4.4 depicts the parts and devices used in this system, which will be elaborated further in the following.

The first part of the system is the GT9000 microwave synthesizer from GIGATRONICS. Based on two YIG (Yttrium Iron Grant) oscillators, it is capable of delivering microwave signals of 2-20 GHz. The benefit of a YIG oscillator is its high quality factor, resulting in a low-phase noise. In other words, this device has high short-term frequency stability. To ensure the long-term frequency stability of the microwave signal a $10\,\mathrm{MHz}$ external rubidium frequency standard (SRS FS725) is applied. The stability of the frequency and output power is monitored by a EIP Microwave source Locking Microwave Counter (Model 578). Nevertheless, the output frequency of this device has to be matched with the desired ν_L. Hence, by using an active frequency quadrupler from CERNEX (CFM1616X410-01) and tuning the output frequency of the synthesizer between $16-16.5\,\mathrm{GHz}$, the $64-66\,\mathrm{GHz}$ is achieved. As a safety measure the quadrupler is equipped with an isolator, which attenuates the reflected waves.

The quadrupler has a power input-output ratio of one with maximum power input of $10\,\mathrm{dBm}$, limiting the $13\,\mathrm{dBm}$ output of the synthesizer. Considering the fact that the microwave signal must travel through many lossy stages and lines before it is delivered to the ions at the ST, a power amplifier(SP654-15-24-W) from SPACEK is add to the Microwave system. At frequency of $65\,\mathrm{GHz}$ a gain of $19.8\,\mathrm{dB}$ and a maximum output power of $23.2\,\mathrm{dBm}$ is reported in test data sheet of the device. A mechanically-tuned attenuator from MI-WAVE (520E) has been considered to make the amplitude of the microwave system tunable. This attenuator has frequency operation range of $60-90\,\mathrm{GHz}$ and attenuation range of $0-25\,\mathrm{dB}$.

The most prominent part of the microwave system design is the transmission line, which is made of a combination of coaxial cables and WR-12 waveguides. Due to the dielectric isolation of the cables, their losses is higher then waveguides. Nevertheless, availability of commercial vacuum feed-thorough for coaxial cables and low bending radius makes there use convincing. The following components are used in the current design of the transmission line of ARTEMIS from the output of the attenuator to the horn antenna:

- **Room temperature Waveguide-to-Coax adapter:** Since the output of the Attenuator is a waveguide connection an adapter to coaxial cable is required. This adapter converts the TE_{10} mode of the microwave to TEM mode. This adapter works based on the principle of applying the inner conductor as an antenna inside the waveguide. A loss of $0.6\,\mathrm{dB}$ is reported by the manufacturer, DUCOMMUN (PTC-12VM-01).

- **Room temperature coaxial cable:** A $1.85\,\mathrm{mm}$ V-type connector cable from ASTROLAB with a length of $50\,\mathrm{mm}$ is connecting the adapter and the feed-through. The loss of this cable has been measured to between $0.6-1\,\mathrm{dB}$.

- **Feedthrough:** A commercial vacuum feed-through with $1.85\,\mathrm{mm}$ connectors from SHF-(KPC185FFHA) is screwed into a CF-flange. An insertion loss of $<0.7\,\mathrm{dB}$ and

He leak range of $10^{-9}\,\mathrm{mbar}\cdot\mathrm{L/s}$ is mentioned in the technical specifications.

- **Cryo-Coaxial cable:** This section of the transmission line has to be bent a couple of times, in order to reach into a space of the setup which a straight waveguide can be mounted again. A $0.5\,\mathrm{m}$ long low-thermal-conductivity, non-magnetic cable, with low bending radius of $3.3\,\mathrm{mm}$ from KMOC (SC-119/50-SB-B) with $1.85\,\mathrm{mm}$ connectors is applied. This cable has $14\,\mathrm{dB/m}$ loss at a frequency of $65\,\mathrm{GHz}$.

- **Cryo-Coax-to-Waveguide adapter:** Converting a $1.85\,\mathrm{mm}$ coaxial cable connection to a WR-12 waveguide connection, this adapter is built by MI-Wave and has an insertion loss of $1\,\mathrm{dB}$.

- **Waveguide:** An E-band wave guide ($60-90\,\mathrm{GHz}$) from Mi-Wave made of OFHC copper without gold plating[1] is chosen for the current system. This waveguide is $950\,\mathrm{mm}$ long and uses UG-387/U flange connection standard. It has a $3.11-1.74\,\mathrm{dB/m}$ loss according to the specification sheet of the manufacturer. It should be noted that the losses of this waveguide at $4\,\mathrm{K}$ noticeably decrease due to increase of its conductivity. The waveguide has 11° bending at the last few cm, which gives an angle to the horn antenna connected to it with respect to the position of the ions.

- **Horn Antenna:** The final part of the transmission line is a pyramidal horn antenna from MI-Wave(261E), which is designed to deliver a high gain in the center forward direction.

The overall loss of the transmission line based on the data sheet of the parts involved is calculated to be $13.2\,\mathrm{dB}$ and further measured in tabletop measurements to be $12.9\,\mathrm{dB}$. Considering the material that is located between the ions and horn antenna, especially the IT-coated window, a total power reduction of $37\,\mathrm{dB}$ can be estimated. As a result, the microwave system described in this section can deliver a power ranging from $-61\,\mathrm{dB}$ to $-12\,\mathrm{dB}$ (or 0 to 50 $\mu\mathrm{W}$) to the ion cloud in the ST. Thus, fulfilling the required estimated microwave power for the $65\,\mathrm{GHz}$ Zeeman transition, which is of order of $10\,\mu\mathrm{W}$ [48].

4.5 Gas Injection System

To inject argon gas into the creation trap (CT) without compromising the vacuum condition, an injection system made of two main parts has been developed. The pressure regulation, known as the pre-chamber and the cryo-valve. The first generation of this system has been

[1] Gold plating requires a nickel diffusion barrier, which is highly magnetic. But, normal coating results in lower transmission losses.

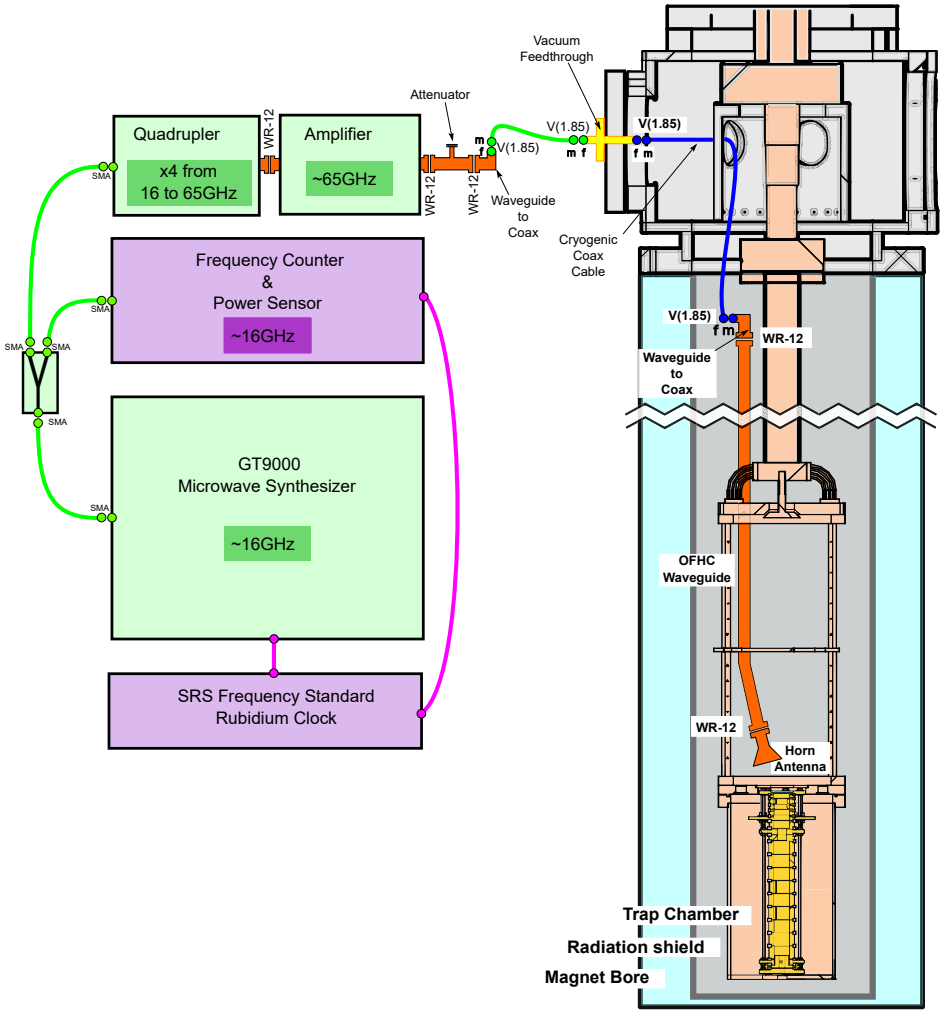

Figure 4.4: An overview of the 65 GHz microwave system of ARTEMIS.

reported in detail in [20]. Currently, the pre-chamber has undergone two updates and here the third iteration will be reported.

The required argon gas is provided from a $10\,\mathrm{L}$ compressed argon bottle with a 4.8 gas purity. Using a pressure regulator, the argon pressure is regulated to around $1\,\mathrm{bar}$. The pre-chamber reduces the pressure further to a value between $0.6 - 0.65\,\mathrm{mbar}$. Figure 4.5.a shows a schematic of the pre-chamber. The center-piece of the pre-chamber is a simple KF 16 cross which has four parts attached to it: two Pfeiffer vacuum EVN 116 gas dosing valves, an Edwards APG100 active pirani vacuum gauge and a KF 16 to swagelok adapter. One of the dosing valves is connected to the argon bottle and the other one to a Edwards oil-sealed backing pump, in a manner that they control the injected gas and vacuum flow respectively. To obtain $0.6 - 0.65\,\mathrm{mbar}$, based on the digital position indicator of the valves [106], argon gas flow (in) of approximately $7 \times 10^{-6}\,(\mathrm{mbar} \times \mathrm{L})/\mathrm{s}$ and the rest gas removal with circa $6\,(\mathrm{mbar} \times \mathrm{L})/\mathrm{s}$ is needed. This setup only provides a dynamic pressure regulation, meaning that argon gas is simultaneously injected and pumped out. Creating a well-defined static

regulated gas injection solution has technical challenges due to the high magnetic field of about ($5\,\mathrm{mT}$).

After the KF-SWAGELOK-adapter two shot-off valves are installed, first a compressed air automatized valve and then a manual one (both from SWAGELOK). The manual valve is used for no-gas-injection-creation-periods and maintenance. The automatized valve is capable of opening times as low as $24\,\mathrm{ms}$ and is the one that is in use most of the time. The gas is passed through a low thermal conductivity stainless steel tube to the cryo-valve, entering the magnet bore via a O-ring sealed compression port.

The so called cryo-valve is the last connecting piece of the gas injection system to the trap chamber. Since this connection is positioned at cryogenic temperatures and close to the center of magnetic field, using mechanical moving parts to totally seal the trap chamber is unfeasible. The solution was also presented based on cryo-pumping effects and high sticking coefficients of metals at available temperature ranges of ARTEMIS, in this case below $15\,\mathrm{K}$. Applying a meander shape connection made out of OFHC copper as in figure 4.5.b would result in a total blockage of the gas leak into the trap chamber. For driving the cryo-valve into open status, simply heating the structure to temperatures above certain ranges (around $20 - 30\,\mathrm{K}$) will be sufficient. In conclusion, to deliver gas to the trap chamber the cryo-valve is heated up and the compressed-air-control shot-off valve allows the gas to flow through. After the heating of the cryo-valve is turned off, the temperature declines rapidly below the closing limits.

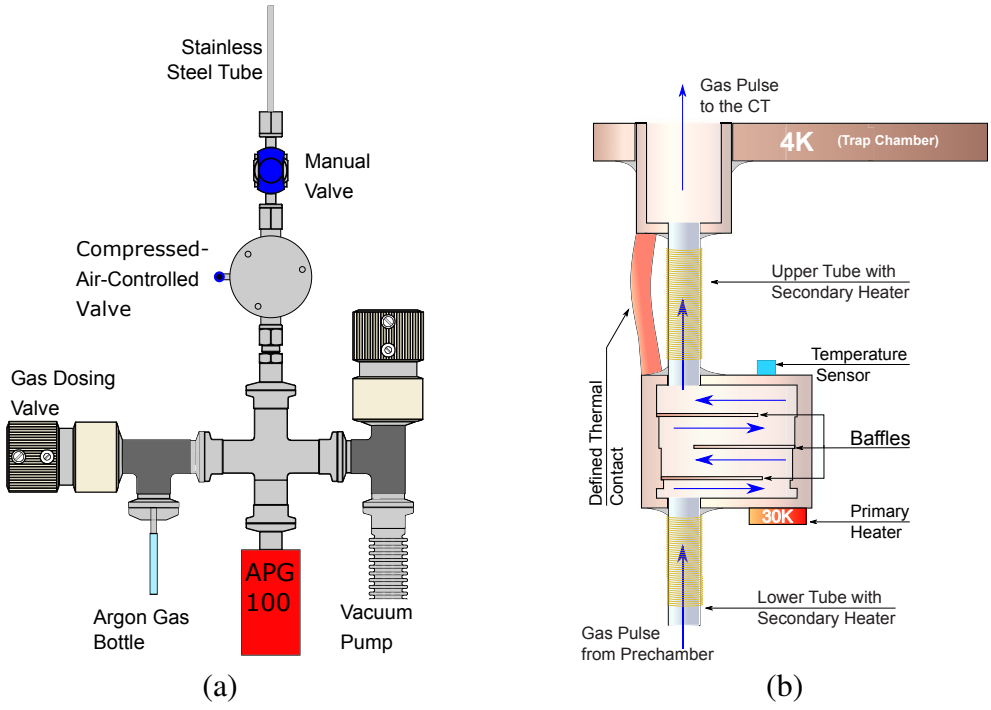

Figure 4.5: The gas injection system at ARTEMIS (a)Schematic of the third generation of pre-chamber structure. (b) Schematic drawing of the cryogenic valve adapted.

The efforts to improve the gas injection system have lead to an improvement of the residual gas pressure in the trap chamber to about $3 \times 10^{-16}\,\mathrm{mbar}$, which will be discussed in section 6.5. To further improve the gas injection system, it is recommended to replace all non-KF standard parts of the pre-chamber with equivalent KF parts, resulting in lower leak rates and better vacuum at the pre-chamber and consequently at the trap chamber.

CHAPTER

FIVE

ION COOLING AT ARTEMIS

An advantage that makes Penning traps unique for precision spectroscopy is the possibility to cool the motion of the trapped particles. In doing so, three main advantages are achieved: (1) longer trapping times (2) higher precision of measurements (3) cooling makes all kinds of ion cloud manipulation easier [107]. In comparison to similar experiments done at high energies—for example the ones performed at the experimental storage ring (ESR) at GSI [4] (section 4.1)—by cooling the ions the Doppler broadening is reduced significantly, hence, increasing the precision of the spectroscopy. Also for a high-precision g-factor measurement cooling is essential, since reduction of the velocities decreases the uncertainties arising form relativistic mass increase and electric potential anharmonicities [107].

In the course of Penning trap application through the years, many cooling techniques have been developed and utilized for the trapped particles. Resistive cooling [65], laser cooling [107], buffer gas cooling [1][50] and sympathetic cooling [108] are among the most important ones. Currently, ARTEMIS at HITRAP is benefiting from three RLC-circuits, which can be used to cool the axial and radial motions at the spectroscopy trap (ST) and the creation trap (CT). Future plans for using a beryllium sympathetic-laser cooling scheme at the ST of ARTEMIS have been considered (appendix B).

In this chapter first an introduction about the concept of temperature for confined particles is introduced and afterwards the cooling phenomena present at ARTEMIS are discussed. Currently, resistive cooling is the most prominent procedure for reducing the motional ion energy at ARTEMIS more details are presented. Furthermore, the effort done in the course of this project for a more accurate interpretation and calculation of the effective electrode distance D is reported.

[1] due to strong magnetron losses not a preferable method for Penning traps

5.1 The Concept of Stored Ion(s) Temperature

The number of particles N is an important factor while discussing the concept of temperature, commonly it is required to have a large enough ensemble of particles ($N \rightarrow \infty$) for associating a temperature to a physical system. Nevertheless, under some circumstances a temperature can be related to a single particle. It is required that first the particle is in thermal equilibrium with a sufficiently large thermal bath at temperature T, then through a repeated motional energy E measurement the probability of obtaining a certain value for the energy follows an exponential $\exp(-E/k_BT)$, with k_B being the Boltzmann constant [109]. In order to apply this approach the system must fulfill the ergodic theorem [110], which in cases such as ARTEMIS this theorem is fulfilled.

In an ideal Penning trap three independent degrees of ion motion are observable, the axial, the reduced cyclotron and the magnetron motions (section 2.2.1). For each of them the amplitude of the particle oscillation is a direct measure of its kinetic energy and an individual temperature can be assigned to them. The typical field imperfections in a Penning trap usually causes an entanglement between these particle motions. Nevertheless, each of the degrees of freedom can acquire an independent temperature dominated by their respective equilibrium thermal bath. Also the temperature of the thermal baths is defined by the temperature of the charge carriers in their conductive components and electronic circuitry [109]. Furthermore, the energy independence of these three particle motions, translates to the fact that they can be either excited or cooled without affecting the temperature of the other two degrees of freedom. Due to the negative total energy of the magnetron motion, it should be treated separately in comparison to the other degrees of freedom [50]. Usually, there are several ways to measure the temperature of a single or ensemble of ions in a Penning trap , such as electronic noise [109], fluorescence line shape [111], magnetic bottle [109] and active motional coupling temperature measurement[43].

5.1.1 Electronic Noise Temperature Measurement

Among the mentioned temperature measurement techniques the electronic noise temperature detection is a technique that can be easily applied at ARTEMIS. To apply such an method it is required to first ensure that the particles are in thermal equilibrium with the detection circuit. Afterwards the level of the Johnson noise U_n is extracted from the measured spectrum of the resonator circuit and using the readout bandwidth set on the spectrum analyzer the temperature evaluation follows

$$T = \frac{U_n^2}{4k_B B_f R_P}. \tag{5.1}$$

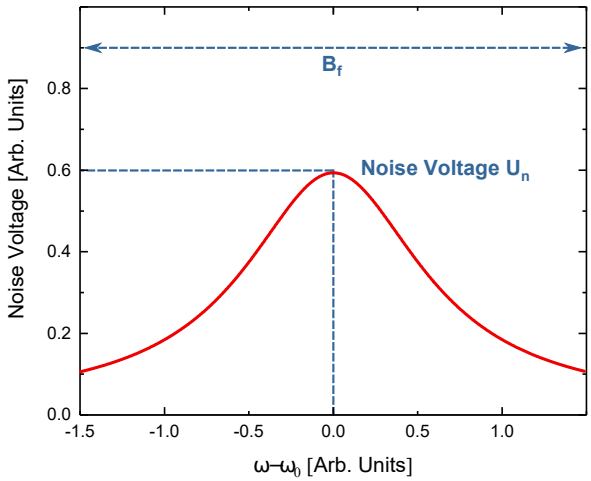

Figure 5.1: Resonance spectrum of a detection system and relevant quantities used to extract temperature by electronic noise measurement approach. U_n is the amplitude of the signal readout and B_f is the bandwidth of used to record the spectrum.

Here k_B is the Boltzmann constant and R_P is the resonator resistance of the RLC-circuit. The typical quantities used for performing such calculations are shown in figure 5.1. For a proper calculation it is required to calibrate the attenuation and amplification of the rf circuit between the detection system circuit and spectrum analyzer, by accounting for the attenuation of the circuitry in the line of measurement and the amplification performed on the signal feed into the spectrum analyzer.

5.1.2 Spectral Width of the Axial Frequency as a Measure of Temperature

The imperfections of the confining fields in a non-ideal Penning trap lead to a frequency distribution of the axial ion motion frequency. This energy-dependent shift comes from the higher-order terms of the axial electrostatic potential, measured by coefficients C_4 and C_6 as defined in section 2.2.2. Based on the discussion presented in [42, 59, 15], for an ion ensemble close to thermal equilibrium with negligible contribution from magnetic field imperfection, the dependence of the thermal axial frequency width is given by

$$\frac{\delta\omega_z}{\omega_z} \approx \frac{15}{4}\frac{C_4}{C_2}\frac{k_B T}{qU_0} + \frac{75}{4}\frac{C_6}{C_2^2}\left(\frac{k_B T}{qU_0}\right)^2 . \tag{5.2}$$

At a given trapping potential U_0, for a Penning trap that the C_2, C_4 and C_6 coefficients are known, the temperature of the ion cloud can be estimated by measuring the center frequency and the spectral width of the confined axial ion ensemble. Considering the values of $C_2 = 0.56$, $C_4 = 0.001$ and $C_6 = 0.05$ at the CT of ARTEMIS, with a trapping potential of $U_0 = 55.7\,\mathrm{V}$ for Ar^{13+}, the expected relative signal width as a function of the ion ensemble temperature is depicted in figure 5.2.

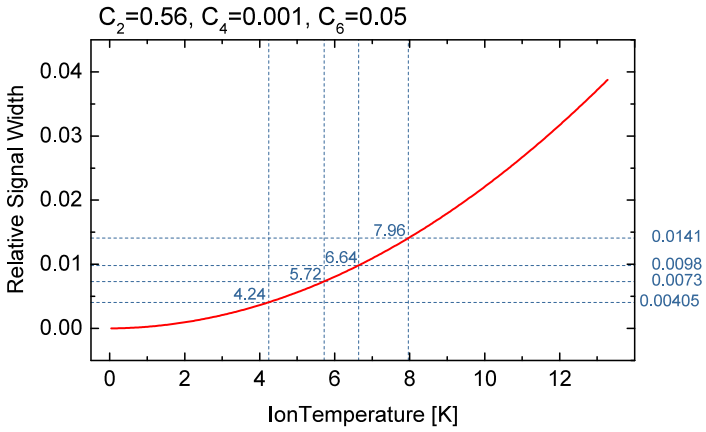

Figure 5.2: Expected relative signal width as a function of temperature at the CT of ARTEMIS. The values mentioned in the plot are related to the result presented in section 6.7 for the different cooling measurement.

5.2 Ion Cooling in Penning Traps

After loading or creating an ion cloud into a Penning trap the temperature can range up to a few orders of magnitudes higher than the equilibrium temperature of the interacting thermal bath. Hence, several techniques may be applied to decrease the temperature down to the quantum mechanical ground state of the ion motion of trapped particles. The detailed description of cooling techniques are available in [107, 50]. Thus only a brief review of the cooling schemes that are relevant for ARTEMIS will be presented, with an exception of the resistive cooling which will be explained in further detail.

5.2.1 Buffer Gas Cooling

If alongside the trapped charged particles buffer gas (neutral species) is present in a trap, the collisions between them leads to an energy equilibration mechanism commonly referred to as buffer gas cooling. In comparison to the other cooling techniques, buffer gas cooling reduces the motional frequencies of all three degrees of freedom at the same time and it is effective on a broad range of temperatures. Nevertheless, the control over this cooling phenomenon is limited and as a result it can cause ion loss through increasing the magnetron radius. A solution of such a problem would be to couple this cooling procedure with magnetron centering (Section 5.2.3) [107, 112]. Buffer gas cooling can be modeled as a frictional force acting on the particle motion, for example the axial energy is reduced with damping rate γ_b as follows

$$\frac{\partial E}{\partial t} = -2\gamma_b E = -\frac{q}{m}\frac{1}{M_0}\frac{pT_0}{p_0 T}, \tag{5.3}$$

here M_0 is the particles' mobility in buffer gas at p_0 =1013 hPa and T_0 =300 K [113]. A damping of the radial motion as a consequence of the axial particle motion reduction for this

cooling method reads as

$$\gamma_{\pm} = \pm 2\gamma_b \frac{\omega_{\pm}}{2\omega_+ - \omega_c}, \tag{5.4}$$

which yet again demonstrates that the reduced cyclotron radius decreases, whereas the magnetron radius increases, resulting in undesired particle loss. Due to the low residual gas pressure estimated at ARTEMIS (section 6.5) the effect of buffer gas cooling should be negligible, but still present.

5.2.2 Evaporative Cooling

The evaporative cooling is a result of losing the hottest trapped particles in a sufficiently shallow trapping potential. By allowing the ions with highest kinetic energy to leave the trap, the rest of the confined particles will equilibrate to a lower temperature. Nevertheless, as a side effect of such an approach the final number of confined particles will be reduced. An example of evaporative cooling of HCI is reported in reference [114]. For analytical understanding a Maxwell-Boltzmann thermal energy distribution is assigned to the ion ensemble. In this case, the probability distribution as a function of energy E reads as

$$p(E)dE = \sqrt{\frac{4E}{\pi}} \left(\frac{1}{k_B T}\right)^{3/2} exp\left(-\frac{E}{k_B T}\right) dE \tag{5.5}$$

with $\int_0^{\infty} p(E)dE = 1$ in this manner a fraction of particles f with kinetic energies above a certain level E' is depicted as

$$f = \int_{E'}^{\infty} \sqrt{\frac{4E}{\pi}} \left(\frac{1}{k_B T}\right)^{3/2} \exp\left(-\frac{E}{k_B T}\right) dE, \tag{5.6}$$

thus the value f indicates the fraction of trapped particles that leave the trap after lowering the trapping potential to $U_E = q/E'$. Figure 5.3 demonstrates schematically the evaporative cooling stages. This kind of ion cooling phenomena is generally seen at the initial internal

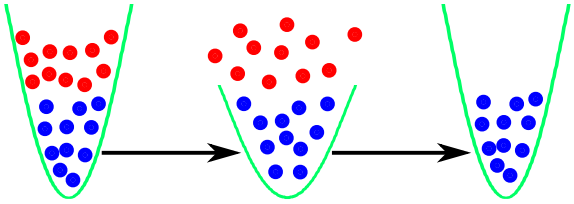

Figure 5.3: A cartoon demonstrating the three stages of an evaporative cooling. The red dots represent the trapped ions with $E > E'$ and the blue one $E < E'$. The green curves are the representation of trapping potential $C_2 U_0$.

ion creation in Penning traps (section 6.2), where the temperature of a fraction of the created ions is higher than the deepest trapping potential. Another example of such cooling happens during mass spectra measurement, in cases where the temperature of particles exceed the

trapping voltage while ramping the voltage (section 6.1). Also, a common application is to combine evaporative cooling with radio frequency excitations for charge state selection, known as the SWIFT (section 6.3).

5.2.3 Resistive Cooling of Ion Clouds

The resistive cooling has an important role at the current situation at ARTEMIS. Hence, a detailed review of three main cases at ARTEMIS is studied; (1) resistive cooling of a single particle (2) ion ensemble with in-phase (3) random phase oscillations. Afterwards, the energy transfer model that is considered for resistive cooling in case such as ARTEMIS is discussed. Finally, the study of the effective trap distance D considering a trapped ion ensemble is presented. In case of ion clouds with considerable number of particles, it is required to recalculate D. Since, an large enough ion ensemble can no longer be treated as point-like particle in the center of the trap and the spatial distribution of it should be considered.

5.2.3.1 Resistive Cooling of a Single Particle

Resistive cooling is based on the image current interaction (eq. 3.2) with the detection system. The formalism for this behavior is similar for axial ω_z and radial $\omega_\pm$ motions, for convenience the latter is discussed in detail. The RLC-circuit is kept at liquid helium temperature. Thereafter, the ion motion leads to a power dissipation $P = R_P {I_P}^2$, with R_P and I_P being the resonance circuit effective resistance and the induced image current, respectively [52]. For resistive cooling of a single particle, assuming a frictional loss model, in a few steps it can be shown that the ion cooling has an exponential loss behavior, $E_z = E_z(t = 0)\exp(-\gamma t)$. The γ is the energy damping constant in such a system, which translates to a cooling time constant as

$$\tau_z = \gamma^{-1} = \frac{D^2}{R_P}\frac{m}{q^2}, \tag{5.7}$$

with D being the effective trap size. Furthermore, this cooling model only holds true for the cases that the $\gamma \ll \omega$. The single-ion cooling has been measured in agreement with equation 5.7 in [43].

5.2.3.2 Extension to Ion Ensembles

In general the resistive cooling of ion ensembles follows the same principles of single particle cooling but further considerations are required. Since the number of particles is larger and ion-ion interaction plays an important role, a more complex simulative method is necessary as described in references [19, 115, 116]. The induced current of $I_N(t)$ for N identical particles

with independent movement and same phase which are in resonance with the cooling RLC-circuit is

$$I_N^2(t) = N^2 I_p(t) = N^2 \frac{m}{q^2} \frac{D^2}{R_P} E_z(t). \tag{5.8}$$

which the dissipated power can be written as

$$P_N = N R_P I_N^2(t) = \frac{dN E_z}{dt}, \tag{5.9}$$

where it is obvious that the energy dissipation follows an exponential decay

$$E(t) = E(t=0) e^{-t/\tau}, \tag{5.10}$$

with $E(t=0)$ being the initial ion ensemble energy after creation or transport to the Penning trap and τ is the cooling time constant. Finally, the cooling time constant for N particles oscillating axially in phase reads as [11]

$$\tau_N = \frac{1}{N} \frac{m}{R_P} \frac{D^2}{q^2} = \frac{1}{N} \tau_z. \tag{5.11}$$

The similarity between the cooling time constant of a single particle and an ion ensemble is obvious here and the only difference is that the ion cloud cools N times faster than a single confined particle. The final temperature of the ion is determined by the noise of the electronics (often the Johnson noise having the main contribution), creating a root mean square (RMS) voltage across the resistor R_P of the RLC-circuit as (section 5.1.1)

$$U_T^2 = 4 k_B T R_P \Delta\omega, \tag{5.12}$$

here T is the detection systems temperature and $\Delta\omega$ is the width of the ion signal spectrum.

Finally, in the case that the particles are moving with arbitrary phases, the time-averaged mean square value of the induced current due to all N particles have to be taken into account. According to [117]

$$\left\langle I_N^2(t) \right\rangle = \sum_{k=1}^{N} \left\langle I_k^2(t) \right\rangle + \sum_{k,l \ \& \ k \neq l}^{N} \left\langle I_k(t) I_l(t) \right\rangle, \tag{5.13}$$

only the first term of this summation is non-zero and equal to [117]

$$\left\langle I_N^2(t) \right\rangle = \frac{q^2}{m} \frac{\langle N E(t) \rangle}{D^2} = N \left\langle I^2(t) \right\rangle. \tag{5.14}$$

Finally, this term is translated to

$$\frac{\langle NE \rangle}{dt} = -\langle P(t) \rangle = -N \left\langle I^2(t) \right\rangle R. \tag{5.15}$$

$$\tau_N = \frac{m}{q^2} \frac{D^2}{R_P}, \tag{5.16}$$

since τ_N is similar to what is calculated for a single charged particle. It can be concluded that for an ion ensemble of N particles oscillating with random phases, the cooling is equivalent to the cooling of a particle with mass Nm and charge Nq. Therefore, giving rise to the idea that cooling an ensemble of ions can be treated as cooling the center-of-charge of that cloud [117]. Due to Newton's third law, the center-of-charge motion of an ion cloud is immune to ion-ion interactions and therefore the cooling of ion ensemble should not vary [65]. Nevertheless, due to high energies after creation in the CT of ARTEMIS and unresolved imperfection at this stage of the experiment, internal coupling of different degrees of freedom is not negligible.

The same approach is valid for the radial degrees of freedom leading to the same exponential energy decay, where for ω_+ and ω_z the dissipation of energy translates to reduction of the motion amplitude, for the magnetron motion ω_- the response is opposite. Hence 'magnetron cooling' (a term commonly used instead of magnetron centering) is achieved through coupling this degree of freedom with one of the other ion motions by radiation of a signal with sum of the ω_- and ω_+ or ω_z [118].

5.2.3.3 Energy Transfer Model for Resistive Cooling

This model presented in reference [108] is based on considering two assumptions: First confined particles obtain considerably high kinetic energy and second the direct cooling is only done on the axial center-of-charge motion.

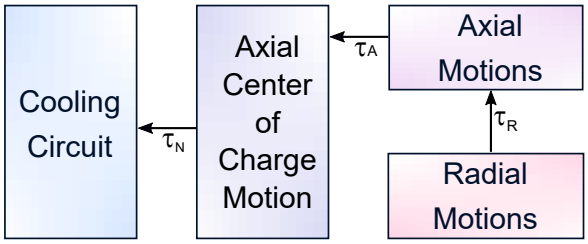

Figure 5.4: Energy transfer model for resistive cooling through the axial motion cooling of an extremely hot thermalised ion cloud.

In this model and in the presence of field imperfections, the axial energy of individual confined particles are translated into an effective axial center-of-charge motion energy, where the center-of-charge temperature in turn dissipates through the cooling circuit. Although the radial motion is not directly cooled, the energy of this motion is transfered to the axial energy, hence it is transfered to the thermal bath via the energy chain. Three different time constants are expected to be present in such a model: the center-of-charge cooling time constant τ_N,

axial motion time constant τ_A and the radial cooling time constant τ_R. Figure 5.4 shows a diagram of this model with the relevant time constants.

The observability of this cooling procedure highly depends on the energy levels of each motion. Considering a thermalised ensemble of ions with a considerable number of particles $N \gg 1$ the ratio each degree of freedom verses the total energy E of the system reads as

$$\frac{E_{cc}^{(z)}}{E} = \frac{1}{3N} \ll 1 \qquad \text{axial centre-of-charge motion} \qquad (5.17)$$

$$\frac{E^{(z)}}{E} = \frac{N-1}{N} \approx \frac{1}{3} \qquad \text{relative axial motions} \qquad (5.18)$$

$$\frac{E^{(R)}}{E} = \frac{2N}{3N} = \frac{2}{3} \qquad \text{radial motions.} \qquad (5.19)$$

As a first conclusion, the hierarchy of the cooling time constants can be easily observed from these equations $\tau_N < \tau_A < \tau_R$. Since the first ratio is typically very small for such a system observation of the center-of-charge energy is hardly possible and the relative time constant is too fast to be resolved [108]. The cooling procedures and their corresponding energy flows happen simultaneously and with time constants close to each other, thus only a superposition of all cooling procedures will be observable.

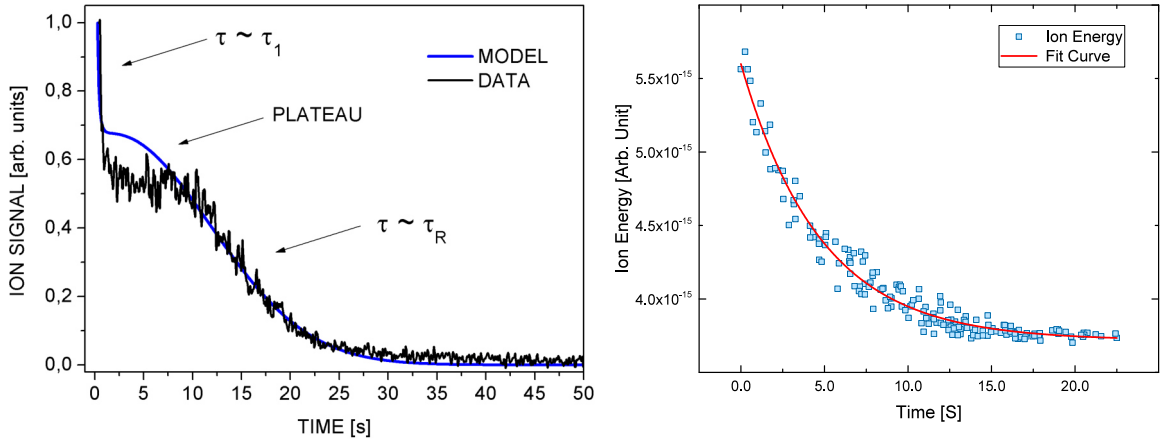

Figure 5.5: Comparison of cooling curves for two different ion ensembles at different trapping potential situation. The left curve is taken from reference [108] and it represents a cooling procure of limited particle number ion cloud at near perfect trapping potential. Whereas the one on the right is for a highly populated ion cloud measured at the CT of ARTEMIS with non-harmonized trapping potential.

Nonetheless, in general two main cooling behaviors could be expected: a fast thermalisation with exponential decay and a slow thermalisation with non-exponential cooling. Fast exponential cooling behavior is normally observed when a considerable number of particles are stored (more than 10^3) and field imperfections are strong enough to lead to strong interactions between the particles different degrees of freedom [65]. On the contrary when a non-exponential slow cooling is observed the number of particles are limited (e.g. 30 in reference [108]) and moreover the trap's potential is optimized to high levels of harmonicity.

In this fashion field-initiated cooling effects are not strong enough to accelerate the cooling procedure.

Figure 5.5 shows a side-by-side comparison of the two discussed cooling behaviors. The cooling curve demonstrated on the left side is from [108] and demonstrate the case that a low number of particles are confined in a nearly ideal Penning trap. The second curve is obtained from the trapped particles in the CT of ARTEMIS and will be discussed in further detail in chapter 6.

5.2.3.4 Effective Electrode Distance Calculation for the Creation Trap

An important parameter characterizing the resistive cooling in Penning traps is the effective electrode distance, which encloses the geometrical specification of the trap electrodes involved in the cooling procedure. In order to simplify the related calculation, the effective electrode distance D has been first introduced in [67] and ever since it has been used in a variety of works [21, 18] to calculate the cooling time constant τ_z as formulated in equations of section 5.2.3.

Using the surface charge density $Q_i(r,z)$ induced by a charged particle q on the surface of a Penning trap electrode and utilizing the radial r and axial z positions of the charge in the trap, D can be calculated [19]. In order to do so $Q_i(r,z)$ is written in terms of a geometry function $\Xi(r,z)$ as follows

$$Q_i(r,z) = -q \cdot \Xi(r,z) \tag{5.20}$$

where $\Xi(r,z)$ reads,

$$\Xi(r,z) = \frac{-1}{\rho_0 \pi} \int_0^\infty \frac{\mathrm{I}_0\,(xr/\rho_0)}{\mathrm{I}_0\,(x)} \left[\mathrm{sinc}(x\frac{z-z_F}{\pi R})(z-z_F) - \mathrm{sinc}(x\frac{z-z_N}{\pi R})(z-z_N) \right] dx. \tag{5.21}$$

Here ρ_0 is the electrode's inner radius at the CT, z_N and z_F are the distance of the center of the trap to the nearest and farthest edge of the pick-up electrode, where $\mathrm{I}_0(x)$ is given by a modified Bessel function of the first kind; its appearance in the denominator of the integral makes further analytic calculation challenging and to this end numerical approaches are preferred.

Taking into account that the ions are stored at C14 ring electrode and the signal is picked up at C13, by applying the values $\rho_0 = 8.704\,\mathrm{mm}$, $z_N = 7.459\,\mathrm{mm}$ and $z_F = 21.571\,\mathrm{mm}$ for the CT of ARTEMIS, the Ξ-function was calculated for a limited number of radial and axial positions of a charged particle using WOLFRAM MATHEMATICA. Figure 5.7.a shows the result of these calculations. To extend this calculation to a more realistic situation at ARTEMIS,

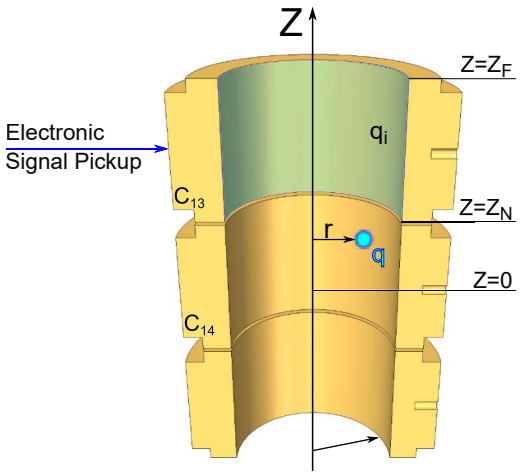

Figure 5.6: Depiction of the geometrical parameters, of the CT of ARTEMIS, used for calculation of the effective electrode distance D, including the induced charge q_i on the pick-up electrode.

where instead of one charged particle an ion cloud is normally confined and the ion cloud spreads out in space to a considerable distance from the center of trap, the number of radial and axial positions were extended to approximately 800 points each, resulting in 6×10^5 values calculated for Ξ. Figure 5.7.b demonstrates the resulting plot of these calculations. The data points between the limits are smoothened out for presentation, since in reality they also look like overlapping data points due to their high number.

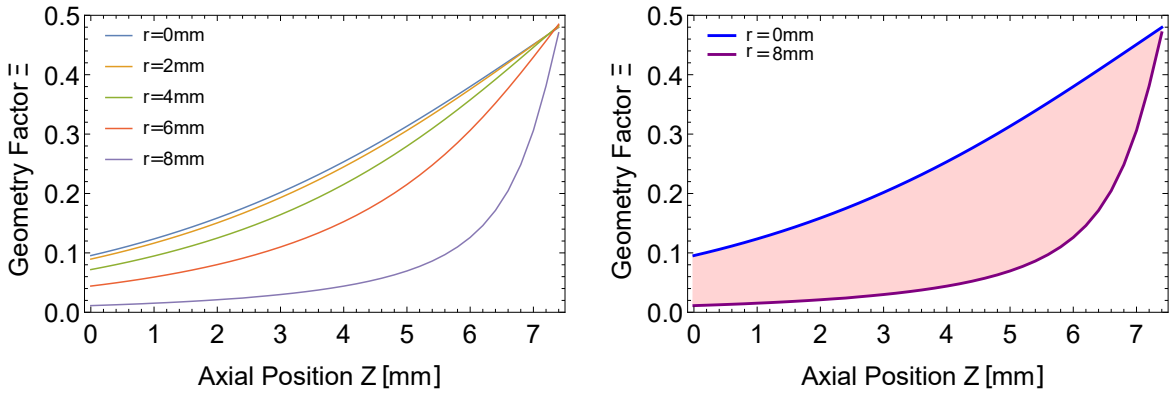

Figure 5.7: The calculations of the geometrical parameter Ξ at ARTEMIS, (a) For 5 different radial and approximately 100 axial positions. (b) Approximately 800 different radial and axial positions each, resulting in 6×10^5 numerical results for Ξ.

As the next step from comparing equations 3.2 and 5.20 it is clear that

$$\partial_z \Xi(r, z) = D^{-1}. \tag{5.22}$$

Therefore, applying a similar numerical calculation scheme for the values of D for the same number of different r and z coordinates, combinations are calculated as depicted in figure 5.8; for limited numbers in sub-figure (a) and the extended version in the sub-figure (b).

Finally to calculate one $D(r, z)$ over the total confinement volume, the RMS of all the D

values have been calculated across axial and radial dimensions. In this fashion the effective electrode distance for an ion cloud located at the center of the electrode C14 which is spread out over a non-negligible distance from the center of trap is calculated. The RMS value of D at the CT of ARTEMIS in this fashion is calculated to be equal to $43.47\,\mathrm{mm}$.

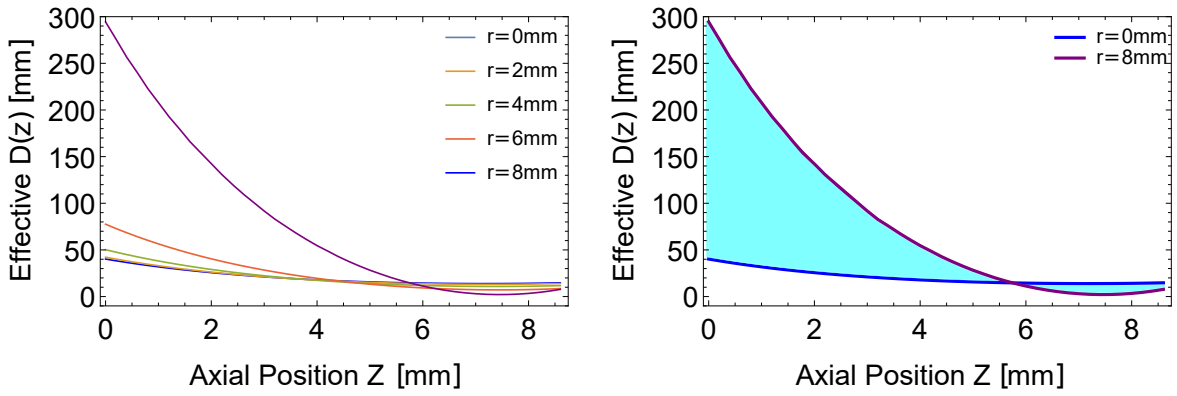

Figure 5.8: The calculations of the effective electrode distance for the CT. (a) For limited number of radial an axial coordinates, 5 radial and approximately 100 axial positions. (b) D calculation of 800 axial and 800 radial positions resulting in 6×10^5 numerical results for D.

5.2.3.5 Spectral Overlap between RLC-Circuit and Particle Oscillation

An important parameter in characterizing the resistive cooling of an ion is the spectral overlap of the particle oscillation and RLC-circuit. The width of the particle motion has several origins (most importantly the field imperfections) and in the case of the RLC-circuit its finite Q-value defines the width of it. Since the resistive cooling is effective only within the bandwidth of the RLC-circuit, to achieve the highest efficiency of a resistive cooling process a maximum overlap between the two frequency widths is required [15]. Figure 5.9 schematically shows such an overlap and the involved parameters. For the axial ion motion of a particle with center frequency of ω_z, a spectral width of δ is introduced in this model. Furthermore, according to equation 3.3, the spectral width of the resonator circuit reads as $\Delta\omega = \omega_R/Q$, here ω_R is the resonance frequency of the detection circuit with the impedance of $R(\omega = \omega_R) = R_P$.

For a large and/or hot ion ensemble—as in the case of the ion cloud in ARTEMIS—the axial frequency distribution of the ions is much broader than the one from the detection circuit $\delta \gg \Delta\omega$. As a result, only the fraction of the ion cloud that is interacting with the resonance circuit is being resistively cooled and the rest of the ion cloud is only cooled via the sympathetic cooling process. In order for the ion ensemble to be efficiently cooled by the resistive cooling, it is required to have fast enough thermalisation between the ions [15].

In case of ion cooling through mass spectra acquisition (chapter 6), the spectral overlap of the ion axial oscillation and the RLC-circuit is a variable as a function of the ramp voltage.

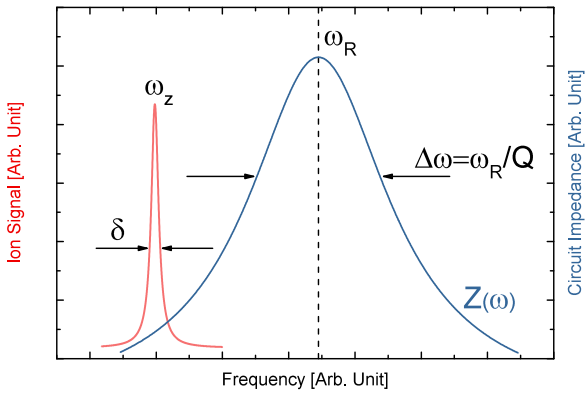

Figure 5.9: Schematic overlap of the spectral distribution of the particle oscillation and the RLC-Circuit spectrum. The highest resistive cooling takes place at $\omega_z = \omega_R$ and $\delta \approx \Delta\omega$.

As a result, the fraction of the ion cloud being resistively cooled is evolving through the procedure, which leads to a difference in the cooling time constant and the acquisition time (section 6.7).

5.2.3.6 Spectral Evolution of Resistive Cooling of the Axial Motion

The spectral line shape evolution of the axial ion signal of each individual species due to resistive cooling as a function of time, is characterized by the time derivative of three main parameters: the energy of the ion cloud E, the center frequency ω_z and the width of the ion signal of that species spectrum δ_ω. Figure 5.10 shows an expected spectral evolution during an axial resistive cooling of a pure ion ensemble (left) and the parameters involved (right), schematically.

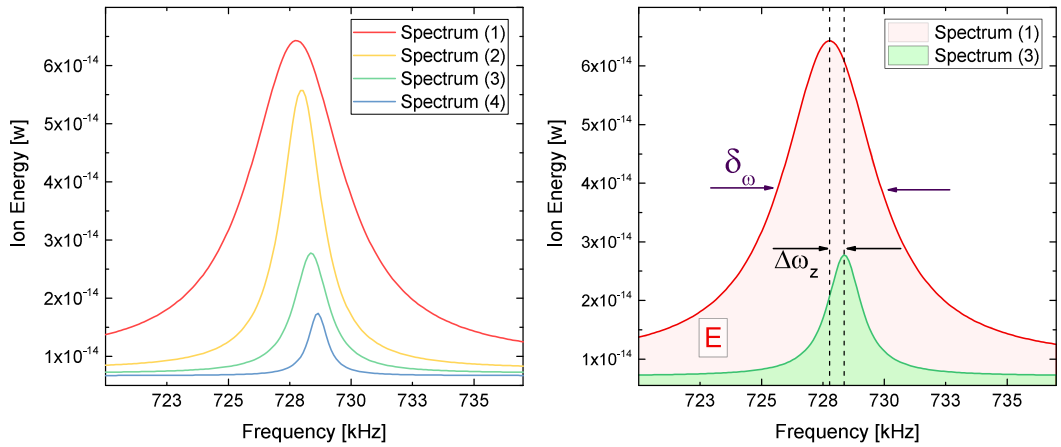

Figure 5.10: Schematic spectral line shape evolution of the ion ensemble signal as a result of resistive cooling and the parameters involved. The area under curve represents the ensemble energy E, the width of the spectrum is depicted as δ_ω and the change of the center frequency of the spectra is shown as $\Delta\omega_z$

Considering an ion ensemble at a thermal equilibrium and as long as ion loss is negligible, in energy space the area under each peak is proportional to ensemble energy and hence to the ensemble temperature. This description is equivalently valid in the frequency space. Considering a Boltzmann distribution (section 5.1), the peak has its expected maximum at

position proportional to ion numbers N and $(1/2)k_BT$. Therefore, its position in the energy spectrum is also proportional to the temperature, whereas the width has a linear and possible higher-order contributions of the temperature [15]. As a result, the time evolution of the peak area and thus the temperature (with decay time constant τ_T) of the ensemble under resistive cooling demonstrates an exponential decay. The peak position should follow the same behavior, ideally with the same time constant as the decay time constant for temperature $\tau_{\omega_z} = \tau_T$. The observed decay time constant of the signal width $\tau_{\delta\omega}$ may be different from τ_T, if the higher-order contributions are significant. This is expected in particular for strong trapping field imperfections and for high ensemble temperatures. Figure 5.11 shows these changes schematically for two temperatures of an ion ensemble $T_2 < T_1$.

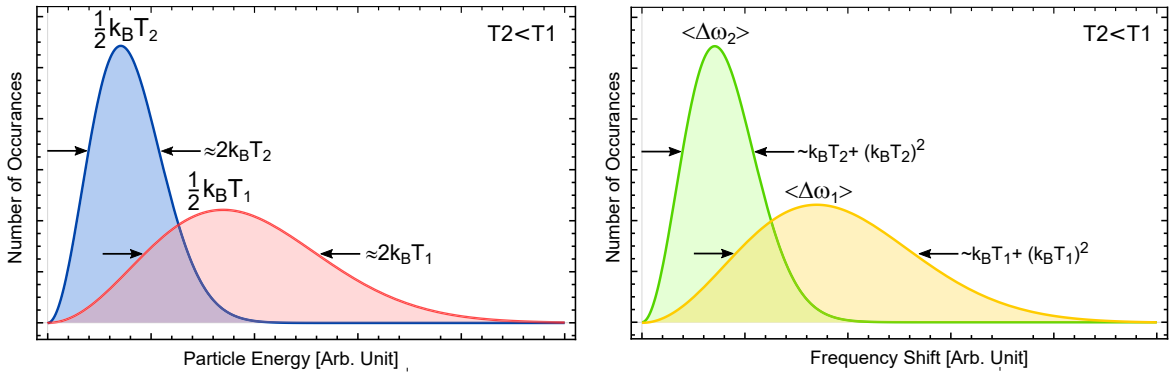

Figure 5.11: Schematic display of Boltzmann distribution of energy (left) and Frequency shift (right) for the stored particles and their changes as a result of the resistive cooling.

Currently, at ARTEMIS the measured quantity is a spectral power density (measured in zero-span mode) as a function of trap voltage, a so-called mass spectrum (section 6.1). The area under such a peak is an energy measure with an unknown scaling, hence for exact energy evaluation it is required to transform the voltage span of a given peak into the frequency span. According to equation 2.15, for a peak of interest, the frequency of the peak is proportional to the square root of the measured trapping voltage C_2U_0. In this fashion, a transformation from the frequency space to voltage space is made. Therefore, the cooling behavior as function of time in the voltage space is proportional to the square of the time derivative of the temperature of the ion ensemble. The spectral width time evolution in voltage space is again dependent on the higher-order temperature contributions, thus the decay time constant of it is subject of change according to the trapping field imperfections and the ion ensemble temperatures.

5.2.4 Sympathetic Cooling

Benefiting from the mutual Coulomb interaction of trapped particles, cooling a fraction of the confined ions via another fraction is normally referred to as sympathetic cooling. In this case it is required to simultaneously trap both ions species in one trap or establish a strong

enough link between the two (or more) trapped ion species via their image current[108]. An approximation of the cooling time constant with a full spatial overlap of the particles is depicted as

$$\tau_T \approx (4\pi\varepsilon_0)^2 \frac{m_1 m_2}{q_1^2 q_2^2} \frac{1}{n_2 \ln\Lambda} \left(\frac{k_B T_1}{m_1} \frac{k_B T_2}{m_2} \right)^{3/2}, \tag{5.23}$$

here the qualities with index '1' are the ones being cooled by another procedure and the ones with index '2' are cooled via sympathetic interactions. The quantity $\ln\Lambda$ is known as the Coulomb logarithm and reads as [119]

$$\ln\Lambda \approx 23 - \ln \left[\frac{q_1 q_2 [\mu_1 + \mu_2]}{e^2(\mu_1 T_1 + \mu_2 T_2)} \left(\frac{n_1 q_1^2}{e^2 T_1} + \frac{n_2 q_2^2}{e^2 T_2} \right)^{1/2} \right]. \tag{5.24}$$

Please keep in mind, that the n should be expressed in units of cm^{-3} and temperature in units of eV. In general for several different coolants the temperature evolves as

$$\frac{\partial T_1}{\partial t} = \sum_a \frac{1}{\tau^{(a)}} (T_a - T_1) \tag{5.25}$$

The sympathetic cooling has two important applications in ARTEMIS. Firstly, when a variety of charge states of HCI is created and stored in the CT, by cooling one charged state resistively other charge states also will cool via a sympathetic interaction. The lower limit of the sympathetic cooling time constant has been estimated to be $\tau_T \approx 6.7\,\mu\mathrm{s}$ [120]. Secondly, a sympathetic laser cooling scheme is to be add to the setup in future, for example using beryllium ions, which will benefit from the same principle (appendix B).

CHAPTER

SIX

STUDIES OF ION ENSEMBLE PREPARATION AND ION CLOUD RESISTIVE COOLING

Characterization of the ion cloud created in the creation trap (CT) and its behavior in both of the traps of ARTEMIS at HITRAP, are evolutionary steps that should be pursued in order to reach the milestone of ARTEMIS —double resonance spectroscopy of highly charged ions. Ion creation parameters, ion transport from the CT to the spectroscopy trap (ST), residual gas pressure estimation, ion ensemble temperature readout, and resistive cooling of the ion ensemble in the CT are the aspects that have been studied in this project and the results obtained are discussed in this chapter. These results are based on the measurement performed in the end of 2016 and the beginning of 2017 measurement campaigns. For the sense of completion it is required to consider the results published in the two preceding reports by D. von Lindenfels [20] and M. Wiesel [21].

6.1 Mass Spectra Read-out

An alternative interpretation of the measurement technique introduced in section 3.1 is a charge-to-mass ramp (q/m ramp) or mass spectrum data acquisition. The underlying concept of image charge measurement still holds in this approach. In comparison to direct frequency space measurements, where the trapping potential is tuned to a certain value C_2U_0, considering the fixed resonance frequency of the RLC detection system, by gradually sweeping the trapping voltage, different charge states come into resonance with the RLC detection system, hence increasing the amplitude of the resonance spectrum acquired from the resonator. In this fashion a mass spectrum of the ion signal versus the trap voltage is obtained. Typically, for such readouts a zero span mode of the FFT spectrum analyzer is utilized. In such spectra, the relation between ion frequency and trapping voltage can be obtained using $\omega_z^2 = C_2 q U_0 / m d^2$

(section 2.15).

Figure 6.1 shows a typical acquired spectrum in the CT of ARTEMIS, with the ARES CT resonator with resonance frequency of $2\pi \times 737.5\,\mathrm{kHz}$ and a voltage sweep step corresponding to frequency steps of $300\,\mathrm{Hz}$. The Ar^{13+} ion species signal, considering the typical frequency shifts in Penning traps (Section 2.4), is observable at $54.87\,\mathrm{V}$.

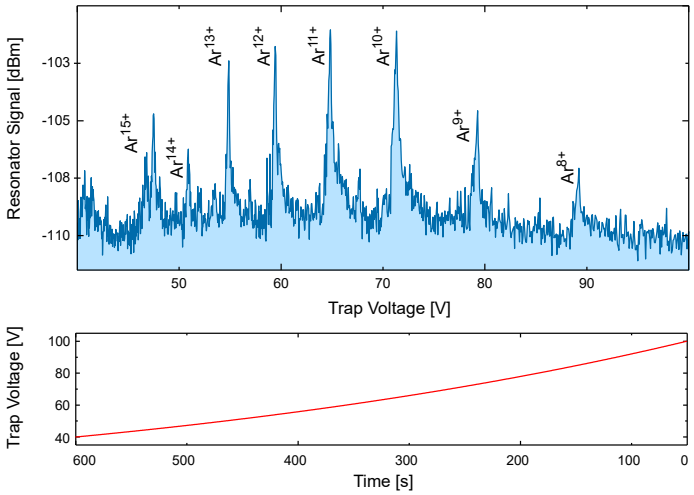

Figure 6.1: Typical mass spectrum acquired with the ARES CT from the ion cloud stored at the CT of ARTEMIS. The lower plot shows the time evolution of the trap voltage from 40 V to 100 V, which is the typical range in which argon charge states are observable with the resonance frequency of the current ARES CT.

There are three main features of such an ion signal readout technique that should be emphasized: (1) these spectra can be used to make a clear distinction of different charge-to-mass ratios, hence making it a strong tool for determining the nature of trapped particles; (2) once an ion species comes into resonance with the RLC-circuit it results in cooling of the ions resistively, as a result the signal height of the two consecutive ramps will differ until the ion cloud is totally in thermal equilibrium with its respective detection system; (3) the area under the curve is a convolution of the ion number and the ion energy. Despite the ease of use and the benefits of this readout technique, the effort to switch to measurements of frequency spectra have already been started. The overlapping ion signal of each charge state in a multi-charge-state ion cloud makes it challenging to use a measurement in the frequency domain, hence also in the future the mass-spectra readout method will be still used extensively.

6.2 Highly-Charged-Ion Creation in the Creation Trap

Until ARTEMIS is connected to the HITRAP beam-line—giving it access to the HCI created at the GSI facility or the commercial EBIT of the HITRAP beam-line—further investigation and optimization of the creation procedure done in the CT of ARTEMIS is required. It should be noted that after each warm-up and cool-down performed for upgrading ARTEMIS the creation parameters involved are modified, hence introducing yet another reason for recalibrating the creation procedure at the beginning of each measurement campaign. Furthermore, some

new ideas have been tested in order to optimize the creation in comparison to the measurement campaigns in 2015[20] and 2016[21].

The creation procedure is reported in extensive detail in [20, 21]. The creation at the CT is based on electron-impact ionization and can be summarized into four stages as follows:

Trapping Electrons:

The electrons are created using a field-emission point (FEP). A negative high voltage V_{FEP} is applied to a needle-shaped tungsten rod, resulting in field emission. Using the so-called accelerator electrode, which has positive potential V_{acc}, the electrons are extracted and directed into the CT. There the strong magnetic field of the trap radially confines the electrons and using the high voltage electrodes—H8/H9 and H19 (figure 2.7)—the electrons are confined axially.

The kinetic energy of the electrons is defined by the V_{FEP} and the electron-current density is defined by the $V_{\text{FEP}} - V_{\text{acc}}$. At ARTEMIS these high-voltages are applied by HV-FEP power supply by Stahl-Electronics, a device capable of delivering up to $\pm 3\,\text{kV}$. Furthermore, this device is capable of manual measurement of the current flowing through the FEP. Since the tip is a collection of microscopic tip structures and subject to possible changes (through time or temperature fluctuations), the overall current of the FEP can vary strongly [20]. Thus, it is required to recalibrate it on a regular basis. Figure 6.2 shows the calibration curves of the FEP current for different V_{FEP} and V_{acc} in two consecutive measurement campaigns.

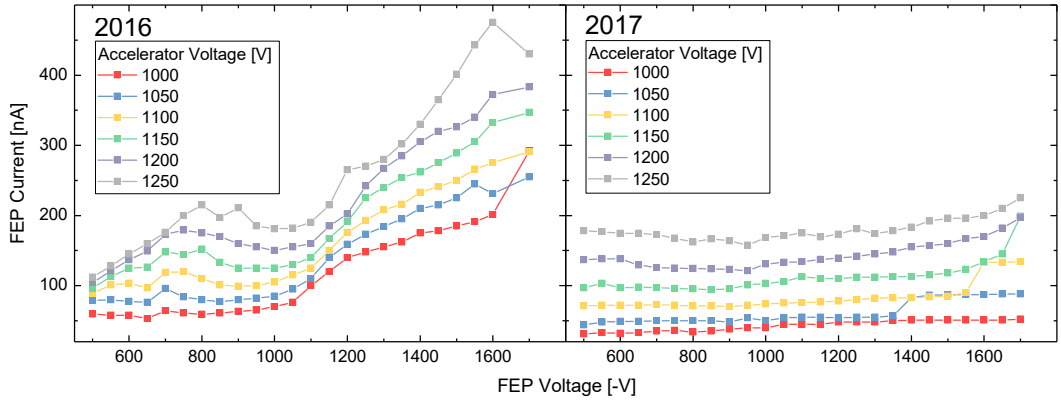

Figure 6.2: A comparison between the FEP currents at the CT as a function of V_{FEP} and V_{acc} in 2016 and 2017. The sharp decrease of the current can be associated to the deformation of the FEP or the changes in the HV-filter board.

The reduced current observed in 2017, may be the result of deformation of the FEP or the changes of the HV-filter board described in section 4.3. Further inspections, when the setup is opened for the next upgrades, are required to clarify this decrease.

Gas Injection:

The gas injection is done through the gas injection system described in section 4.5. As already mentioned the pressure is set in this system to about $0.6\,\mathrm{mbar}$. After the electrons have been emitted and as they are still oscillating in the CT, the path of the gas to the CT is opened using a pressurised-air valve and heating the cryo-valve. For optimization of the creation procedure the pressure of this section also needs to be adjusted in every measurement campaign. It also should be mentioned, that the gas injection is essential only for a limited number of initial creations. Since, after a number of creations the fraction of gas which has not been ionized normally freezes on the cryo-valve and the inner walls of the trap electrode. Thus, the later creations can be successfully carried out without injecting new atoms into the system and only through sputtering of the frozen atoms.

Charge Breeding and Ion formation:

Using the high voltage electrodes at the two ends of the CT the electrons are reflected back-and-forth resulting in ionization of the argon atoms, this procedure is typically known as charge-breeding capable of delivering higher charge state ions. The convolution of charge breeding-time and the electron-current density influences the charge state of the created HCI. By controlling the breeding-time via ARTEMIS's control program [1] and the absolute voltage value applied between the accelerator electrode and the FEP, the charge states created in the CT are controlled.

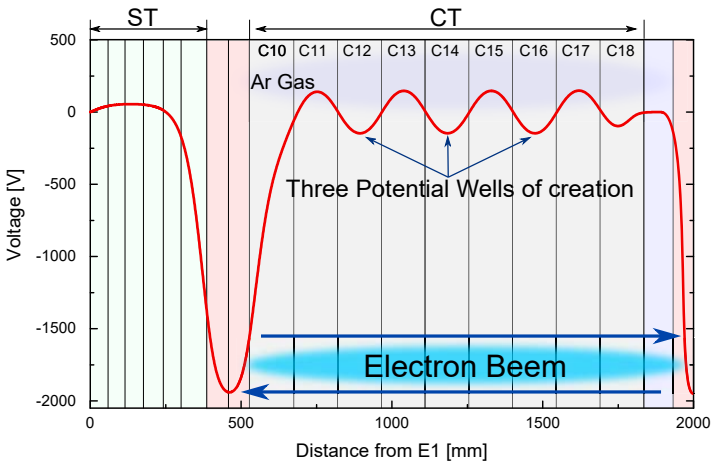

Figure 6.3: Ion creation trap configuration for the high voltage and trapping electrodes at the CT. The potentials depicted in this figure are simulated using the program SIMION and afterwards the other involved parts are added schematically to the figure.

Simultaneously, the electrodes of the CT trap are set to form three potential wells of creation (figure 6.3). As soon as the argon atoms and the stored electrons collide, charged argon ions are created and trapped. For creating Ar^{13+} an electron beam with energy of approximately $0.7\,\mathrm{keV}$ is required [20], although the actual energy of the electrons emitted from the

[1] A LABVIEW-based program for controlling ARTEMIS and its laser system. Also, software integration into the HITRAP beam-line in future will be done through this control program.

FEP is not easily drivable from the voltages applied [121]. Anyhow, looking at typical mass spectra of the ion clouds after creation at ARTEMIS, the energy requirement is easily fulfilled (even higher to create Ar^{16+}). The effects of different electron energies and breeding-times in ARTEMIS have been already studied and reported [17, 21].

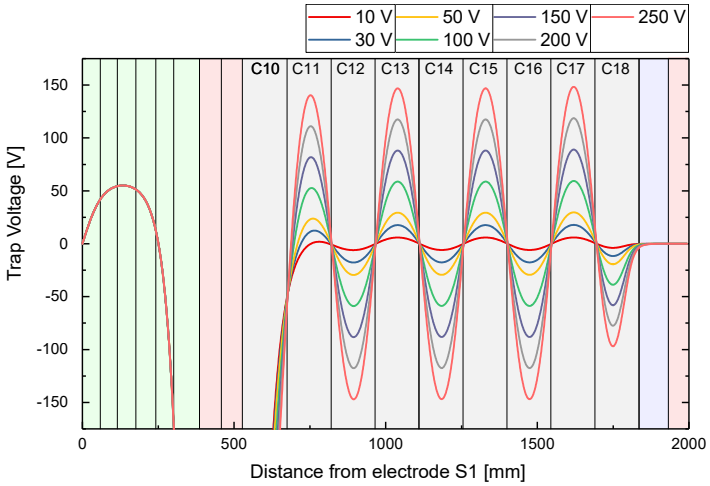

Figure 6.4: SIMION simulation of seven different potential wells of creation used for studying the effect of different potential wells on the yield of the creation procedure.

Another important parameter involved in the creation of HCI yield is the depth of the three potential wells of creation, since the alternating CT potential modifies the energy of the ions, especially when the ion ensemble is newly created and has high temperatures and is not confined in the minima of the trapping potential. It can be shown using equation 5.6, that the ion evaporation rate increases for shallower creation traps, leading to weaker confinement of the newly created ions.

Hence, by setting the depth of these wells to seven different values (figure 6.4) several combinations of five V_{FEP} and two V_{acc} and a breeding time of $5\,\mathrm{s}$ were used to study the ion creation. Figure 6.5 shows the total spectrum area after each creation (sub-figures (a) and (b)) and another mass spectrum obtained immediately after the first one (sub-figures (c) and (d)). The plots on the left side are the result of the creations with $V_{\mathrm{acc}} = +1250\,\mathrm{V}$ and the plots on the right are after creations with $V_{\mathrm{acc}} = +1200\,\mathrm{V}$. The legends in the plots show the value of V_{FEP} used in the respective creation.

The general trend observed in these curves is that by increasing the depth of the creation traps the total area under the spectrum increases, which can be associated to the fact that ions with higher energies are also trapped and have not escaped the trap. For certain values of the trapping potential in the second mass spectra it is clear that almost the same area under the spectrum is achieved; for creation with $V_{\mathrm{acc}} = +1250\,\mathrm{V}$ at $300\,\mathrm{V}$ and for $V_{\mathrm{acc}} = +1200\,\mathrm{V}$ at $250\,\mathrm{V}$. These values of trapping potential match the anticipated ion ensemble energies, since the ions created with a lower V_{acc} are expected to have a lower energy transferred to them by the electrons. An increase in the total area under the spectrum is observed when the creation is carried out at a voltage of $200\,\mathrm{V}$ and the total voltage between the accelerator electrode and

FEP is set as $2.7\,\mathrm{kV} \leqslant V \leqslant 2.85\,\mathrm{kV}$, thus indicating that these values can be considered as an optimum creation condition for all involved parameters.

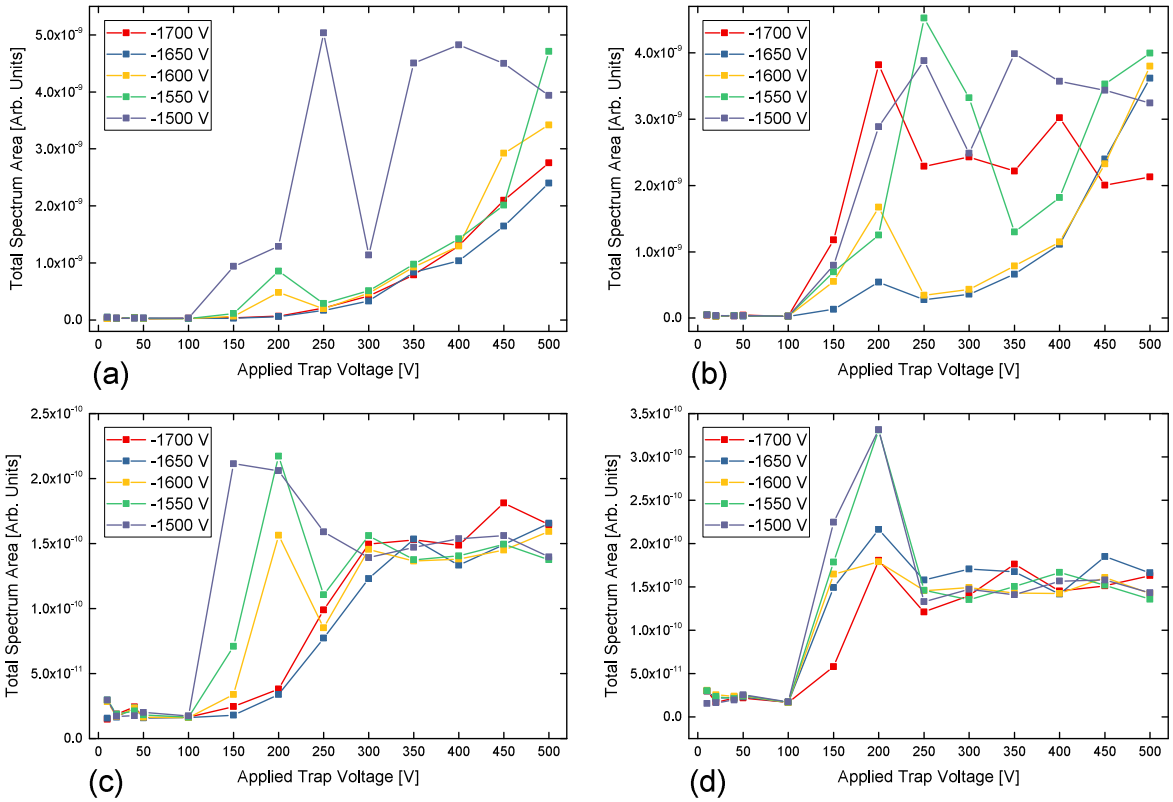

Figure 6.5: Comparison of the total spectrum area for seven different depths of creation traps shown in figure 6.4. Sub-figures (a) and (c) are the data evaluated after the first and second mass spectrum (respectively) acquired from the ion ensembles created with $V_{\mathrm{acc}} = +1250\,\mathrm{V}$. Whereas, Sub-figures (b) and (d) are similar measurements with $V_{\mathrm{acc}} = +1200\,\mathrm{V}$. The legends in the plots show the value of V_{FEP} used in the respective creation.

Ion Concentration and Emptying the Adjacent Traps:

This is the final stage of ion creation, which ensures that all the ions created in the CT are concentrated and confined in the central trap at C14 electrode. As reported in [21] this part of the procedure is required to eliminate unwanted image current induced on the electrodes, resulting in an interfering ion signal from the adjacent traps with the main ion signal from the trapped particles in the C14 trap.

Highly Charged Ions Stored in ARTEMIS

Creating ion clouds of various charge states of argon (Ar^{9+} to Ar^{16+}) is done routinely at ARTEMIS, a typical mass spectrum of such an ion ensemble is shown in figure 6.1. Nevertheless, if the accelerator voltage applied is high enough to make the FEP current emitted in orders of a few hundred nA, the FEP —which is made of tungsten—starts to disintegrate and

delivers tungsten into the CT Trap. A FEP voltage about $0.5\,\mathrm{kV}$ is enough to create W^{21+}.

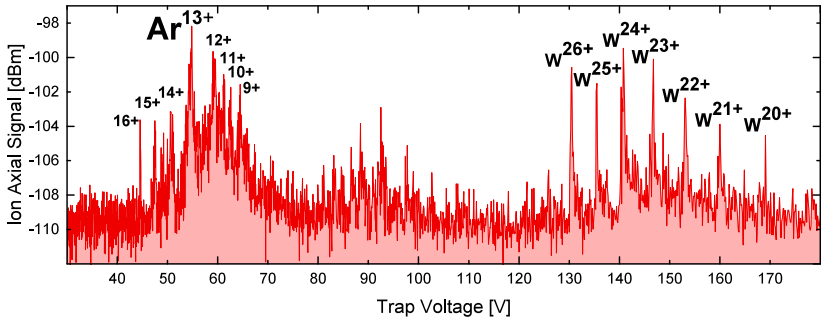

Figure 6.6: Highly charged ions stored in ARTEMIS, Ar and W. The argon charge states are created and stored as part of measurement routine at ARTEMIS. However, tungsten charge states are a result of high V_{acc} and disintegration of the FEP.

Figure 6.6 depicts a mass spectrum of the HCI stored in the CT of ARTEMIS after cooling the ion cloud. Besides the different charge states of argon, tungsten ions up to W^{26+} have been successfully stored in the trap. From this measurement it can be concluded, that heavier highly charged ions can be stored in ARTEMIS's trap. However, for preserving the FEP it is not recommended to recreate this mass spectrum.

6.3 Charge State Selection with SWIFT Technique

Generally, the ions resulting from in-trap production (or dynamic capture) include a variety of charge states. Hence, the **S**tored **W**aveform **I**nverse **F**ourier **T**ransform, or SWIFT, is a technique commonly used to remove the unwanted charge states in Penning traps, thus leaving the selected desired charge states confined in the trap. To 'clean' the trap[2], the axial motion (in some instances radial motion) is excited using a rf signal and the trapping potential is lowered in a manner that the excited ions leave the trap evaporatively. The SWIFT signal transient usually consists of the frequency band of all unwanted particles. This procedure using the available transmission lines connected to electrode C15, has been calculated and programmed into ARTEMIS's control system by M.Kiffer [120] and has been also reported in detail in [21]. Figure 6.7 shows a SWIFT procedure typically performed in several stages at ARTEMIS. The cycle of the SWIFT utilized at ARTEMIS is as follows:

- **SWIFT signal irradiation:** Since the ion cloud consists of a high number of particles and the low voltage filter board (Section 4.3) limits the power of the SWIFT signal to $10\,\mathrm{V}$ peak-to-peak, it is required to divide the excitation signal into several bandwidths each time corresponding to certain charge state(s). Therefore, the cleaning approach used at ARTEMIS can be rather described as a combination of rf resonant ejection and SWIFT technique. Currently, each excitation consists of 1000 bursts of the SWIFT signal with amplitude of $8\,\mathrm{V}$ peak-to-peak.

[2] An expression used for SWIFT in the community

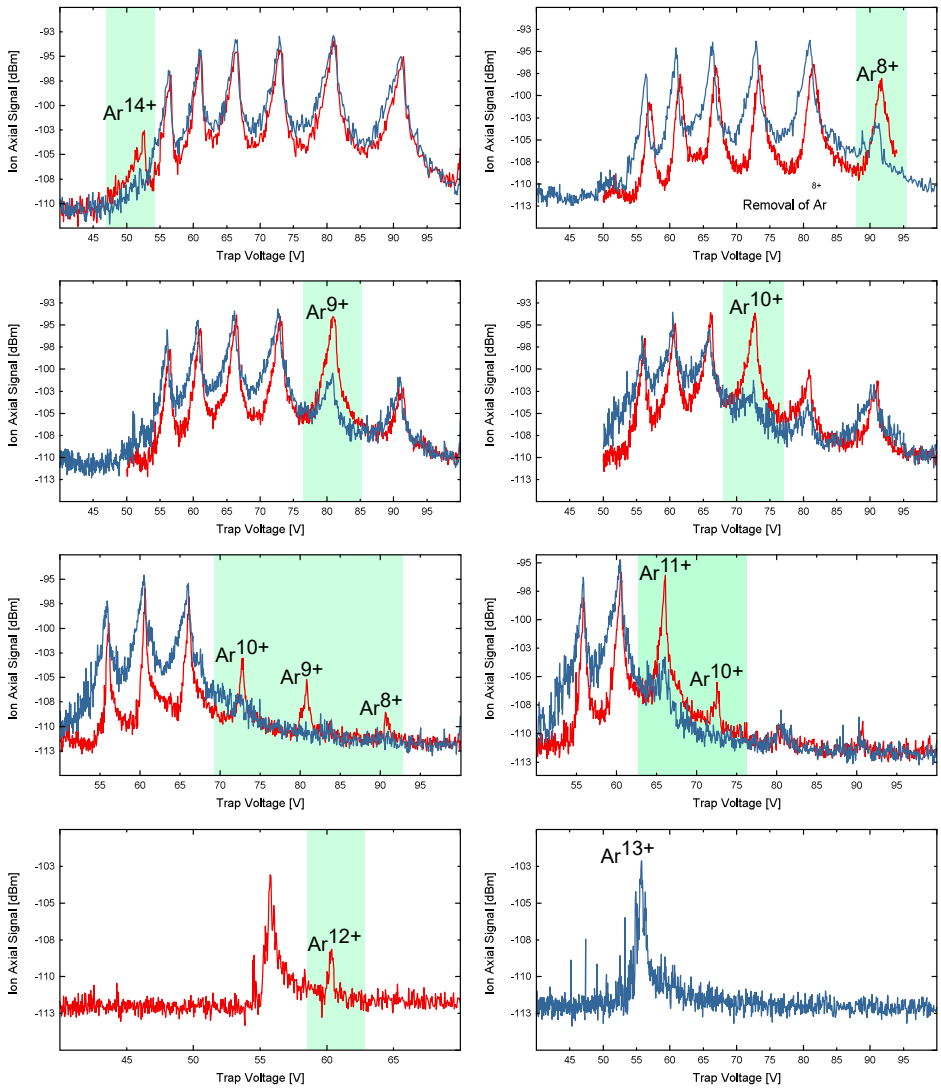

Figure 6.7: The charge selection done at ARTEMIS using the SWIFT technique. In comparison to many other experiments that apply SWIFT for cleaning the trap, at ARTEMIS the cleaning is done over several stages. A SWIFT excitation for specific charge is performed, afterwards a change of the trapping potential is done and then after rethermalisation of the ion ensemble the next charge state is removed.

- **Effective trapping potential modification:** As stated in section 5.2.4 a thermalisation time of roughly $\tau_T = 6.7\,\mathrm{ms}$ is expected in case of a typical ion cloud stored in ARTEMIS. This translates to the fact, that the lowering time of the effective trapping potential τ_S should be smaller than τ_T, hence a fast voltage switch with $\tau_S = 600\,\mu\mathrm{s}$ is used.

- **Rethermalisation and detection of the remaining charge state:** At this stage it is required to have a clear picture of what charge states have been successfully removed. Therefore, by acquiring a limited number (up to ten) of mass spectra the charge states that are still confined are identified and resistively cooled. Afterwards based on these last observed spectra, either the same charge state is excited and removed or the next desired charge state is cleaned from the trap.

The final ion ensemble left in the trap after a typical SWIFT procedure is about 10% of the size of the initial ion could. The three introduced stages are performed until the only confined charge state is Ar^{13+}. This procedure is considered to be long, in order of a day, hence modifications of the LV-filter boards and other electronics to be able to transmit higher powers of rf signal may be considered in the future.

6.4 Transport to Spectroscopy Trap

The next step after cleaning the ion cloud stored in the CT to pure Ar^{13+} is an adiabatic transport of the ion ensemble to the ST. The transport is realized by slow and consecutive manipulation of the potential of the neighboring electrode to the electrode that the ions are stored in it, starting from electrode C14 and ending at electrode S3. The transport is an essential part of the final experiment, since the double resonance laser-microwave spectroscopy is performed at electrode S3 of the ST. Since the direction of the transport matches the axial motion of the ions and considering the axial oscillation frequency of the ions (in order of a few hundred kHz), the response time of the filter boards (in order of few ms) guarantees the slow transport of trapped particles (figure 6.8).

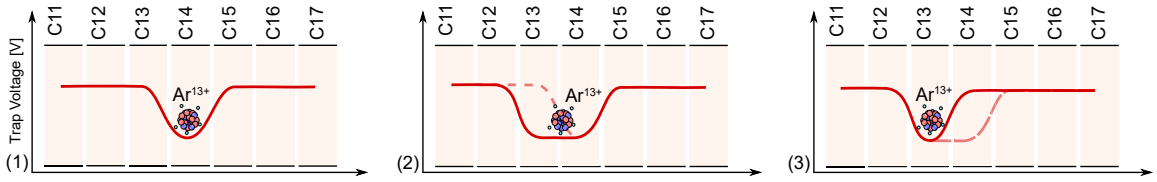

Figure 6.8: A cartoon showing the ion transport procedure from electrode C14 to the adjacent C13. The transport is preformed for one electrode to its neighboring until the ion cloud reaches the electrode S3 for the double resonance spectroscopy.

The transport of newly created ions from the electrode C14 to the electrode S3 has been successfully carried out in the measurement campaign of 2016. The spectrum of this transported ion cloud has been acquired using the toroidal superconducting resonator when it was still functional (section 3.2.7), figure 6.9 shows a typical spectrum of this measurement. Nevertheless, there are two issues to be considered. First prior to the transport, cooling and rf manipulation of the ion cloud is required, which with the transport procedure used in 2016 was not possible. Second, a back transport to the CT did not succeed, making the procedure irreversible. Anyhow observation of this spectrum had two important technical results; first confirmation that the toroidal superconducting detection system has worked —although for a short period of time. Second, the successful installation of the ITO-coated window regarding ion trapping in the ST (sections 3.7 and 2.3.1) [56].

After a close inspection of the components that are involved in the transport, it became clear that the high-voltage switch box responsible for selecting the voltage range (High- or low-

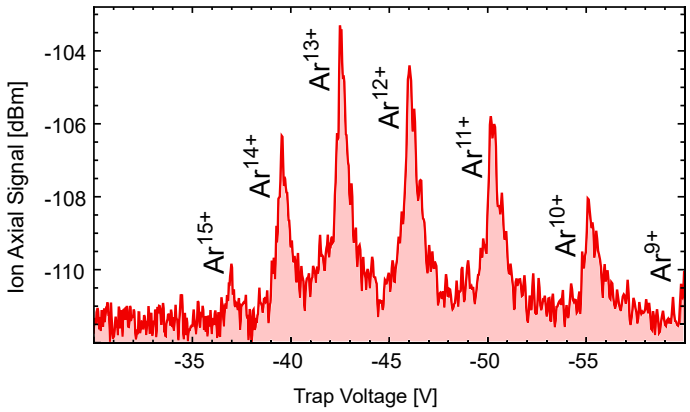

Figure 6.9: Spectrum of the ion ensemble measured in the ST after transport, where the transport is done directly after creation (2016). The ITO-coated window and the toroidal superconducting RLC detection system had been installed before acquiring this spectrum.

voltage) applied to H8, H9 and H19 (figure A.1) does not work according to the specification when switched to low voltage status. If the applied voltage was above $42\,\mathrm{V}$, the voltage provided to the corresponding electrodes was below the programmed voltage. This issue was resolved by designing a transport procedure with voltages below $42\,\mathrm{V}$ using the SIMION program. An important consideration for these simulations was the smaller inner diameter of the H8 and H9 electrodes. Since the detection system of the ST despite all the effort is not operational (section 3.2.8), the challenge would have been to be able to transport the ion cloud back to CT (a goal which was anyhow considered in [56]).

Figure 6.10 shows a comparison of the ion cloud before and after the transport to ST and back to the CT. It should be considered that the ion cloud spectrum before transport has undergone ten cooling ramps. The area under the spectrum after the transport has changed about 70%, which from the decrease of peak widths it can be concluded that the ion cloud has been cooled down during this transport. Additionally, an ion-loss as a result of transport is possible, since the electrodes H8 and H9 can act as filters and remove the charged particles with higher magnetron radius. Further studies to optimize the transport have been done after the time scope of this project, which will be reported in future reports.

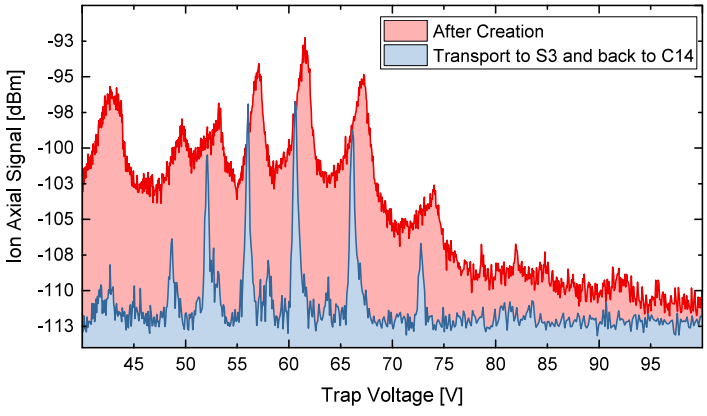

Figure 6.10: Spectrum of the ion cloud transported to the ST and back to the CT (2017). The first spectrum (red) is obtained from the ion ensemble in the CT after creation and ten cooling ramps. The second spectrum (blue) is the same ion cloud transported to the ST and back to CT.

6.5 Residual Gas Pressure Estimation at ARTEMIS

Before studying the resistive ion cooling process (or any other cooling technique), it is essential to have better knowledge about the residual gas pressure in the trap. Since, for highly charged ions this pressure directly translates to the lifetime of any given charge state.

In presence of ambient neutral gas, highly charged ions perform charge exchange, which can be used to estimate the pressure inside the trap. These estimations are normally utilized, since in typical cryogenic Penning traps direct measurement of the pressure is not feasible. Hence, by measuring the number of ions of a specific charge state in the course of the trapping a fair estimation of the residual gas pressure can be done. This is normally performed using a pure ion cloud, which in this instant reads as

$$P_R = \frac{1}{\sigma t_c}\sqrt{\frac{k_B T \mu_m}{3}} \quad \text{with} \quad \mu_m = \frac{m_R m}{m_R + m} \tag{6.1}$$

here σ is the cross section of electron capture from the neutral gas for the specific charge state, k_B is the Boltzmann constant, T is the temperature of the ion ensemble, m_R is the mass of the residual gas atom or molecule and m is the ion mass. In addition t_c is the lifetime of the specific charge state, which for large numbers of ions reads as

$$t_c = \frac{t_1}{\ln \frac{n_0}{n_1}}, \tag{6.2}$$

with t_1 being the time elapsed for the measurement, n_0 the number of particles at $t = 0$ and n_1 the number of particles at t_1. For cryogenic Penning trap experiments (e.g. ARTEMIS) the main contribution to the residual gas pressure is helium and hydrogen atoms and molecules, since the majority of other gases have already frozen out much earlier than reaching the final temperature of the setup.

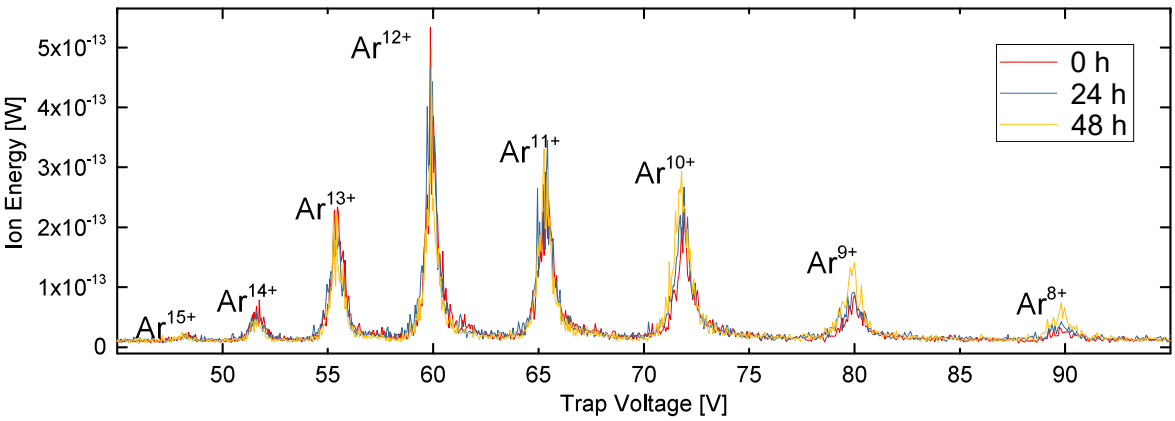

Figure 6.11: The mass spectra of different argon charge states in the CT, after five days of resistive cooling with time difference of 24 hours.

The calculation of t_c and consequently the P, for an ensemble with several charge states is not as straightforward as in the case of a single-charge-state ion cloud. Since at the same time that higher charge states ions convert to a lower charge state species, simultaneously that lower charge state species undergoes a charge exchange and populates its lower charge state ions. Thus, for exact calculation in such a case it is required to solve a coupled rate equation. Nevertheless, using the equation 6.1 the lower limit of the lifetime and eventually the lower limit of residual gas pressure can be estimated as [15]

$$t_c \geq \frac{t_1}{\ln \frac{n_0}{n_1}}. \tag{6.3}$$

After five days of ion cooling of the trapped ion cloud in the CT, i.e. ensuring the thermalisation of the ion ensemble and the detection system to about $4\,\mathrm{K}$, during three days with a time interval of 24 hours, three mass spectra were acquired. These mass spectra have been plotted in figure 6.11. The area under the curve of each charge state was integrated individually and plotted as a function of the elapsed time in figure 6.12. As a result of the extensive ion cooling, the area under each peak can be considered as a good measure of the particle number of each charge state.

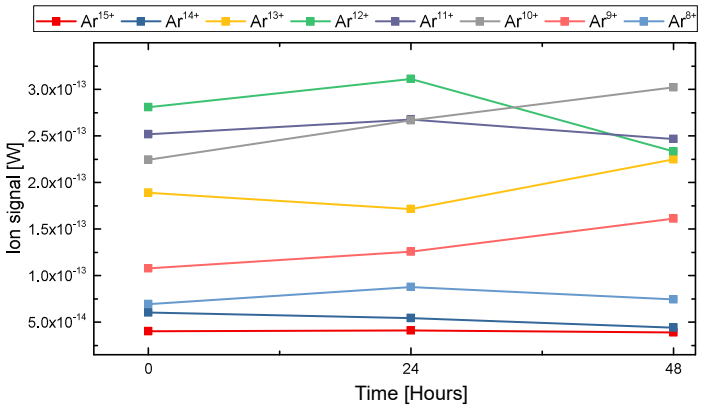

Figure 6.12: The changes of the area under the spectrum of each charge state individually in 48 hours, used as a measure of the particle number of a charge state.

If a conservative estimation is made, such that all the charge-states greater than Ar^{13+} have been converted to Ar^{13+}, using equation 6.2, the changes of Ar^{13+} in 48 hours leads to a lifetime of 22 days. Thus, with the Ar^{13+} charge exchange cross-section from Müller-Salzborn fit [11] and temperature of $4\,\mathrm{K}$, the P_R can be estimated to be around $3.2 \times 10^{-16}\,\mathrm{mbar}$. The estimated values ensure, while performing cooling experiments —typically within a time span of a day —the effect of charge exchange resulting in de-ionization of the trapped particles can be neglected.

6.6 The Nine-days Ion Storage Measurements

At the beginning of the 2017 measurement campaign, a measurement to observe the lifetime and residual gas pressure of the system, after the updates done on ARTEMIS, was performed. After ion creation at CT, the measurement system was set to acquire mass spectra with an interval of two hours. The trap was set to $55.7\,\mathrm{V}$ in the times between the spectrum readout, resulting in additional sympathetic cooling of the ion cloud through resistive cooling of Ar^{13+}. Figure 6.13 shows a selected number of spectra from this ion ensemble in the course of nine days.

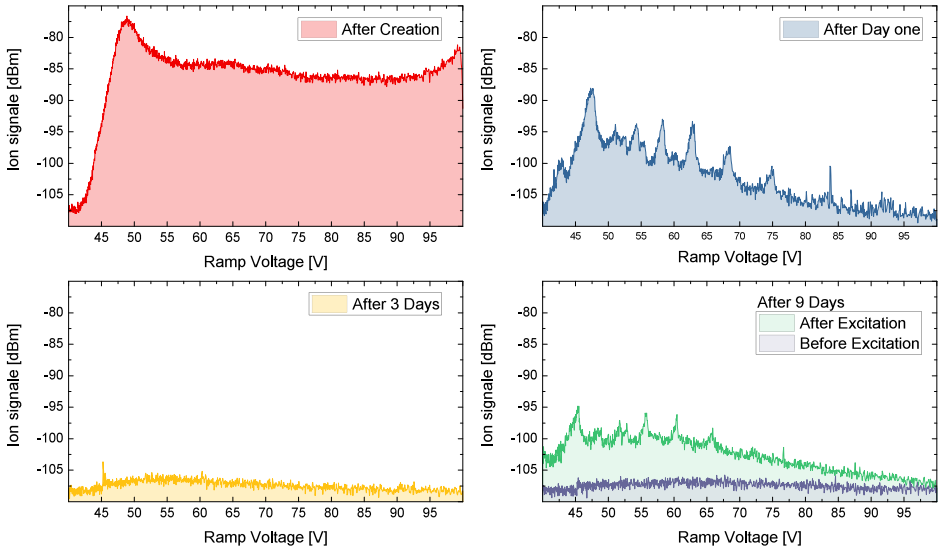

Figure 6.13: Spectra of the ion cloud measured in nine days at the CT. This measurement was done for validation of the residual gas pressure and lifetime of charge state

After the third day of the measurement it was assumed that as a result of the changes that have been done on the setup, the residual gas pressure has increased severely. Nevertheless, since this measurement was done remotely during an absence from the setup (while attending the 'quantum electrodynamics, precision physics and fundamental interactions' conference in Cargése, France), the measurement was not disturbed and just left running till it could be personally attended. On the ninth day of the ion storage and upon access to the setup, a rf excitation signal with $8\,\mathrm{V}$ peak-to-peak strength with 1000 bursts for $600\,\mu\mathrm{s}$ in the spectral region expected for Ar^{13+} and Ar^{12+} was shone in the CT trap. As a result of this excitation, a spectrum similar to a typical spectrum acquired at the first day was observed.

Excluding the first five acquired spectra, for which the ions were still too hot for an unambiguous identification in the spectra, the total area under each of the spectra was calculated and plotted as a function of time (figure 6.14). As a result of the excitation, the ion signal has recovered to about 72% of its first day value.

Considering the energy exchange that has happened (cooling and re-exciting), it can be con-

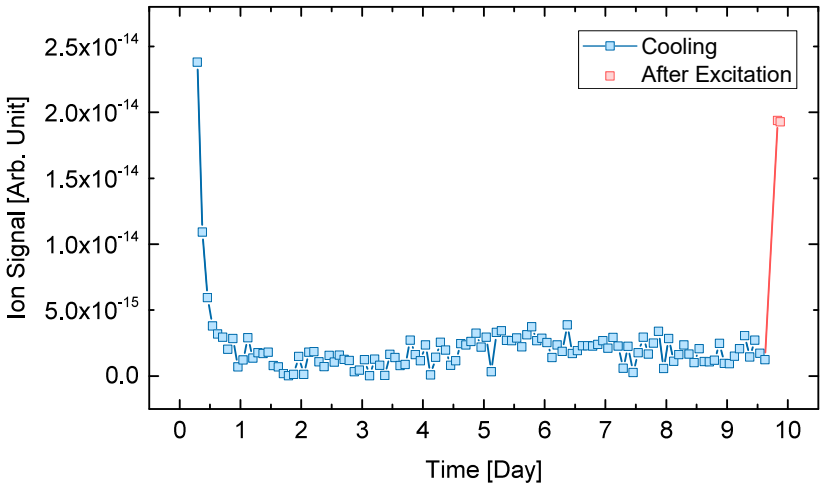

Figure 6.14: Nine-day measurement area under the spectra, the temperature decrease of the ion cloud to the level of the resonator detection circuit and re-excitation of the signal to 72% of the original signal are the significant features of this plot.

cluded that the charge exchange and ion losses during this time are not significant. For estimation of the actual particle numbers after excitation a calibration of temperatures as a function of the excitation signal is required. In addition,it was observed that given the sufficient cooling time it is possible to cool the ions to the level of thermal noise of the RLC-detection system, which is an important requirement for performing high precision spectroscopy. Nevertheless, the time scale observed (9 days) is too long, indicating the fact that optimization on the axial resonator of the creation trap is required. Finally, an unidentified peak was observed in the mass spectra around trapping potential of $46\,\mathrm{V}$ (e.g. a charge state of neon, Ne^{8+}), which could have affected the cooling of the ion cloud because of its different charge-to-mass ratio in comparison to the argon charge states.

6.7 Study of Resistive Cooling of Large Ion Ensembles

The importance and theory of ion cooling have been explained in chapter 5 and as it is stated that, among different cooling techniques resistive ion cooling has a significant role in many experiments including ARTEMIS. The density of the ions involved in the measurement scheme of ARTEMIS, approximately $10^5\,\mathrm{cm}^{-3}$, motivates a detailed study of the resistive cooling at the CT of ARTEMIS.

The RLC-circuit used for the axial motion detection and cooling is the ARES-CT, which has a resonance frequency of about $2\pi \times 741\,\mathrm{kHz}$ and quality factor of about a 1000. Its inductance is estimated to be about $3\,\mathrm{mH}$, hence according to equation 3.4 resulting in R_P of approximately $13.9\,\mathrm{M\Omega}$. The resistive cooling time constant for a single $^{40}Ar^{13+}$ ion (equation 5.7) with $D \approx 12\,\mathrm{mm}$ [21] is $\tau \approx 0.1\,\mathrm{s}$.

For typical resistive cooling at the CT of ARTEMIS an ion cloud with charge states ranging from $8+$ to $15+$ is studied, with high number of particles N in a non-ideal trapping potential. Thus, the effective $D \approx 43.47\,\mathrm{mm}$ calculated in section 5.2.3.4 should be used to calculate

a cooling time constant. Considering Ar^{13+} as the average charge state, in the spectrum of the trap charge states of a typical stored ion ensemble in the CT, the cooling time constant is equal to $\tau \approx 2.90\,\mathrm{s}$.

For this measurement of typical mass spectra as described in section 6.1 acquired (e.g. figure 6.1), after each mass spectrum has finished the trapping potential was set back to the initial value and another mass spectrum was recorded. As a result, in each measurement presented a sequence of mass spectra were acquired. As discussed earlier in section 6.5 the charge exchange effects for short time scales can be neglected, thus the area under each individual peak in the spectrum can be considered as an energy measure of that species.

The comparison of the estimated sympathetic thermalisation time constant of ($\tau_T = 6.7\,\mathrm{ms}$) and the values expected for resistive cooling time constants (in orders of seconds), reveals the fact that the thermalisation between different ions species in the ensemble is much faster than the active resistive ion cooling of a specific species. Therefore, cooling one charge state is effectively cooling the entire ion cloud in the spectrum. Furthermore, a usual spectrum acquisition takes around $550\,\mathrm{s}$, such that even an individual step of the voltage ramp in this manner is much longer than the thermalisation time of the ion cloud.

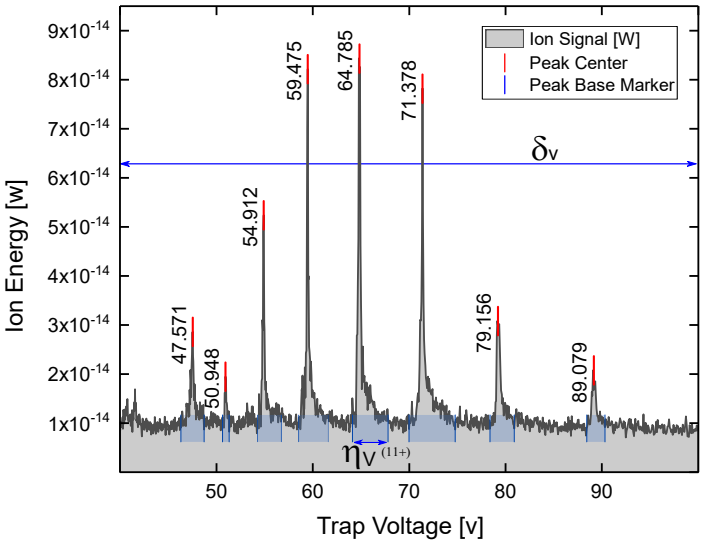

Figure 6.15: A mass spectrum readout with the involved parameters for time corrections used in evaluation of resistive cooling behavior of the ion ensemble. The η_v only shows the fraction of the ion signal width of Ar^{11+}, each charge state contributes to the total value of η_v individually.

To be able to compare the measurements with the cooling models presented in section 5.2.3, the time of the cooling cycle should be converted to an equivalent effective time t, accounting for the actual total time that all ions would have been in resonance with the RLC-circuit. Each cooling cycle consists of one spectrum which is acquired in a acquisition time t_A, to calculate the equivalent time t, two effects—by accounting for correction factors—must be taken into account. The first correction factor accounts for the fraction of the total mass spectrum's width δ_ω interacting with the resonator's width $\Delta\omega$, which reads as $\Delta\omega/\delta_\omega$. Second, considering the shape of mass spectra, there are regions that appear to have no ion signal (between two adjacent ion peaks). Thus, no cooling is taking place in these parts of the spectra. As depicted

in figure 6.15 this correction factor can be calculated as the ratio of the summation over the ions signal peak widths of all charge states η_v to the total spectral width δ_v. Practically, the first correction factor is calculated in frequency domain and the second one in the voltage domain.

Finally, by applying the two correction factors on the measurement time the equivalent correct time reads as

$$t = t_A \frac{\Delta\omega}{\delta_\omega} \frac{\eta_v}{\delta_v}. \tag{6.4}$$

Since further cooling of the spectrum makes the peaks narrower, this time changes from cycle to cycle.

6.7.1 Demonstration of Temperature Equilibrium

In theory, when sufficient time is given to the ion ensemble to interact with the RLC detection system, the temperature of the trapped ions should reach an equilibrium with the thermal bath that they are interacting with (section 5.2.3). Regardless of the initial temperature the final temperature of the ion cloud should be in the same range, in this case about $4\,\mathrm{K}$. In order to study this concept, five ion creation processes with different parameters (caption of figure 6.16) were performed and hundred consecutive mass spectra were acquired for each ion ensemble (5×100 mass spectra). As already discussed the area under the spectrum can be used as a measure of the ions' temperature. Thus, for each spectrum the area under the spectrum was integrated and plotted as a function of their cycle number (figure 6.16). Besides the ion cloud created with a gas injection (creation 3), the temperature of the other clouds —with roughly the same number of trapped ions —reaches approximately the same value. In the case of the creation 3, due to higher number of argon atoms injected into the system during creation and higher electron energy, a larger total area under the curves can be expected.

6.7.2 Electronic Noise Temperature Estimation at ARTEMIS

As explained in section 5.1.1 by measuring the amplitude of the resonance spectrum of the RLC detection system, which is in thermal equilibrium with the ions, the temperature of an ion ensemble can be calculated. First the KEYSIGHT N9000B CXA spectrum analyzer read-out was centered at about $741\,\mathrm{kHz}$ (the detection circuit's resonance frequency at the time) with a span of $3\,\mathrm{kHz}$. Then the trapping potential was set to a harmonic trap configuration of $55.7\,\mathrm{V}$, which is the expected trap voltage for bring Ar^{13+} into resonance with the RLC-circuit. Afterwards, the thermal spectrum of the ARES-CT was measured while there were

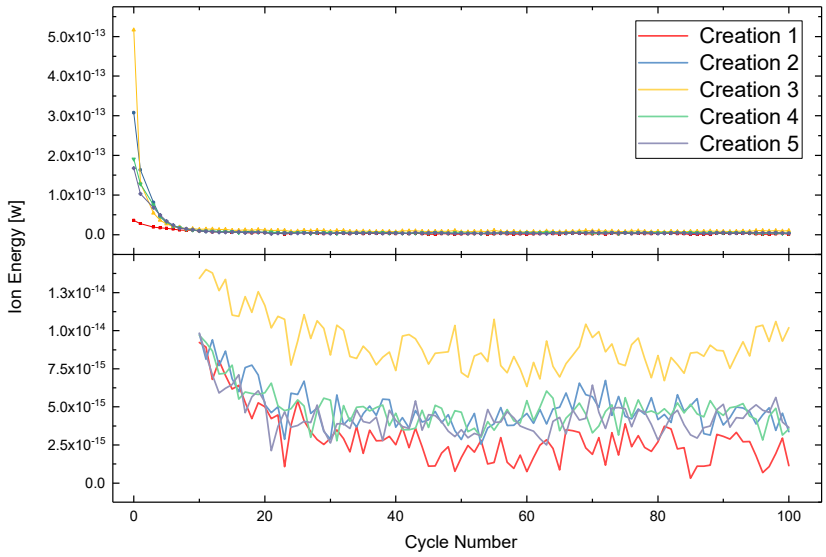

Figure 6.16: A comparison of the cooling procedure of five ion clouds with different initial areas under the curve. The lower plot shows a zoomed picture of the final ion signal. The parameters related to each curve are as follows;
Creation1: Heating OFF, Breeding 5 s, NO Gas pulse, V_{FEP} = -1500 V ,V_{acc} = 1200 V, V_{TRAP} =200 V.
Creation2: Heating OFF, Breeding 5 s, NO Gas pulse, V_{FEP} = -1750 V ,V_{acc} = 1250 V, V_{TRAP} =200 V.
Creation3: Heating ON, Breeding 5 s, Gas Pulse ON, V_{FEP} = -1750 V ,V_{acc} = 1250 V, V_{TRAP} =500 V.
Creation4: Heating OFF, Breeding 5 s, NO Gas Pulse, V_{FEP} = -1750 V ,V_{acc} = 1250 V, V_{TRAP} =350 V.
Creation5: Heating OFF, Breeding 5 s, NO Gas Pulse, V_{FEP} = -1500 V ,V_{acc} = 1200 V, V_{TRAP} =350 V.

no ions in the CT. In the next step, a typical ion creation was performed and in five steps the trapping potential was lowered to $55.7\,\text{V}$ from $250\,\text{V}$, as a result bringing the Ar^{13+} charge states into resonance with the RLC detection system, hence cooling the ion cloud. Considering the $\tau_T = 6.7\,\text{ms}$ sympathetic cooling time constant between the ions in the ensemble, with good estimation the temperature of the entire confined ions should be equal to the temperature of the Ar^{13+} fraction of it. While keeping the ions in resonance with the detection system, twenty-three spectra of the ARES-CT were recorded in $197\,\text{min}$, with the same spectrum analyser settings as set initially. Figure 6.17 shows six selected spectra of these measurements alongside the resonance spectrum of the resonator with an empty trap.

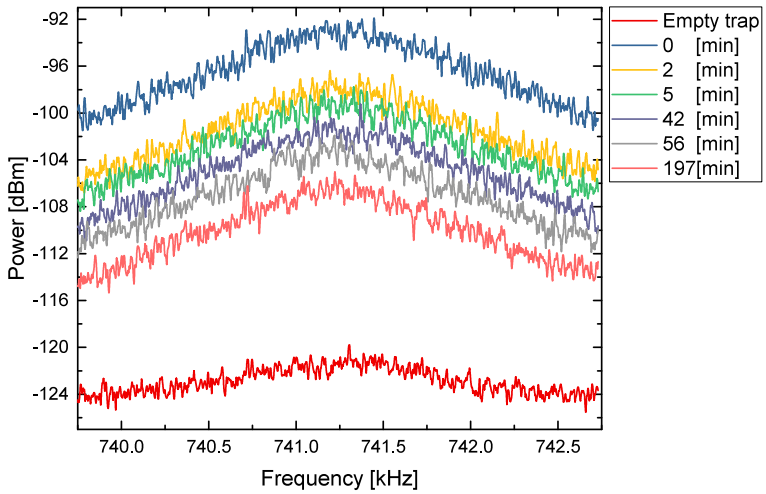

Figure 6.17: The spectra of ARES-CT circuit recorded for the empty trap and six selected spectral responses after trapping an ion ensemble with presumably different temperatures as a result of resistive ion cooling.

In order to extract the peak power of the spectrum, a Lorentzian fit was performed on each spectrum, then the power peak was converted to its equivalent voltage, considering the impedance of the detection system. Finally, using the equation 5.1 temperature of the ions was estimated. To perform a calibrated measurement of the temperature in this fashion, the loss and amplification of the rf readout line and the resonance circuit effective resistance R_P must be measured exactly, here a typical value for $R_P \approx (14\,\mathrm{M\Omega})$ was estimated and the loss and amplifications of the rf signal was neglected. Nevertheless, assuming there is no additional noise source, the temperature estimated for the spectrum acquired for an empty trap can be used as the $4\,\mathrm{K}$ line. Hence, the ratio of $4\,\mathrm{K}$ and the estimated temperature for an empty trap can be used to scale the other obtained temperatures when the ion cloud is present.

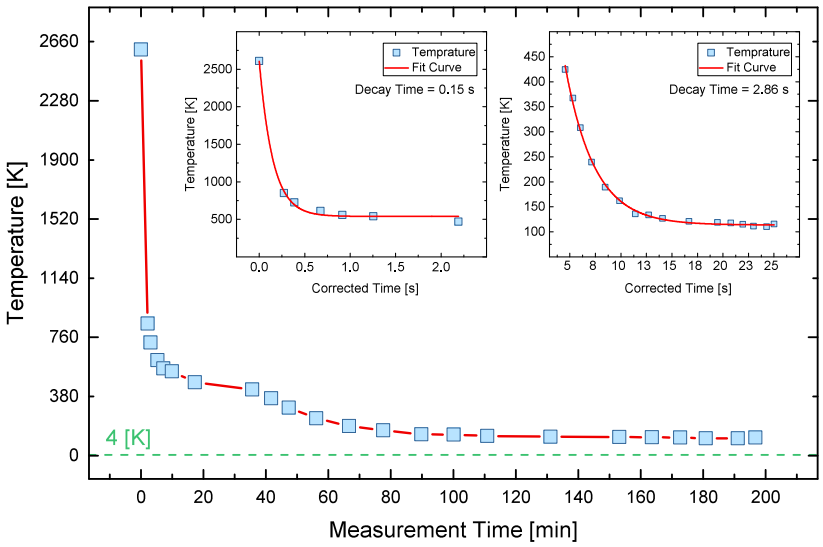

Figure 6.18: Electronic noise temperature estimation at ARTEMIS. The temperature of the unloaded ARES-CT circuit is plotted as green line (4 K). The inset on the left side is for the first seven estimated temperatures, which can be fitted with a fast exponential decay function. The inset on the right side shows the data point of the next sixteen estimated temperatures and the more moderate exponential function fitted to them.

Figure 6.18 shows a plot of the temperatures of the ion ensemble as a function of time. The temperature of the resonator detection system —without the trapped ions—is roughly three orders of magnitude lower than the temperature estimated after loading the trap with ions ($2600\,\mathrm{K}$), which after $197\,\mathrm{min}$ of resistive cooling decreases to about $115\,\mathrm{K}$.

The cooling behavior of the ion ensemble can be described with two exponential decay functions fitted to the data, an initial fast temperature decrease followed by a slower one. Considering the fraction of the resonator width $\Delta\omega = 1.57\,\mathrm{kHz}$ at the time of this measurement and frequency width of the expected spectrum for a typical ion ensemble and based on the discussion in section 5.2.3.5, a correction factor of $1/472$ was applied to the acquisition times. Then the decay times τ_N of the two cooling curves observed in this measurement were calculated to be $0.14\,\mathrm{s}$ and $2.86\,\mathrm{s}$ for the fast and slower curve, respectively (inset of figure 6.18).

6.7.3 Resistive Cooling of Ion Cloud after Creation

Directly after an ion creation in the CT (section 6.2), with $V_{\mathrm{FEP}} = -1.6\,\mathrm{kV}$, $V_{\mathrm{acc}} = 0.95\,\mathrm{kV}$ and breeding time of $1\,\mathrm{s}$, a hundred axial mass spectra were recorded; the evolution of the ion cloud as a result of the axial resistive cooling is depicted in figure 6.19. The first spectrum acquired shows that the ion ensemble has an extremely high temperature, in a manner that all the individual charge states peaks are blurred. After a number of spectra, four to eight, the peak of each individual charge state starts to appear. Furthermore, after extensive cooling of the ion cloud (around fiftieth spectra) the anharmonicities caused by $C4$ coefficient of the electric potential in the CT (section 2.2.2) start to affect the shape of the peaks observed in the spectrum [66].

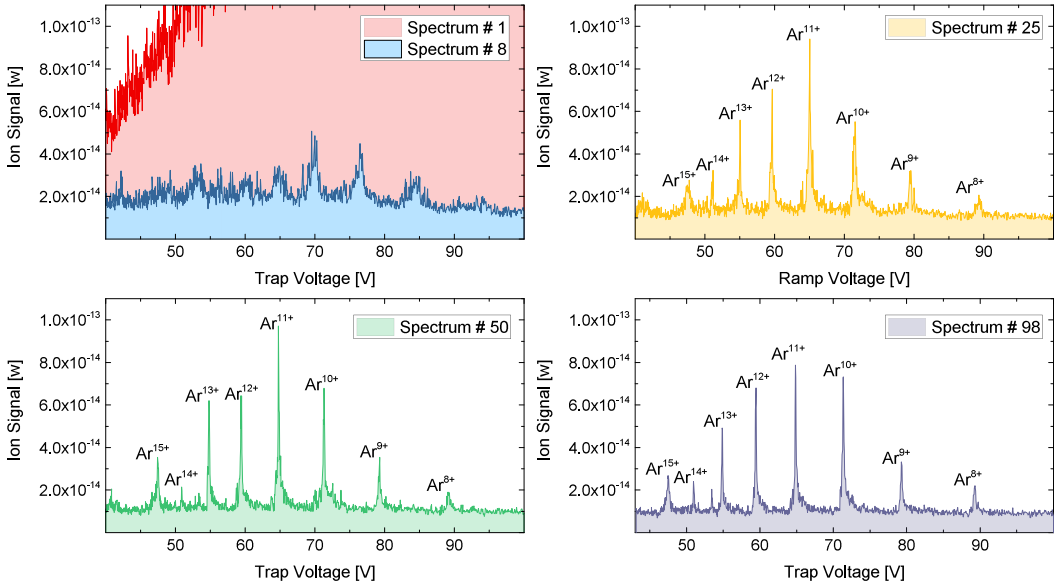

Figure 6.19: Ion ensemble evolution as a result of 100 resistive cooling ramps directly after creation. The first ion cloud spectrum (depicted on the top left plot in red) appears as a blurred hot spectrum with no clear signs of the charge states. After eight mass spectra the individual charges appear.

As the first step of evaluation, the integral of the total area under each spectra was calculated and plotted as a function of the corrected time (figure 6.20). Each spectrum readout has a time interval of $550\,\mathrm{s}$. Considering the spectral width of the ion cloud $\delta_f \approx 330\,\mathrm{kHz}$ and the ARES CT span $\Delta\omega = 860\,\mathrm{Hz}$, the first time correction factor reads as $\Delta\omega \approx 1/385$. The value of the second time correction factor was individually calculated for each spectrum as the ratio of the total peak widths to the width of spectrum in the voltage domain, η_v/δ_v. As also depicted in figure 6.20 the ion energy is given in arbitrary units, since the actual amplification factors at $4\,\mathrm{K}$ of the detection system need to be measured [3]. It is clear that this cooling curve can be fitted with two exponential decay functions; an initial fast decay with $\tau_{E1} = 0.67\,\mathrm{s}$ and a more moderate cooling behavior with $\tau_{E2} = 6.17\,\mathrm{s}$.

[3] planned for near future.

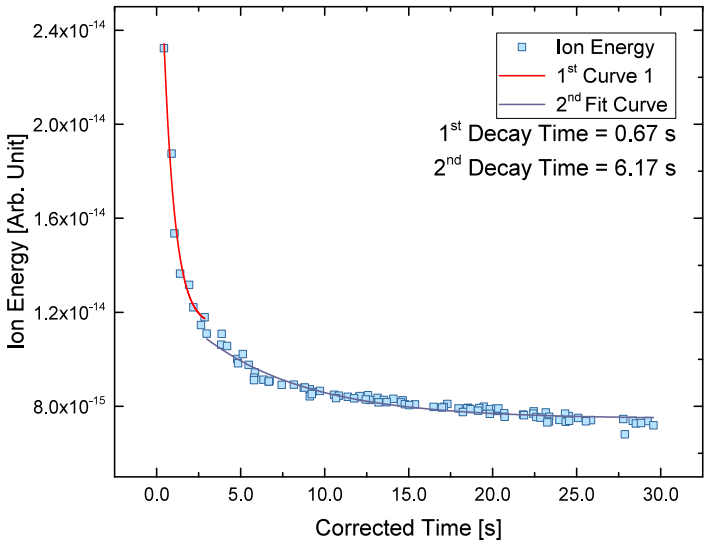

Figure 6.20: The energy evolution of an ion cloud directly after creation as a result of resistive cooling. Only the very first spectrum after creation with extreme temperature is not considered. Two exponential decay curves have been fitted to the data.

The first fast decay is due to the convolution of extremely high initial energy and energy transfers from the other degrees of freedom to the axial energy. The second decay is the part of the cooling curve, where the axial cooling of the ion could gets dominant and becomes effective. Therefore, at the moment the first decay will be neglected. Nevertheless, in reality these two cooling curves do not have clear boundaries. As depicted in Figure 6.21 one can consider the axial cooling becoming more prominent after four or after eight cycles of cooling. In doing so, two cooling time constants in the same order of magnitude as the theoretical estimated value are yielded after fitting the data with an exponential decay function. This ion cooling behavior to good extent matches the ion cooling of the center-of-charge model presented in section 5.2.3.

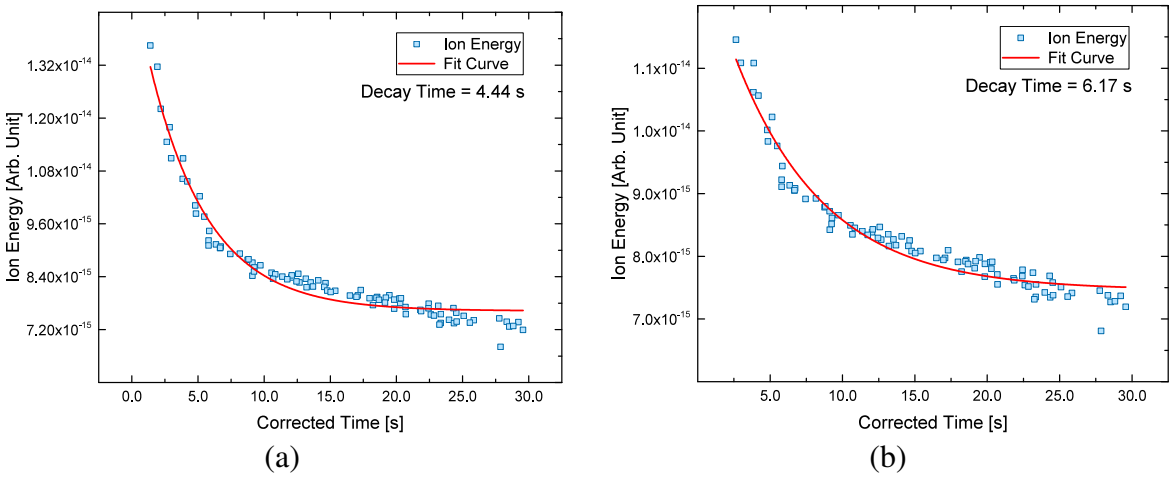

Figure 6.21: A comparison between cooling curves of the ion cloud, when the first four spectra are removed (left) and eight spectra are removed (right).

Another effect observed while cooling the ions is shifts of the ions' oscillation frequency to their expected axial motion frequencies. Using Ar^{11+} as a probe, which is the average charge

state of the present ion species in this cloud, the general frequency shift of the ion cloud was studied. The trapping voltages corresponding to this charge state's peak were converted to the equivalent peak frequencies using equation 2.15 and plotted as a function of the corrected time (Figure 6.22). In the first $5\,\mathrm{s}$ of cooling, a strong decrease in the center frequency of the ion peak is observed. Thereafter, the decrease becomes moderate and around $15\,\mathrm{s}$ of cooling the frequency starts to increase towards its actual theoretical value. Generally, an increase towards the theoretical axial frequency should be observed, as will be demonstrated for the other two cases presented (sections 6.7.4 and 6.7.5). However, in this case the frequency shift is not showing the pattern that is expected. The overall appearance of the spectra is conserved during the cooling process, indicating that no considerable change happens in the combination of the confined species. Thus, a reason beyond the process of resistive ion cooling can be responsible for such a behavior.

One possible explanation would be that the ion cloud is not located at the center of the trap. The initial decrease can be due to the ion ensemble shifting to the center of the trap and the remaining shift being a result of the energy change in the system due to cooling. The initial decentralization of the ion cloud can be associated to charge-up of the electrodes and possible frozen particles on the surface of the electrodes, which can lead to unexpected anharmonicities in the electric potential, thus a strong shift irrespective of the ion energy. The expected shift then will be dominated by the time constant of de-charging the electrodes and may be in order of magnitude of several minutes or hours.

As mentioned in section 5.1.2, the spectral width of ion peak signal can be used as a measure of the ensemble's temperature. Figure 6.23 shows the evolution of the spectral width of this ion species as a function of the corrected time. As in the case of ion energy study of this ensemble, the four (or eight) initial spectra are not in the same energy scale as the other spectra, thus for further evaluation they have been removed. The observed relative signal

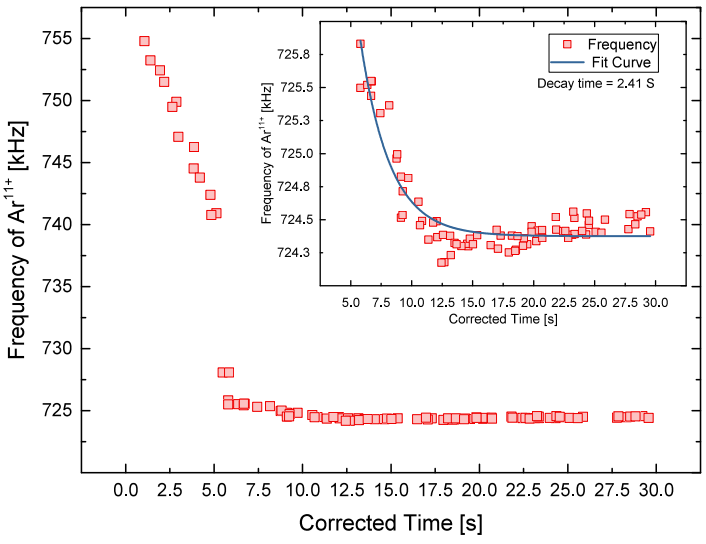

Figure 6.22: Frequency of the ion cloud as a function of corrected time for an ion cloud directly after creation. The Ar^{11+} peak has been chosen as a probe to study the signal shift.

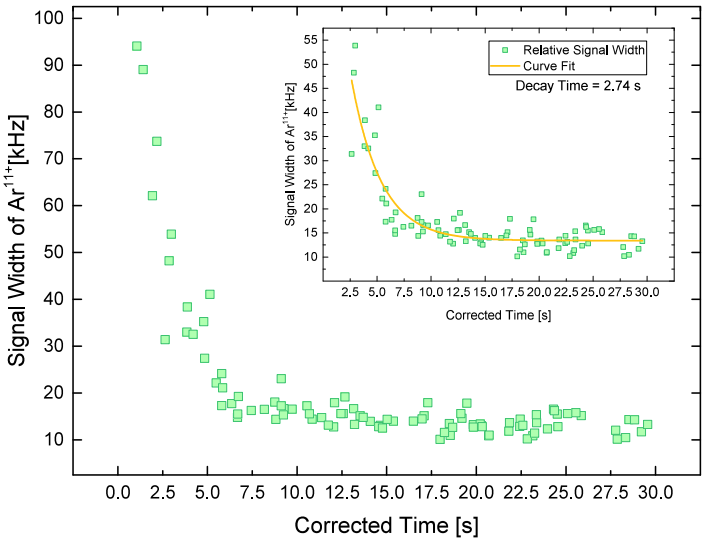

Figure 6.23: Spectral width evolution of the ion ensemble directly after creation. The inset depicts the same curve excluding the first four spectra, fitted with an exponential decay function.

width of 1.4×10^{-2} for the last spectrum of the cooling process (considering its corresponding peak frequency of $724.5\,\mathrm{kHz}$) translates according to the calculation done in section 5.1.2 to a temperature of $7.96\,\mathrm{K}$ for the ion ensemble.

Due to the extreme temperatures of the ion ensemble at the beginning of this measurement, despite the fact that the cooling time constants are in the same range, different time evolution of the spectral features of the cooling do not show the relation that is expected from them as discussed in section 5.2.3.6.

6.7.4 Single Species Ensemble —Ar^{13+}—Resistive Cooling

For this measurement after a creation with typical parameters, using a SWIFT procedure (section 6.3) the ion cloud was reduced to only contain Ar^{13+} charge state. The last excitation of the ions in the SWIFT procedure was performed with $8\,\mathrm{V}$ peak-to-peak power, which afterwards left an excited confined ion ensemble in the trap. A hundred mass spectra were acquired, figure 6.24 shows the changes in the mass spectra of the ion cloud. In this measurement, around the thirty-fifth spectrum, the ion thermalises with the RLC-circuit and loses its observability (it should be excited using a rf signal to be measurable again).

The readout time of each mass spectrum acquisition in this measurement is around $285\,\mathrm{s}$, in the same fashion as before the acquisition time was converted to the corrected time. Afterwards, similar to section 6.7.3 the ion energy evolution of the ion ensemble was plotted as a function of corrected time (Figure 6.25).

As one expects, the resistive cooling of the ion energy curve shows a perfect exponential decay behavior, since the initial energy and particle number of the Ar^{13+} ion ensemble is relatively lower (as a result of SWIFT procedure) than the ion cloud studied in section 6.7.3. Nevertheless, the decay time constant is a factor of about 2 smaller than the theoretical value.

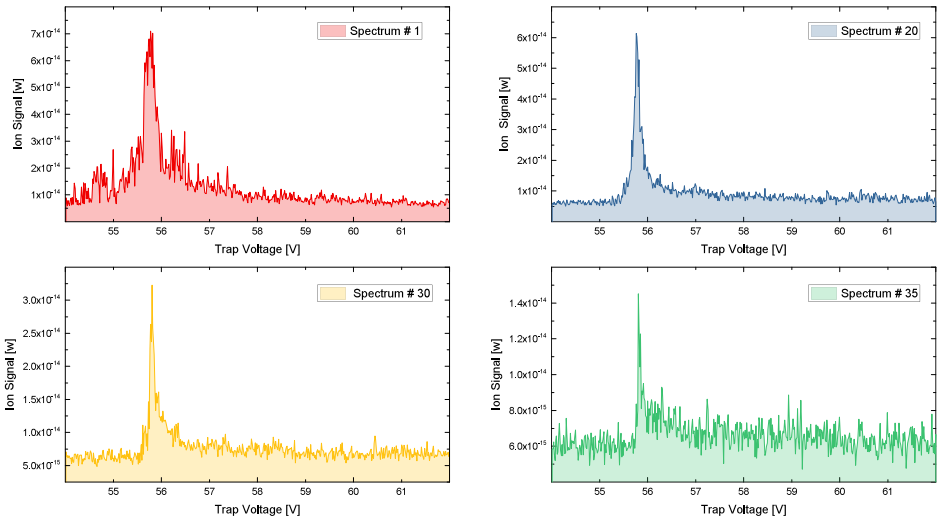

Figure 6.24: Spectrum evolution of Ar^{13+} as a result of resistive cooling. The thirty-fifth spectrum is were the ion peak is last observable. After this spectrum in order to again observe the spectrum rf excitation is required.

As a possible explanation, the spatial distribution of the ion cloud along the trap center can be responsible for this modification, thus the need to estimate a new effective D with new parameters for a more accurate value.

As the next step, the frequency shift of the ensemble was studied as a function of the corrected time (figure 6.26.a). The final frequency, before the ion cloud totally thermalises, is about $730.809\,\mathrm{kHz}$. This value is about $6.4\,\mathrm{kHz}$ smaller than the estimated theoretical values presented in table 2.2. In addition to the thermalisation of the ions with the RLC circuit, extrapolating the cooling curve with the obtained growth rate indicates that the shift of the ion cloud can no longer be associated with the temperature of the ensemble. This discrepancy can be due to the anharmonicity of the electric potential at the CT [20] and/or the space charge frequency shift presented in section 2.4. Since these shifts are in the same order of magnitude for Ar^{13+}, disentangling them requires further information (particularly the number of particles). In an ambiguous estimation —in case the shift was only caused by

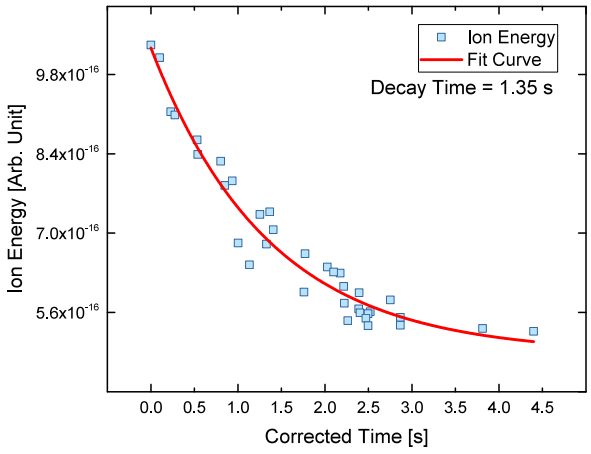

Figure 6.25: Ion energy evolution as a result of resistive cooling of Ar^{13+} ensemble. The data is fitted with an exponential decay function.

the space charge effect—a number density of $3.17 \times 10^3\,\mathrm{cm}^{-3}$ can be extracted from figure 2.11.b for the current ion cloud.

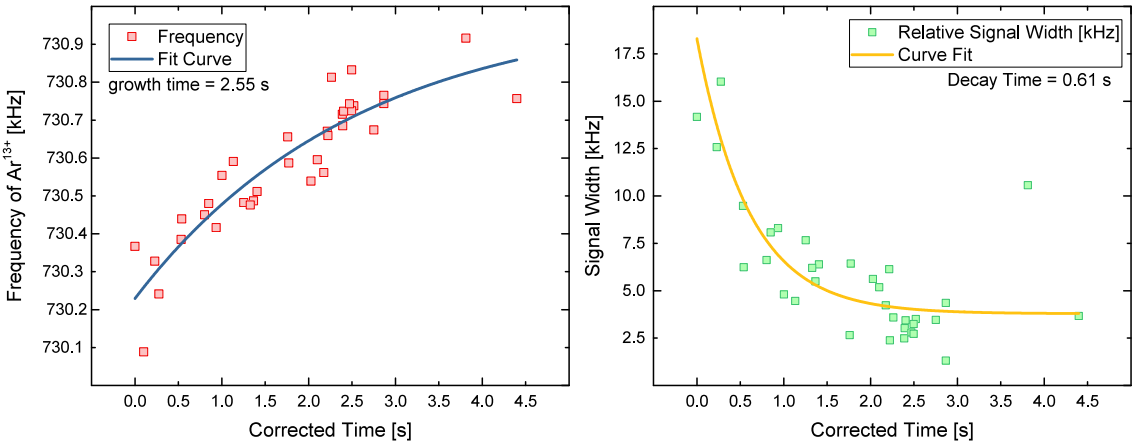

Figure 6.26: (a) Frequency shift of the Ar^{13+} ensemble as a result of resistive cooling. (b) Spectral width evolution of the Ar^{13+} cloud as a result of resistive cooling.

Figure 6.26.b shows the spectral width changes of Ar^{13+} versus the corrected time of the cooling cycle. According to the discussion in section 5.1.2 for the first mass spectrum a temperature of about $13\,\mathrm{K}$ can be estimated for the ion ensemble. As a result of resistive cooling the last observable spectrum has spectral width of 4×10^{-3} at peak frequency of $730.8\,\mathrm{kHz}$, which translates to an estimated temperature of about $4.24\,\mathrm{K}$. Since the ion ensemble is afterwards no longer observable, this estimation might be not far from the actual temperature of the RLC-circuit. An exponential decay function can be fitted to this curve as well, which is two times faster than the ion energy decay τ_E in figure 6.25. Although in this case, the ion cloud has a much lower initial temperature than the ion ensemble presented in section 6.7.3, still the relation between different cooling time constants does not match the model presented in section 5.2.3.6. This discrepancy indicates that a more advanced theoretical study is required to understand the resistive cooling time evolution.

6.7.5 Consecutive Resistive Ion Cooling of an Ensemble

For this measurement the created ion cloud in the CT has been modified using the SWIFT technique to contain mostly Ar^{13+}, without removing the other charge states totally. As a result of the SWIFT technique with 1000 burst excitation signals with $8\,\mathrm{V}$ peak-to-peak power, the ion ensemble had a high energy. First, one hundred and fifty mass spectra was acquired. Afterwards using an rf signal the energy of the ion ensemble was excited two times to a value close to the initial energy and then resistively cooled each time. Finally, after the fourth excitation of the ion cloud again one hundred and fifty spectra were obtained. In this fashion,

any kind of possible residual effect by previous cooling cycles can be explored (if present). Figure 6.27 shows the integrated area under the curve of the acquired spectra as a function of the readout cycle number, again as a measure of ion energy.

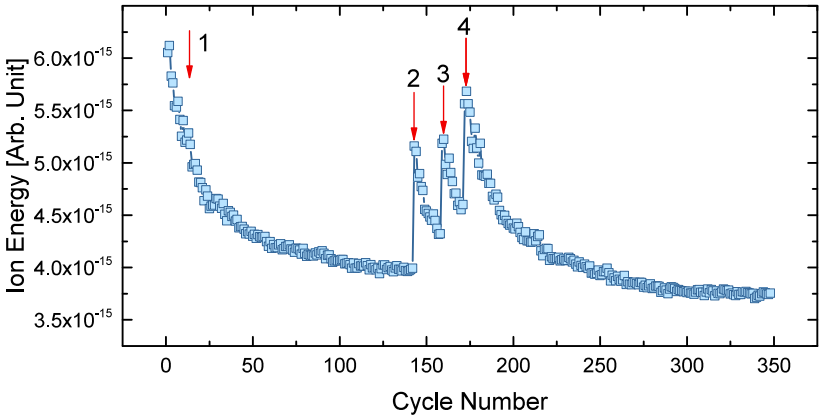

Figure 6.27: The energy scale evolution of consecutive resistive ion cooling of the same ensemble in four cycles.

Using a selected number of spectra the spectrum evolution happening in the first and last cooling decays is shown in figures 6.28 and 6.29, respectively. As shown in these spectra Ar^{13+} charge state is the majority of the ions in the ensemble.

As in the two previous examples, for each of the decay curves the ion energy, frequency shift of the Ar^{13+} and the spectral width of the Ar^{13+} peak were calculated for all 150 spectra and plotted as a function of the corrected time —time correction procedure used is the same as the previous two cases. Figure 6.30 shows the plots of these evaluations performed on the ion cloud.

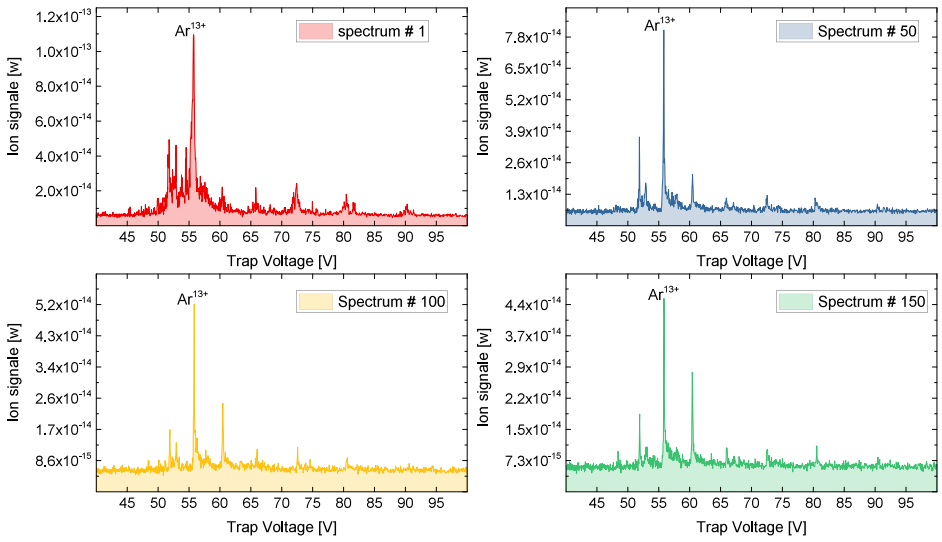

Figure 6.28: The spectral evolution observed in the first decay as a result of the resistive cooling of the confined particles. Presented for comparison with figure 6.29

The ion energy decay curves were fitted by an exponential decay function, resulting in similar decay time constants of about $\tau_E = 4.7\,\mathrm{s}$. These values are in fair agreement with the theoretical calculation and second decay observed in the data presented in section 6.7.3. The center frequency shift of the ion cloud seems to behave as expected, unlike the ion cloud

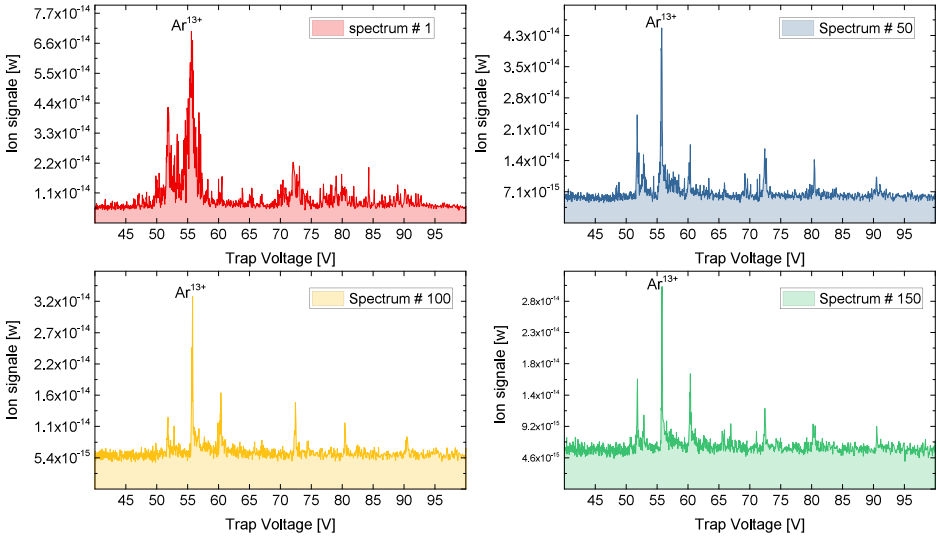

Figure 6.29:
The spectral evolution observed in the second decay as a result of the resistive cooling of the confined particles. Presented for comparison with figure 6.28

which has been studied in section 6.7.3, which gives more evidence supporting the idea that for an ion cloud studied after creation a shift due to reasons such as electrode charge-up can be expected. Finally, from the measured relative frequency width of the ion cloud at the end of the first cooling cycle of 7.3×10^{-3} (at a peak frequency of $730.8\,\mathrm{kHz}$) and at the end of the fourth cooling cycle of 9.8×10^{-3} (at a peak frequency of $730.5\,\mathrm{kHz}$), temperatures of $6.64\,\mathrm{K}$ and $5.72\,\mathrm{K}$ can be estimated by use of the approach described in section 5.1.2, respectively.

The similar behavior observed in these consecutive cooling processes leads to the conclusion that the resistive ion cooling is independent of the excitation and cooling cycles. The parameters defining the cooling time constant, as expected, are the geometry of the trap, the magnetic and electric potential, the specification of the RLC detection system and the specification of the ion ensemble itself.

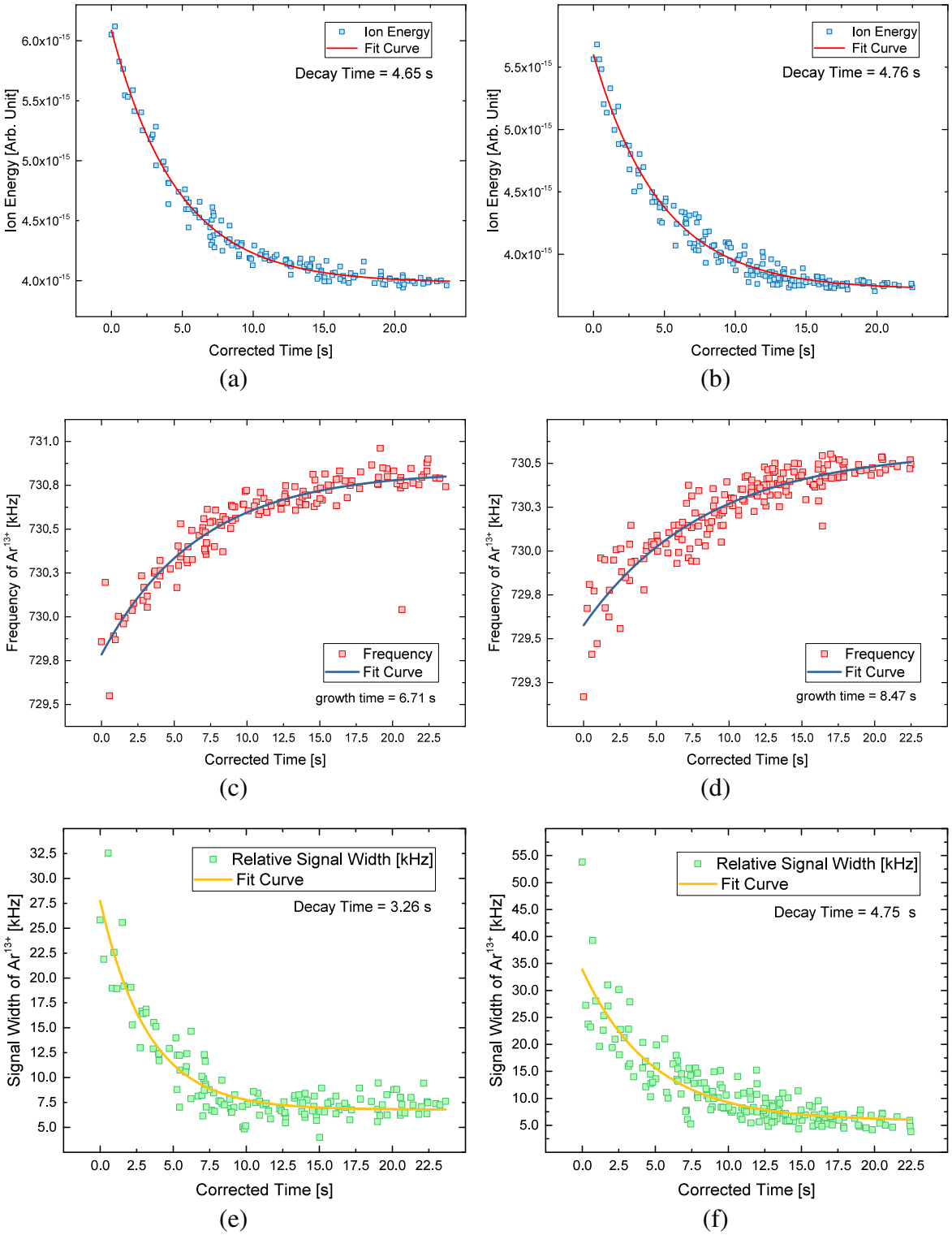

Figure 6.30: The ion energy, frequency shift of the Ar^{13+} and the spectral width of the Ar^{13+} peak as a function of the corrected time for the same ion cloud in two of the consecutive cooling procedures. The left column of plots belong to the fist cooling curve and the one on the right belong to the fourth cooling process.

CHAPTER

SEVEN

CONCLUSION AND OUTLOOK

Primarily, this thesis widens the knowledge about the non-destructive detection and resistive cooling of highly charged ion ensembles for atomic spectroscopy in the ARTEMIS Penning trap at HITRAP. Among the different cooling procedures possible, resistive cooling of the ion ensemble stored at ARTEMIS has an important role, due to ease-of-use and efficiency. However, since ARTEMIS's double resonance spectroscopy scheme involves 10^5 particles, the common knowledge available for the detection systems and their application as resistive cooling circuits was not totally compliant to the case of ARTEMIS. To this end, two main categories of studies have been conducted in this project. Firstly, a study of different components of the detection system was performed and secondly, experiments on the resistive cooling behavior of ion ensembles were conducted.

As presented in chapter 3, a comprehensive study on different components of the cooling circuit were performed, to optimize the detection system according to the needs of ARTEMIS. Different combinations of two geometries (helical and toroidal) with two wire materials (normal -conducting copper and superconducting niobium-titanium) were studied for development of the inductor coils of the RLC-circuit. A superconducting toroidal resonator can deliver a significantly higher quality factor in comparison to the other tested inductor coils, but as it turned out that developing and maintaining such a coil is more challenging. A normal-conducting helical resonator is easy to make and can be used as a tool for checking all the connections and parts involved in the detection system at room temperature.

The behavior of a NbTi superconducting toroidal resonator, with initial quality factor about 21000 and an unloaded resonance frequency of $2\pi \times 1\,\mathrm{MHz}$, in a variable magnetic field up to $6\,\mathrm{T}$ was studied, indicating a strong decrease in the Q-values (down to roughly 7000 at $6\,\mathrm{T}$) and a shift in the resonance frequency of the spectrum (about $20\,\mathrm{kHz}$) as a function of the applied magnetic field. Hysteresis effects were observed in this system, but not on a level that can affect the performance of the detection system. The results of this study are also

presented in [76].

The cyclotron resonator detection system requires a range of frequency adjustability in order to be put in use, therefore a varactor diode board has been realized and installed. Utilizing the varactor diode board, the resonance frequency of the cyclotron detection system at ARTEMIS was set to $35\,\mathrm{MHz}$ with an adjustment span of $3.5\,\mathrm{MHz}$ around this frequency. An important milestone is the measurement of the cyclotron frequency of the the stored ions, which with the current developments can be achieved in the near future.

The second important series of measurements presented in this thesis (Section 6.7) are regarding the study of resistive cooling of the ion ensemble. Firstly, a theoretical treatment of the effective electrode distance D for a large spatial distribution of ions in the creation trap of ARTEMIS has been performed, leading to a value of $D \approx 43.47\,\mathrm{mm}$. Using the calculated value of D, the cooling-time constant of the ion ensemble $\tau \approx 3\mathrm{s}$ was calculated and put to test against different types of ion cloud specimens: (1) an extremely hot and dense ion cloud (2) a cooler less populated ion cloud (3) a cold ion cloud with low number of Ar^{13+} ions. The measured time constants are in the same order of magnitude, but a discrepancy between these values is observed. Furthermore, by study of the consecutive cooling behavior of an ion cloud it became clear that the cooling response of the ion cloud does not possess a memory. In the course of these studies a first measurement of final ion temperature and thermal evolution of the ion cloud using the electronic noise of the RLC-circuit and the spectral width of a specific ion species peak was estimated, which indicated an efficient cooling in the creation trap using the RLC-circuit down to $4\,\mathrm{K}$ in the case of a single species ion cloud.

During the course of this study, a lifetime of twenty-two days for a specific ion species was estimated, which translates to a residual gas pressure of $3.2 \times 10^{-16}\,\mathrm{mbar}$ (section 6.5). In an attempt to validate this estimation, a typical ion cloud was created and stored for over nine days, during which the ion ensemble thermalised with the RLC-detection system and was re-excited afterwards.

Finally, successful transport of the ion cloud to the spectroscopy trap (and back to the creation trap) is reported (6.4). Despite all the efforts at this point, the RLC detection system of the spectroscopy trap is not working. Therefore, an optical observation of the ion cloud in the ST using electron excitation of the ensemble is planned. Furthermore, a new upgrade and development phase for the experiment, as result of newly obtained knowledge, is foreseen in near future.

At this point, it is not far from reality to claim the first proof of concept measurement for microwave-laser double resonance spectroscopy is closer than ever. Moreover, the plans for connecting ARTEMIS to the HITRAP beamline have proceeded in a promising fashion.

APPENDIX

A

ARTEMIS WIRING DIAGRAMS

The changes and upgrades done in the wiring of ARTEMIS in comparison to [21] are as follows:

- Adding the varactor diode board, which requires two additional lines for the heater and one for biasing.
- Installing a new amplifier board and removing to extra connection line .
- Changing the resistors used in the HV-filter board.

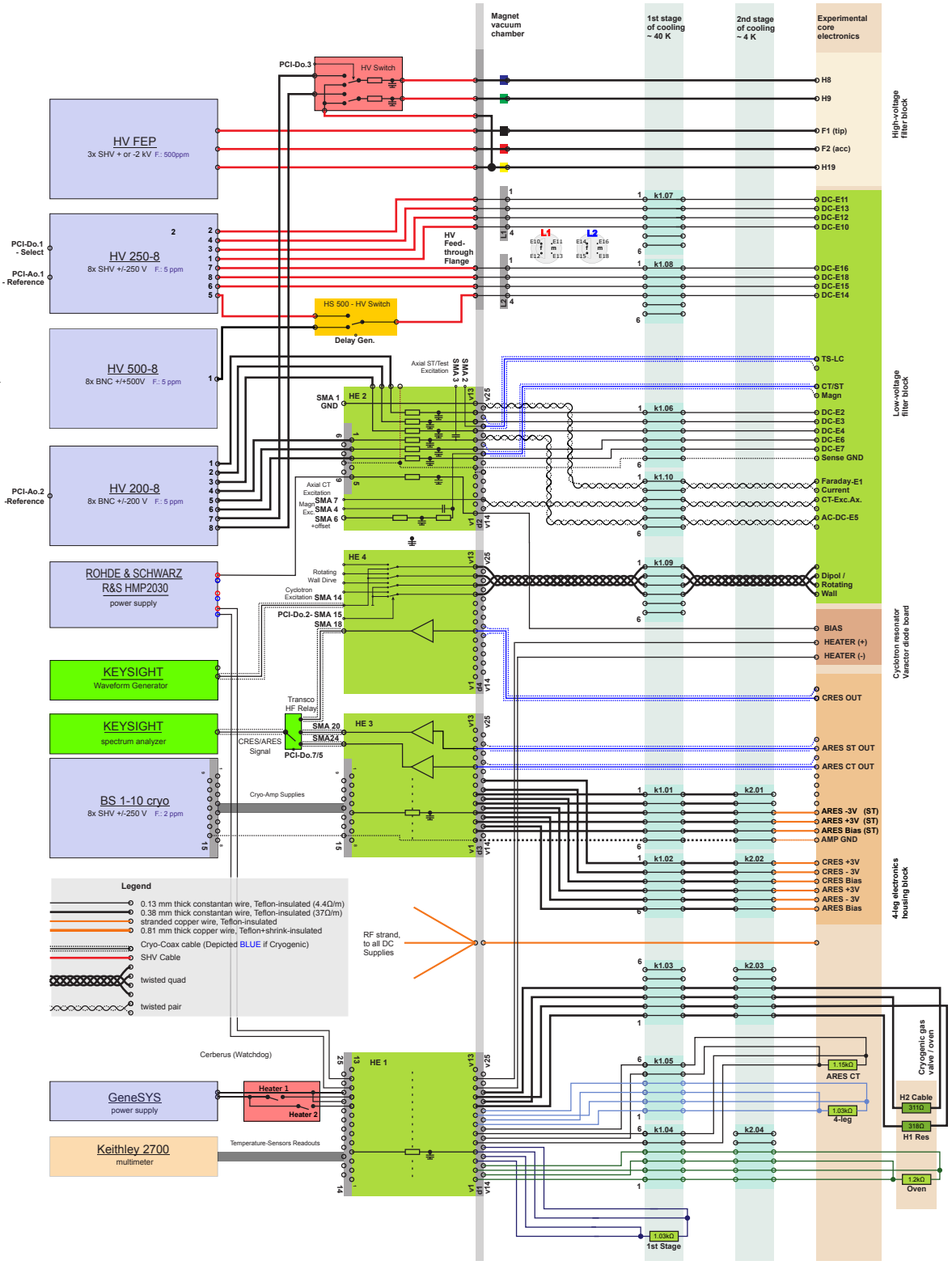

Figure A.1: The 2017 updated version wiring diagram of ARTEMIS.

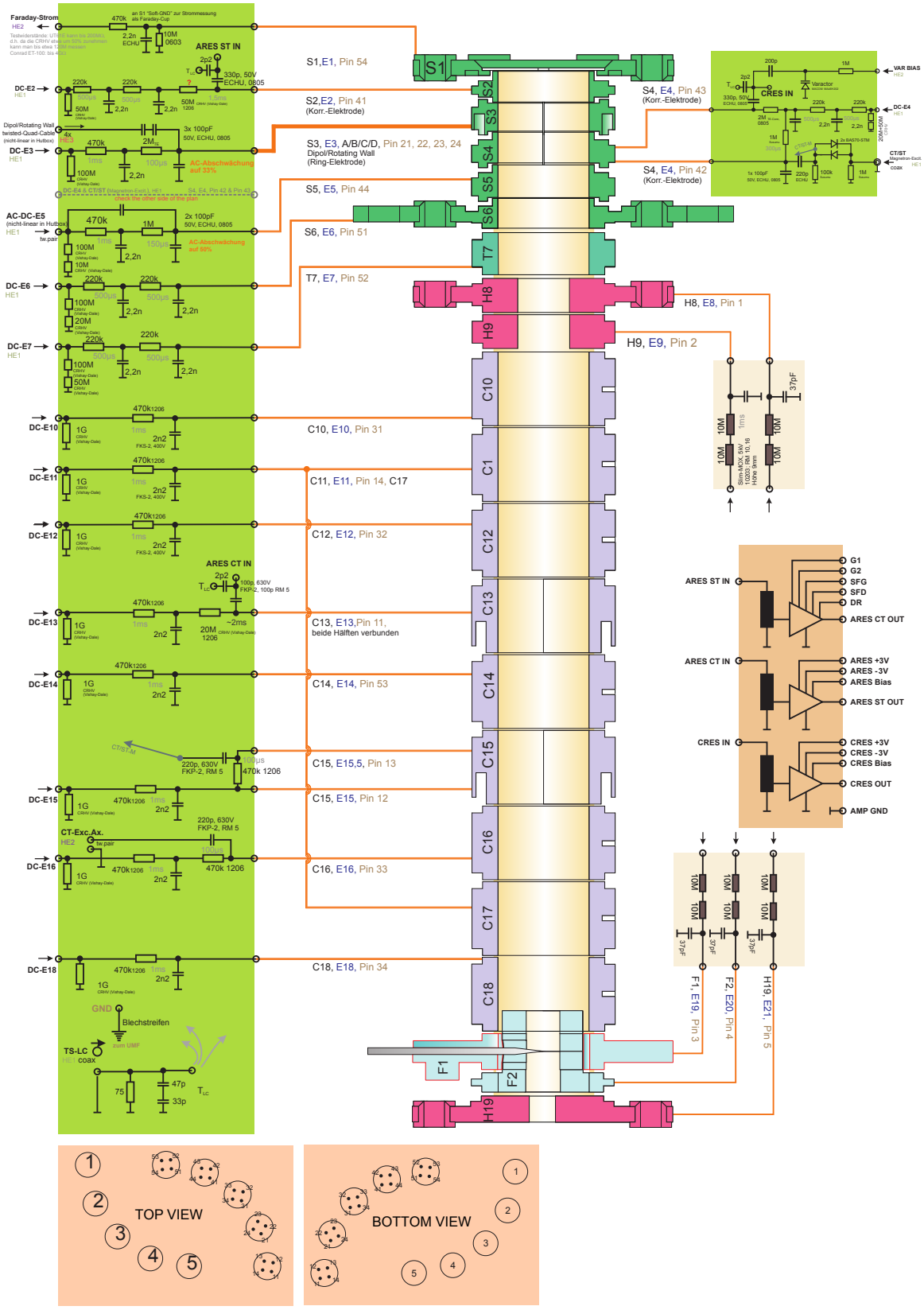

Figure A.2: The 2017 updated version wiring diagram of ARTEMIS.

APPENDIX

B

LASER DOPPLER COOLING

This cooling technique has proven to be one of the most effective ones and it is the common approach to reduce the axial energy of the ion from several thousand kelvin to approximately few mK in a Penning trap. Thus many theoretical and experimental efforts have been dedicated to it [122, and references therein]. The basic concept applied in such cooling is momentum exchange between the laser beam and the ions. As depicted in figure B.1, a laser beam parallel to the trap axis is irradiated and the particles absorb photons from the laser beam. Each absorbed photon transfers momentum to the particles and in doing so excites the ions into an excited atomic energy level. As a result, a spontaneous decay happens with the photons emitted evenly throughout the space. If the cooling-laser is slightly red-detuned from the frequency of transition in use, the particle slows down as a result of the light scattering force.

Less than a hand full of ions have the proper atomic energy level structure for laser-cooling procedure, such as beryllium, magnesium and calcium ions [18], only ions that exhibit a strong optical transition from ground state to the excited state with consecutive decay of the ion back to the ground state are suitable for laser-cooling of the ions. Furthermore, ions with many possible states to decay after the excitation make the laser-cooling complicated. Because to bring back an ion into the cooling cycle from one of undesired states requires an additional laser setup [50].

For Doppler laser cooling the so-called Doppler limit is the lowest achievable temperature $T_D = \hbar\gamma/k_B$, with γ expressing the decay rate of the excited state to its ground state. For the named ions typically used for laser cooling this limit is approximately $1\,\mathrm{mK}$. Although radial laser cooling is also possible by shining a perpendicular laser beam to the axis of the trap, due to the complications caused by the magnetron motion it is not as straight forward as in the case of the axial motion (in analogy to section 5.2.3). Reaching lower temperatures than the T_D, down to the motional ground state, is also possible by applying schemes of laser

cooling with resolved sidebands [123]. Initial study to implement this cooling technique in future at ARTEMIS have recently started.

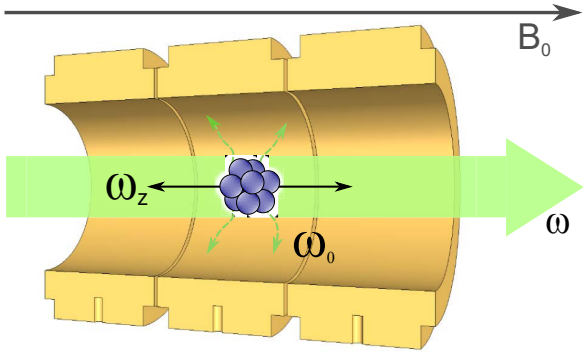

Figure B.1: Schematic overview of a laser cooling with cooling transition of ω_0. For successful cooling a red-detuned laser with frequency ω is applied to the ion ensemble parallel to the axial motion of the trapped particles.

LIST OF FIGURES

LIST OF TABLES

BIBLIOGRAPHY

[1] D. Hanneke, S. Fogwell, and G. Gabrielse. New Measurement of the Electron Magnetic Moment and the Fine Structure Constant. *Phys. Rev. Lett.*, 100(12):120801, 2008. doi:10.1103/physrevlett.100.120801.

[2] H. Häffner, T. Beier, N. Hermanspahn, H.-J. Kluge, W. Quint, S. Stahl, J. Verdú, and G. Werth. High-Accuracy Measurement of the Magnetic Moment Anomaly of the Electron Bound in Hydrogenlike Carbon. *Phys. Rev. Lett.*, 85(25):5308–5311, 2000. doi:10.1103/physrevlett.85.5308.

[3] J. Verdú, S. Djekić, S. Stahl, T. Valenzuela, M. Vogel, G. Werth, T. Beier, H.-J. Kluge, and W. Quint. Electronic g Factor of Hydrogenlike Oxygen $^{16}O^{7+}$. *Phys. Rev. Lett.*, 92(9), 2004. doi:10.1103/physrevlett.92.093002.

[4] J. Ullmann, Z. Andelkovic, C. Brandau, et al. High precision hyperfine measurements in Bismuth challenge bound-state strong-field QED. *Nat. Commun.*, 8(15484), 2017. doi:10.1038/ncomms15484.

[5] S. Borneis, A. Dax, T. Engel, et al. Ground-state hyperfine structure of heavy hydrogen-like ions. *Hyperfine Interactions*, 127(1/4):305–310, 2000. doi:10.1023/a:1012676508596.

[6] J.R. Crespo López-Urrutia, P Beiersdorfer, K Widmann, and V Decaux. Visible spectrum of highly charged ions: The forbidden optical lines of Kr, Xe, and Ba ions in the Ar I to Kr I isoelectronic sequence. *Canadian Journal of Physics*, 80(12):1687–1700, 2002. doi:10.1139/p02-080.

[7] J.R. Pierce. *Theory and Design of Electron Beams*. D. Van Nostrand Co., Inc., 1954. ISBN 1124091300.

[8] H. Dehmelt. Spin Resonance of Free Electrons. 1958-61 Progress Report for NSF Grant NSF-G 5955.

[9] H. G. Dehmelt and F. L. Walls. "Bolometric" Technique for the rf Spectroscopy of Stored Ions. *Physical Review Letters*, 21(3):127–131, 1968. doi:10.1103/physrevlett.21.127.

[10] R. S. Van Dyck, P. B. Schwinberg, and H. G. Dehmelt. Electron magnetic moment from geonium spectra: Early experiments and background concepts. *Physical Review D*, 34(3):722–736, 1986. doi:10.1103/physrevd.34.722.

[11] W. Quint and M. Vogel, editors. *Fundamental Physics in Particle Traps*. Springer Berlin Heidelberg, 2014. ISBN 978-3-642-45200-0.

[12] F. Köhler, K. Blaum, M. Block, S. Chenmarev, S. Eliseev, D. A. Glazov, M. Goncharov, J. Hou, A. Kracke, D. A. Nesterenko, Y. N. Novikov, W. Quint, E. M. Ramirez, V. M. Shabaev, S. Sturm, A. V. Volotka, and Günter Werth. Isotope dependence of the Zeeman effect in lithium-like calcium. *Nat. Commun.*, 7(10246):10246, 2016. doi:10.1038/ncomms10246.

[13] A. Wagner, S. Sturm, F. Köhler, D. A. Glazov, A. V. Volotka, G. Plunien, W. Quint, G. Werth, V. M. Shabaev, and K. Blaum. g-Factor of Lithiumlike Silicon $^{28}Si^{13}$. *Phys. Rev. Lett.*, 110(3):033003, 2013. doi:10.1103/physrevlett.110.033003.

[14] W. Quint, D. L. Moskovkhin, V. M. Shabaev, and M. Vogel. Laser-microwave double-resonance technique for g-factor measurements in highly charged ions. *Phys. Rev. A*, 78(3):032517, 2008. doi:10.1103/physreva.78.032517.

[15] M. Vogel. *Particle Confinement in Penning Traps: An Introduction (Springer Series on Atomic, Optical, and Plasma Physics)*. Springer, 2018. ISBN 978-3-319-76263-0.

[16] D. von Lindenfels, M. Vogel, W. Quint, G. Birkl, and M. Wiesel. Half-open Penning trap with efficient light collection for precision laser spectroscopy of highly charged ions. *Hyp. Int.*, 227:197Ű207, 2014. doi:10.1007/s10751-013-0961-z.

[17] D. von Lindenfels, N.P.M. Brantjes, G. Birkl, W. Quint, V. M. Shabaev, and M. Vogel. Bound electron g-factor measurement by double-resonance sepctroscopy on a fine-structure transition. *Can. J. Phys.*, 89:79–84, 2011. doi:10.1139/P10-071.

[18] T. Murböck, S. Schmidt, G. Birkl, W. Nörtershäuser, R. C. Thompson, and M. Vogel. Rapid crystallization of externally produced ions in a Penning trap. *Phys. Rev. A*, 94 (4):043410, 2016. doi:10.1103/PhysRevA.94.043410.

[19] J. Steinmann. *Analytical and numerical investigations of resistive cooling of trapped ion clouds*. PhD thesis, Universität Erlangen-Nürnberg, 2016.

[20] D. von Lindenfels. *Experimental Studies of Highly Charged Ions in a Penning Trap for the Measurement of Electron Magnetic Moments by Double-Resonance Spectroscopy*. PhD thesis, University of Heidelberg, Germany, 2015.

[21] M. Wiesel. *Preparation and Investigation of Highly Charged Ions in a Penning Trap for the Determination of Atomic Magnetic Moments*. PhD thesis, Technische Universität Darmstadt, 2017.

[22] F. Heiße, F. Köhler-Langes, S. Rau, J. Hou, S. Junck, A. Kracke, A. Mooser, W. Quint, S. Ulmer, G. Werth, K. Blaum, and S. Sturm. High-Precision Measurement of the Proton's Atomic Mass. *Phys. Rev. Lett.*, 119(3):033001, 2017. doi:10.1103/physrevlett.119.033001.

[23] S. Ulmer, C. Smorra, A. Mooser, K. Franke, H. Nagahama, G. Schneider, T. Higuchi, S. Van Gorp, K. Blaum, Y. Matsuda, W. Quint, J. Walz, and Y. Yamazaki. High-precision comparison of the antiproton-to-proton charge-to-mass ratio. *Nature*, 524 (7564):196–199, 2015. doi:10.1038/nature14861.

[24] M. Ahmadi, B. X. R. Alves, C. J. Baker, et al. Observation of the hyperfine spectrum of antihydrogen. *Nature*, 548(7665):66–69, 2017. doi:10.1038/nature23446.

[25] R. S. Van Dyck, P. B. Schwinberg, and H. G. Dehmelt. New high-precision comparison of electron and positron g factors. *Phys. Rev. Lett.*, 59(1):26–29, 1987. doi:10.1103/physrevlett.59.26.

[26] C. Smorra, S. Sellner, M. J. Borchert, J. A. Harrington, T. Higuchi, H. Nagahama, T. Tanaka, A. Mooser, G. Schneider, M. Bohman, K. Blaum, Y. Matsuda, C. Ospelkaus, W. Quint, J. Walz, Y. Yamazaki, and S. Ulmer. A parts-per-billion measurement of the antiproton magnetic moment. *Nature*, 550(7676):371–374, 2017. doi:10.1038/nature24048.

[27] B. Odom, D. Hanneke, B. D'Urso, and G. Gabrielse. New Measurement of the Electron Magnetic Moment Using a One-Electron Quantum Cyclotron. *Phys. Rev. Lett.*, 97(3): 030801, 2006. doi:10.1103/PhysRevLett.97.030801.

[28] S. Sturm, A. Wagner, B. Schabinger, J. Zatorski, Z. Harman, W. Quint, G. Werth, C. H. Keitel, and K. Blaum. g-factor of Hydrogenlike $^{28}Si^{13}$. *Phys. Rev. Lett.*, 107(2): 023002, 2011. doi:10.1103/physrevlett.107.023002.

[29] C. P. Poole Jr. *Electron Spin Resonance: A Comprehensive Treatise on Experimental Techniques/Second Edition*. Dover Publications, 1997. ISBN 978-0486694443.

[30] C. Clauss, D. Bothner, D. Koelle, R. Kleiner, L. Bogani, M. Scheffler, and M. Dressel. Broadband electron spin resonance from 500 MHz to 40 GHz using superconducting coplanar waveguides. *Appl. Phys. Lett.*, 102(16):162601, 2013. doi:10.1063/1.4802956.

[31] P. A. M. Dirac. The Quantum Theory of the Emission and Absorption of Radiation. *Proceedings of the Royal Society A: Mathematical, Physical and Engineering Sciences*, 114(767):243–265, 1927. doi:10.1098/rspa.1927.0039.

[32] P. Kusch and H.M. Foley. Precision measurement of the ratio of the atomic g values in the $^2P_{3/2}$ and $^2P_{1/2}$ states of gallium. *Phys. Rev.*, 72(1256):1256–1257, 1947.

[33] H. M. Foley and P. Kusch. On the Intrinsic Moment of the Electron. *Phys. Rev.*, 73 (4):412–412, 1948. doi:10.1103/physrev.73.412.

[34] R. P. Feynman. Space-Time Approach to Quantum Electrodynamics. *Phys. Rev.*, 76 (6):769–789, 1949. doi:10.1103/physrev.76.769.

[35] F. J. Dyson. Divergence of Perturbation Theory in Quantum Electrodynamics. *Phys. Rev.*, 85(4):631–632, 1952. doi:10.1103/physrev.85.631.

[36] A. A. Shchepetnov, D. A. Glazov, A. V. Volotka, V. M. Shabaev, I. I. Tupitsyn, and G. Plunien. Nuclear recoil correction to thegfactor of boron-like argon. *J. Phys. Conf. Ser.*, 583(1):012001, 2015. doi:10.1088/1742-6596/583/1/012001.

[37] D. A. Glazov, A. V. Malyshev, V. M. Shabaev, and I. I. Tupitsyn. Nuclear recoil effect on the g factor of middle-Z boronlike ions. *arXiv*, 2017. URL `http://arxiv.org/pdf/1711.09293v1`.

[38] D. Hanneke, S. Fogwell Hoogerheide, and G. Gabrielse. Cavity control of a single-electron quantum cyclotron: Measuring the electron magnetic moment. *Phys. Rev. A*, 83(5):052122, 2011. doi:10.1103/physreva.83.052122.

[39] S. Sturm, M. Vogel, F. Köhler-Langes, W. Quint, K. Blaum, and G. Werth. High-precision measurements of the bound electron's magnetic moment. *Atoms*, 5(4):4, 2017. doi:10.3390/atoms5010004.

[40] G. BREIT. The magnetic moment of the electron. *Nature*, 122(3078):649–649, 1928. doi:10.1038/122649a0.

[41] F. Beyer. *Introduction to the Physics of Highly Charged Ions*. Taylor & Francis Ltd, 2002. ISBN 9781420034097.

[42] L. S. Brown and G. Gabrielse. Geonium theory: Physics of a single electron or ion in a Penning trap. *Rev. Mod. Phys.*, 58:233–311, 1986. doi:10.1103/revmodphys.58.233.

[43] H. Häffner, T. Beier, S. Djekić, N. Hermanspahn, H.-J. Kluge, W. Quint, S. Stahl, J. Verdú, T. Valenzuela, and G. Werth. Double Penning trap technique for precise g-factor determinations in highly charged ions. *Eur. Phys. J. D*, 22(2):163–182, 2003. doi:10.1140/epjd/e2003-00012-2.

[44] S. Sturm, F. Köhler, J. Zatorski, A. Wagner, Z. Harman, G. Werth, W. Quint, C. H. Keitel, and K. Blaum. High-precision measurement of the atomic mass of the electron. *Nature*, 506(7489):467–470, 2014. doi:10.1038/nature13026.

[45] T. Nakamura, M. Wada, K. Okada, I. Katayama, S. Ohtani, and H.A. Schuessler. Precision spectroscopy of the Zeeman splittings of the hyperfine structure for nuclear structure studies. *Opt. Commun.*, 205(4-6):329–336, 2002. doi:10.1016/s0030-4018(02)01259-2.

[46] V. Mäckel, R. Klawitter, G. Brenner, J. R. Crespo López-Urrutia, and J. Ullrich. Laser spectroscopy of highly charged argon at the Heidelberg electron beam ion trap. *Phys. Scr.*, T156(T156):014004, 2013. doi:10.1088/0031-8949/2013/t156/014004.

[47] A. Lapierre, U. D. Jentschura, J. R. Crespo López-Urrutia, J. Braun, G. Brenner, H. Bruhns, D. Fischer, A. J. González Martínez, Z. Harman, W. R. Johnson, C. H. Keitel, V. Mironov, C. J. Osborne, G. Sikler, R. Soria Orts, V. Shabaev, H. Tawara, I. I. Tupitsyn, J. Ullrich, and A. Volotka. Relativistic Electron Correlation, Quantum Electrodynamics, and the Lifetime of the$1s^2\ 2s^2\ 2p^2P_{3/2}$ Level in Boronlike Argon. *Phys. Rev. Lett.*, 95(18):183001, 2005. doi:10.1103/physrevlett.95.183001.

[48] D. von Lindenfels, M. Wiesel, D. A. Glazov, A. V. Volotka, M. M. Sokolov, V. M. Shabaev, G. Plunien, W. Quint, G. Birkl, A. Martin, and M. Vogel. Experimental access to higher-order Zeeman effects by precision spectroscopy of highly charged ions in a Penning trap. *Phys. Rev. A*, 87(2):023412, 2013. doi:10.1103/physreva.87.023412.

[49] H. Dehmelt. Experiments with an isolated subatomic particle at rest. *Rev. Mod. Phys.*, 62:525–530, 1990. doi:10.1103/RevModPhys.62.525.

[50] M. Knoop, N. Madsen, and R.C. Thompson. *Physics with Trapped Charged Particles: A Graduate Textbook with Problems and Solutions (Advanced Textbooks in Physics)*. World Scientific (UK), 2016. ISBN 978-1-78634-011-5.

[51] F. Herfurth, Z. Andelkovic, W. Barth, et al. The HITRAP facility for slow highly charged ions. *Phys. Scr.*, 2015(T166):014065, 2015. doi:10.1088/0031-8949/2015/T166/014065.

[52] V. N. Gheorghe, F.G. Major, and G. Werth. *Charged Particle Traps*. Springer-Verlag, Heidelberg, 2004. ISBN 3540220437.

[53] G. Gabrielse, L. Haarsma, and S.L. Rolston. Open-endcap Penning traps for high precision experiments. *Int. J. Mass Spectrom. Ion Processes*, 88(2):319 – 332, 1989. doi:http://dx.doi.org/10.1016/0168-1176(89)85027-X.

[54] THORLABS. *Conductive ITO Coated Windows*. THORLABS. URL `https://www.thorlabs.com/newgrouppage9.cfm?objectgroup_id=5750`.

[55] S. Bharadia, M. Vogel, D. M. Segal, and R. C. Thompson. Dynamics of laser-cooled Ca+ ions in a Penning trap with a rotating wall. *Appl. Phys. B*, 107(4):1105Ű1115, 2012. doi:10.1007/s00340-012-4871-6.

[56] M. Wiesel, G. Birkl, M. S. Ebrahimi, A. Martin, W. Quint, N. Stallkamp, and M. Vogel. Optically transparent solid electrodes for precision Penning traps. *Rev. Sci. Instrum.*, 88(12):123101, 2017. doi:10.1063/1.5002180.

[57] H. Nagahama, C. Smorra, S. Sellner, J. Harrington, T. Higuchi, M. J. Borchert, T. Tanaka, M. Besirli, A. Mooser, G. Schneider, K. Blaum, Y. Matsuda, C. Ospelkaus, W. Quint, J. Walz, Y. Yamazaki, and S. Ulmer. Sixfold improved single particle measurement of the magnetic moment of the antiproton. *Nat. Commun.*, 8(14084 (2017)), 2017. doi:10.1038/ncomms14084.

[58] G. Gabrielse and F.C. Mackintosh. Cylindrical Penning traps with orthogonalized anharmonicity compensation. *Int. J. Mass Spectrom. Ion Processes*, 57(1):1–17, 1984. doi:https://doi.org/10.1016/0168-1176(84)85061-2.

[59] M. Vogel, W. Quint, and W. Nörtershäuser. Trapped Ion Oscillation Frequencies as Sensors for Spectroscopy. *Sensors*, 10(3):2169–2187, 2010. doi:10.3390/s100302169.

[60] Martin Kretzschmar. Theory of the elliptical Penning trap. *Int. J. Mass Spectrom.*, 275 (1-3):21–33, 2008. doi:10.1016/j.ijms.2008.05.009.

[61] L. S. Brown and G. Gabrielse. Precision spectroscopy of a charged particle in an imperfect Penning trap. *Phys. Rev. A*, 25:2423–2425, 1982. doi:10.1103/PhysRevA.25.2423.

[62] J. Yu, M. Desaintfuscien, and F. Plumelle. Ion density limitation in a Penning trap due to the combined effect of asymmetry and space charge. *Appl. Phys. B*, 48(1):51–54, 1989. doi:10.1007/BF00694417.

[63] P. M. Bellan. *Fundamentals of Plasma Physics*. Cambridge University Press, UK, 2008. ISBN 0521528003.

[64] A. Martin. *Laser Spectroscopy Investigations of Exotic States in Noble Gases*. PhD thesis, Technische Universität Darmstadt, 2017.

[65] D. J. Wineland and H. G. Dehmelt. Principles of the stored ion calorimeter. *J. Appl. Phys.*, 46(2):919, 1975. doi:http://dx.doi.org/10.1063/1.321602.

[66] S. Ulmer. *First Observation of Spin Flips with a Single Proton Stored in a Cryogenic Penning Trap*. PhD thesis, University of Heidelberg, 2011.

[67] S. Stahl. *Aufbau eines Experiments zur Bestimmung elektronischer g-Faktoren einzelner wasserstoffähnlicher Ionen*. PhD thesis, Universität Mainz, 1998.

[68] J. Carr. *Secrets of RF Circuit Design*. McGraw-Hill/TAB Electronics, 2000. ISBN 978-0071370677.

[69] D. M. Pozar. *Microwave Engineering*. John Wiley & Sons inc, 2011. ISBN 0470631554.

[70] American radio relay league. *American radio relay league handbook for radio amateurs 1994*. American radio relay league in, 1993. ISBN 0-87259-171-9.

[71] F.E. Terman. *Electronic and Radio Engineering (Electrical & Electronic Engineering)*. McGraw-Hill Inc.,US, 1955. ISBN 0070635099.

[72] D. H. Staelin. *Electromagnetics and Applications*. Department of Electrical Engineering and Computer Science, Massachusetts Institute of Technology , Cambridge, MA, 2011.

[73] S. W. Pasko, M. K. Kazimierczuk, and B. Grzesik. Self-Capacitance of Coupled Toroidal Inductors for EMI Filters. *IEEE Trans. Electromagn. Compat.*, 57(2):216–223, 2015. doi:10.1109/TEMC.2014.2378535.

[74] RUAG. *RUAG Thermal Insulation Products*. https://www.ruag.com, 2017.

[75] H. Nagahama, G. Schneider, A. Mooser, C. Smorra, S. Sellner, J. Harrington, T. Higuchi, M. Borchert, T. Tanaka, M. Besirli, K. Blaum, Y. Matsuda, C. Ospelkaus,

W. Quint, J. Walz, Y. Yamazaki, and S. Ulmer. Highly sensitive superconducting circuits at ∼700 kHz with tunable quality factors for image-current detection of single trapped antiprotons. *Rev. Sci. Instrum.*, 87(11):113305, 2016. doi:10.1063/1.4967493.

[76] M. S. Ebrahimi, N. Stallkamp, W. Quint, M. Wiesel, M. Vogel, A. Martin, and G. Birkl. Superconducting radio-frequency resonator in magnetic fields up to 6 T. *Rev. Sci. Instrum.*, 87(7):075110, 2016. doi:10.1063/1.4958647.

[77] J. Cheng, J. Liu, Z. Ni, C. Cui, S. Chen, S. Song, L. Li, Y. Dai, and Q. Wang. Fabrication of NbTi Superconducting Joints for 400-MHz NMR Application. *IEEE Trans. Appl. Supercond.*, 22(2):4300205–4300205, 2012. doi:10.1109/TASC.2012.2185795.

[78] K. Seo, S. Nishijima, K. Katagiri, and T. Okada. Evaluation of solders for superconducting magnetic shield. *IEEE Trans. Magn.*, 27(2):1877–1880, 1991. doi:10.1109/20.133563.

[79] R.F. Thornton. Superconducting joint for superconducting wires and coils and method of forming, May 17 1988. US Patent 4,744,506.

[80] M. Hüllen. Entwicklung und Test eines elektronischen Nachweissystems für hoch geladene Ionen in einer Penning-Falle. Bachlor Thesis, Hochschule Karlsruhe, 2011. (Engl. translation: Development and test of an electronic detection system for highly charged ions in a Penning trap).

[81] M. Tinkham. *Introduction to Superconductivity*. Dover Publications, 2004. ISBN 0486435032.

[82] A. V. Narlikar. *Superconductors*. Oxford University Press, 2014. ISBN 0199584117.

[83] A. Godeke, D. Cheng, D.R. Dietderich, P. Ferracin, S.O. Prestemon, G. Sabbi, and R.M. Scanlan. Limits of NbTi and Nb3Sn and Development of W&R Bi-2212 High Field Accelerator Magnets. *IEEE Trans. Appl. Supercond.*, 17(2):1149–1152, 2007. doi:10.1109/tasc.2007.898447.

[84] M. N. Kunchur and S. J. Poon. Critical fields and critical currents of superconducting disks in transverse magnetic fields. *Phys. Rev. B*, 43(4):2916–2921, 1991. doi:10.1103/physrevb.43.2916.

[85] J. Bardeen and M. J. Stephen. Theory of the Motion of Vortices in Superconductors. *Phys. Rev.*, 140(4A):A1197–A1207, 1965. doi:10.1103/physrev.140.a1197.

[86] Chia-Ren Hu and R. S. Thompson. Dynamic Structure of Vortices in Superconductors. type II . H much less than H/sub c2/. *Phys. Rev. B*, 6(1):110–120, 1972. doi:10.1103/physrevb.6.110.

[87] C. Song, T. W. Heitmann, M. P. DeFeo, K. Yu, R. McDermott, M. Neeley, John M. Martinis, and B. L. T. Plourde. Microwave response of vortices in superconducting thin films of Re and Al. *Phys. Rev. B*, 79(17):174512, 2009. doi:10.1103/physrevb.79.174512.

[88] S. Ulmer, H. Kracke, K. Blaum, S. Kreim, A. Mooser, W. Quint, C. C. Rodegheri, and J. Walz. The quality factor of a superconducting rf resonator in a magnetic field. *Rev. Sci. Instrum.*, 80(12):123302, 2009. doi:10.1063/1.3271537.

[89] M. Vogel, W. Quint, G.G. Paulus, and Th. Stöhlker. A Penning trap for advanced studies with particles in extreme laser fields. *Nucl. Instrum. Methods Phys. Res., Sect. B*, 285:65–71, 2012. doi:10.1016/j.nimb.2012.05.001.

[90] D. Bothner, T. Gaber, M. Kemmler, D. Koelle, R. Kleiner, S. Wünsch, and M. Siegel. Magnetic hysteresis effects in superconducting coplanar microwave resonators. *Phys. Rev. B*, 86(1):014, 2012. doi:10.1103/physrevb.86.014517.

[91] C. P. Bean. Magnetization of Hard Superconductors. *Phys. Rev. Lett.*, 8(6):250–253, 1962. doi:10.1103/physrevlett.8.250.

[92] M. S. Ebrahimi. Planar Superconducting Microwave Resonators. Master's thesis, University of Stuttgart, 2013.

[93] E. H. Brandt and M. Indenbom. Type-II-superconductor strip with current in a perpendicular magnetic field. *Phys. Rev. B*, 48(17):12893–12906, 1993. doi:10.1103/physrevb.48.12893.

[94] C. P. Poole, H. A. Farach, R. J. Creswick, and R. Prozorov. *Superconductivity*. Academic Press, 2010. ISBN 978-0120887613.

[95] J. C. Holt. *The Art of Electronics*. Cambridge University Press, UK, 2015. ISBN 0521809266.

[96] Y. Tawk, J. Constantine, and C. Christodoulou. *Antenna Design for Cognitive Radio*. Artech House Publishers, 2016. ISBN 1608079538.

[97] L. DiCarlo, Y. Zhang, D. T. McClure, C. M. Marcus, L. N. Pfeiffer, and K. W. West. System for measuring auto- and cross correlation of current noise at low temperatures. *Rev. Sci. Instrum.*, 77(7):073906, 2006. doi:10.1063/1.2221541.

[98] S. M. Sze and K. K. Ng. *Physics of Semiconductor Devices*. John Wiley & Sons inc, 2006. ISBN 0471143235.

[99] H Nagahama. Development of Low Noise Electronics for the Measurement of the Magnetic Moment of the Antiproton. Master's thesis, The University of Tokyo, 2014.

[100] A. Martin and P. Bausand G. Birkl. External cavity diode laser setup with two interference filters. *Appl. Phys. B*, 122(12):298, 2016. doi:10.1007/s00340-016-6575-9.

[101] P. Baus. Characterization of a Wide Tunable, Robust, Multi Application Diode Laser for Spectroscopy. Master's thesis, TU Darmstadt, 2014.

[102] J. Cariou and P. Luc. Atlas du Spectre d'Absorption de la Molécule de Tellure, 21100 cm^{-1}- $23800cm^{-1}$. *No. Bd. 5 in Atlas du Spectre dŠAbsorption de la Molécule de Tellure (Laboratoire Aime-Cotton)*, 1980.

[103] S. Albrecht, S. Altenburg, C. Siegel, N. Herschbach, and G. Birkl. A laser system for the spectroscopy of highly charged bismuth ions. *Appl. Phys. B*, 107(4):1069–1074, 2012. doi:10.1007/s00340-011-4732-8.

[104] T. Gassner. *High precision x-ray spectroscopy of highly charged heavy ions*. PhD thesis, Friedrich-Schiller-University Jena, 2016.

[105] C. Vogel. Aufbau und Charakterisierung eines Kaltventils fuer Penning-Fallen Experimente. Bachelor thesis, Technische Universität Darmstadt, 2014.

[106] Pfeiffer vacuum. *EVN 116 Dosing Valve, Operating Instructions*. https://www.pfeiffer-vacuum.com.

[107] W. M. Itano, J.C. Bergquist, J.J. Bollinger, and D.J. Wineland. Cooling methods in ion traps. *Phys. Scr.*, 1995(T59):106, 1995.

[108] M. Vogel, H. Häffner, K. Hermanspahn, S. Stahl, J. Steinmann, and W. Quint. Resistive and sympathetic cooling of highly-charged-ion clouds in a Penning trap. *Phys. Rev. A*, 90(4):043412, 2014. doi:10.1103/PhysRevA.90.043412.

[109] S. Djekic, J. Alonso, H.-J. Kluge, W Quint, S. Stahl, T. Valenzuela, J. Verdù, M. Vogel, and G. Werth. Temperature measurement of a single ion in a Penning trap. *The European Physical Journal D - Atomic, Molecular, Optical and Plasma Physics*, 31 (3):451–457, 2004. doi:10.1140/epjd/e2004-00168-1.

[110] C. C. Moore. Ergodic theorem, ergodic theory, and statistical mechanics. *Proceedings of the National Academy of Sciences*, 112(7):1907–1911, 2015. doi:10.1073/pnas.1421798112.

[111] M. Jensen, T. Hasegawa, and J. Bollinger. Temperature and heating rate of ion crystals in Penning traps. *Phys. Rev. A*, 70(3):033401, 2004. doi:10.1103/physreva.70.033401.

[112] H.U. Hasse, St. Becker, G. Dietrich, N. Klisch, H.J. Kluge, M. Lindinger, K. Lützenkirchen, L. Schweikhard, and J. Ziegler. External-ion accumulation in a Penning trap with quadrupole excitation assisted buffer gas cooling. *Int. J. Mass Spectrom. Ion Processes*, 132(3):181–191, 1994. doi:10.1016/0168-1176(93)03924-b.

[113] H.W. Ellis, M.G. Thackston, E.W. McDaniel, and E.A. Mason. Transport properties of gaseous ions over a wide energy range. Part III. *At. Data Nucl. Data Tables*, 31(1): 113–151, 1984. doi:10.1016/0092-640x(84)90018-4.

[114] I. Bergström, C. Carlberg, T. Fritioff, G. Douysset, J. Schönfelder, and R. Schuch. SMILETRAP—A Penning trap facility for precision mass measurements using highly charged ions. *Nucl. Instrum. Methods Phys. Res., Sect. A*, 487(3):618–651, 2002. doi:10.1016/s0168-9002(01)02178-7.

[115] G. Maero, F. Herfurth, H.-J. Kluge, S. Schwarz, and G. Zwicknagel. Numerical investigations on resistive cooling of trapped highly charged ions. *Appl. Phys. B*, 107(4): 1087–1096, 2011. doi:10.1007/s00340-011-4808-5.

[116] S. Van Gorp, M. Beck, M. Breitenfeldt, V. De Leebeeck, P. Friedag, A. Herlert, T. Iitaka, J. Mader, V. Kozlov, S. Roccia, G. Soti, M. Tandecki, E. Traykov, F. Wauters, Ch. Weinheimer, D. Zákoucký, and N. Severijns. Simbuca, using a graphics card to simulate Coulomb interactions in a penning trap. *Nucl. Instrum. Methods Phys. Res., Sect. A*, 638(1):192–200, 2011. doi:10.1016/j.nima.2010.11.032.

[117] P. K. Ghosh. *Ion Traps*. Oxford university press, 1996. ISBN 0198539959.

[118] K. Blaum. High-accuracy mass spectrometry with stored ions. *Phys. Rep.*, 425:1–78, 2006. doi:10.1016/j.physrep.2005.10.011.

[119] J.D. Huba. *NRL Plasma Formulary*. Beam Physics Branch, Plasma Physics Division, Naval Research Laboratory, Washington, DC 20375, (2013).

[120] M. Kiffer. Breitbandanregung von Ionen in einer Penningfalle. Bachlor Thesis, Friedrich-Schiller-University Jena, 2016.

[121] J. Alonso Otamendi. *Development of an Experiment for Ultrahigh-Precision g-Factor Measurements in a Penning-Trap Setup*. PhD thesis, Johannes Gutenberg-Universität Mainz, 2007.

[122] C. Champenois. Laser Cooling techniques applicable to trapped ions. In *Advanced Textbooks in Physics*, pages 117–145. World Scientific, apr 2016. ISBN 978-1-78634-011-5. doi:10.1142/9781786340139_0006.

[123] W. Demtröder. *Laser Spectroscopy*. Springer Berlin Heidelberg, 2008. ISBN 978-3-540-73418-5.

ACKNOWLEDGMENTS

> The only way to discover the limits of the possible
> is to go beyond them into the impossible.
>
> Arthur C. Clarke

First and foremost, I would like to thank *PD Dr. Wolfgang Quint* for giving me the opportunity to fulfill my lifelong dream and passion. Dear Wolfgang, you have taught me a great deal, not only as a scientist but also as a person. I will be forever grateful for all your kindness and support.

Often in challenging times one seeks a role model for a solution, I believe that in my PhD project that person was *Dr. Manuel Vogel*, knowledgeable and supportive. Dear Manuel, I sincerely appreciate your support during my PhD project and writing this thesis.

I would like to thank *Prof. Dr. Gerhard Birkl* for his constructive discussions and unlimited sharing of his experience and knowledge. Also, I would like to thank him for accepting the role as my second supervisor at HGS-HIRE Graduate School.

I appreciate all the efforts that *Prof. Dr. Thomas Stöhlker* makes on a daily basis to keep the atomic physics group at GSI beautifully running. I would like to thank *Prof. Dr. Klaus Blaum* for being the second advisor of this project at the University of Heidelberg.

I would like to use this opportunity to thank the referee of this thesis *Prof. Dr. Markus Oberthaler* and the members of the final examination committee *Prof. Dr. Peter Fischer* and *PD Dr. Antonino Di Piazza* .

Completing this work was supported by three organizations, GSI DARMSTADT, HGS-HIRE and HGSFP; which I would like to thank each and every one of the people working there for their

hard work. I would like to thank the colleagues at HITRAP collaboration for supporting the ARTEMIS experiment.

An important lesson of this PhD project was that no matter how difficult it seems to climb the mountain in front of you, a good team and supportive friends are all one needs. The hard work of *Dr. David von Lindenfels*, *Dr. Marco Wiesel* and *Dr. Alexander Martin* who created the ARTEMIS setup gave me the opportunity to work on such a complex and fascinating experiment. The future of ARTEMIS is guaranteed, since it will be left in the capable hands of *Mr. Zhexi Guo* and *Mr. Patrick Baus*. The collaboration with *Mr. Nils Stallkamp* showed me further the benefits of working with a capable and talented person. Thanks for all the hard work and the great time we had together. I would like to thank *Zhexi* and *Nils* again for reading and commenting on this thesis carefully and passionately.

I would like to express my gratitude to *Dr. Stefan Ulmer*, for giving me the opportunity to experience working in the most prestige physics facility in the world, CERN, and all the scientific discussions that we had. Also, I would like to thank *Dr. Hiroki Nagahama* and *Mr. Matthias Borchert* for making my stay at BASE even more pleasant.

I would like to thank *Dr. Stefan Stahl* and STAHL ELECTRONICS for all their great products and advices which is essential for ARTEMIS. Among other people that have contributed to the development of ARTEMIS, one name stands out and I would like to specially thank him, *Mr. Davide Racano*.

I would like to thank the following people for the great and friendly working atmosphere, their help and constructive discussions: *Dr. Rodolfo Sanchez*, *Dr. Zoran Andelkovic*, *Dr. Tobias Murböck*, *Dr. Stefan Schmidt*, *Dr. Tobias Gaßner*, *Mr. Stefan Ringleb*, *Ms. Anahita Khodaparast*, *Mr. Mouwafak Shaaban* and *Mr. Christian Vogel*.

And finally I would like to specially thank my wife *Cansel Bozkurt Ebrahimi* for standing by me in all the hardship and stressful times of my PhD period. Your devotion and love has been giving my life a different color and motivation to work hard and for that I will never be able to thank you enough. My dear parents *Mahdi* and *Nahid Ebrahimi* have always been my greatest inspiration to work hard and honestly. I would like to thank You from the bottom of my heart and I hope that I have succeeded in making you feel proud.

Mohammad Sadegh Ebrahimi
Darmstadt—19, February, 2018